



Review

## Advancements and future prospects of additive manufacturing in high-entropy alloy applications



S. Ragunath <sup>a</sup>, N. Radhika <sup>a,\*</sup>, Bassiouny Saleh <sup>b,c</sup>

<sup>a</sup> Department of Mechanical Engineering, Amrita School of Engineering, Amrita Vishwa Vidyapeetham, Coimbatore, India

<sup>b</sup> College of Energy and Power Engineering, Nanjing University of Aeronautics and Astronautics, Nanjing 210016, China

<sup>c</sup> Production Engineering Department, Alexandria University, Alexandria 21544, Egypt

ARTICLE INFO

Keywords:

High entropy alloys  
Additive manufacturing  
Microstructure  
Mechanical properties  
Challenges

ABSTRACT

A comprehensive review of Additive Manufacturing (AM) of High Entropy Alloys (HEAs) is presented, exploring the opportunities for producing advanced components with tailored properties through design-based alloys. HEAs have emerged as promising metallic materials with unique properties that cater to the needs of modern industries. The utilization of AM, a 3D printing technology, allows for the creation of intricately designed products with minimized defects by tailoring microstructural features. The combination of HEAs and AM offers exceptional mechanical properties, improved wear resistance, and enhanced corrosion behavior by optimizing process parameters. This article thoroughly reviews recent advancements in fabricating AM-built parts using HEAs, focusing on powder feedstock, microstructural aspects, phase formation, strengthening mechanisms, and resulting mechanical properties. Furthermore, it explores various applications of AM-processed HEAs in industries such as medical, hydrogen storage, aerospace, nuclear, coating, and automotive, providing detailed insights into their usage. The challenges encountered during the AM process are discussed, and future directions for enhancing the quality of customized products are outlined. This review article offers valuable insights into the realm of additive manufacturing AM of HEAs, incorporating recent developments. It catalyzes future research endeavors in this field.

### 1. Introduction

High Entropy Alloys (HEAs) are multi-component alloys developed in the 21st century to meet the demands of current industrial requirements due to their exceptional properties. Conventional metallic alloys typically consist of one primary element along with a few additional elements to enhance their properties. In contrast, HEAs are synthesized by incorporating five or more elements within an atomic range of 5–35%, using equimolar or non-equimolar ratios, thus achieving a maximum entropy of mixing [1,2]. HEAs have gained significant attention in materials research due to their exceptional mechanical properties, wear resistance, and corrosion behavior resulting from core effects and strengthening mechanisms [3]. The synthesized HEAs are categorized into lightweight HEAs, refractory HEAs, precious group of HEAs, lanthanide HEAs, 3D transitions HEAs, interstitial HEAs, and high entropy brasses and bronzes based on density, high-temperature materials, availability, and performance of contributed elements (Fig. 1) [4]. HEAs offer excellent high-temperature properties such as oxidation

resistance and creep behavior, enhanced structural integrity, and irradiation resistance. In some cases, HEAs exhibit more than two-phase structures, which are referred to as multi-component alloy systems [5]. A single-phase structure in HEA powders can be achieved by suppressing the precipitation of secondary structures through rapid cooling [6]. Hence, HEAs have the potential to be considered as alternative materials to Ni-based superalloys, particularly in engineering applications. The formation of intermetallic compounds and multiple phases in multicomponent alloys often results in complex microstructures and brittleness. High entropy mixing and a reduction in Gibbs free energy among the elements promote the formation of simple solid solution structures such as FCC, BCC, and HCP, and mixing these phases [4]. The fabrication of HEAs is categorized by solid-state, gas-state, and liquid-state synthesis. The synthesis processes play a significant role in producing refined grains, forming microstructures, and stabilizing phase structures [7,8]. Subsequently, a heat treatment process is undertaken to further improve material properties [9]. The different melting temperatures of principal elements and the rapid solidification route of

\* Corresponding author.

E-mail address: [n\\_radhika1@cb.amrita.edu](mailto:n_radhika1@cb.amrita.edu) (N. Radhika).

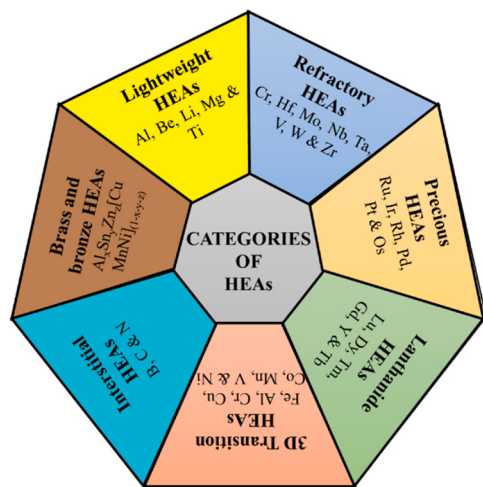


**Fig. 1.** Categories of high entropy alloys.

synthesis lead to segregation and inhomogeneous microstructure during the fabrication of HEAs [10]. A single-phase structure of HEA particles is achieved by rapidly cooling the material and suppressing the precipitation of secondary phases [11]. The unique microstructure obtains enhanced mechanical properties due to the metastable nature of HEA powders. The concept of metastability engineering employed in Transformation-Induced Plasticity (TRIP) during the synthesis of HEAs exhibits excellent performance in cryogenic conditions [12,13].

HEAs exhibit enhanced mechanical properties, including Ultimate Tensile Strength (UTS), yield strength, shear strength, and hardness [14]. However, the ductility of HEAs is often compromised due to the strength-ductility trade-off effect. Casting defects, such as large pores, cracks, and shrinkage, can also minimize the strengthening properties of synthesized HEA materials. To address these manufacturing challenges, an innovative and flexible fabrication technique known as Additive Manufacturing (AM) has emerged. AM techniques are widely utilized in the fabrication process to create intricate shapes and incorporate functionality that is difficult to achieve using conventional methods. By employing computer-aided design models, complex structural parts with improved strength and ductility can be fabricated layer by layer [15]. AM, as a transformative technology, has revolutionized various industries through its ability to generate objects based on 3D models using 3D printing techniques [16,17]. The AM products exhibit improved microstructures with homogeneously distributed grains, attributed to enhanced strengthening properties over the as-cast products. The near-net shape of complex geometric products built by AM minimizes the need for additional processes such as machining, finishing, and assembling. AM is employed in various engineering materials, including Al alloys, Ti alloys, stainless steel, and polyamide, for many applications in the engineering and medical sectors. AM leads to improved production efficiency with minimized waste, thanks to the synergistic effect of near-net shaping and design freedom [18,19]. The AM-processed HEAs exhibit improved chemical homogeneity by impeding diffusional phase transformation due to the higher cooling rate. AM offers effective material processing that improves mechanical properties, playing a vital role in specific applications under extreme conditions [20]. AM processes find applications in various industries due to their advantages, including rapid prototyping and customization capabilities. However, it is essential to acknowledge the limitations of AM. These limitations include restricted material choices and constraints on component size, which can render AM unsuitable for specific applications. Furthermore, achieving the same level of surface finish as traditional machining and injection molding processes can be challenging for AM, potentially affecting the quality and functionality of the end product. Moreover, the longer processing time associated with AM often leads to increased costs

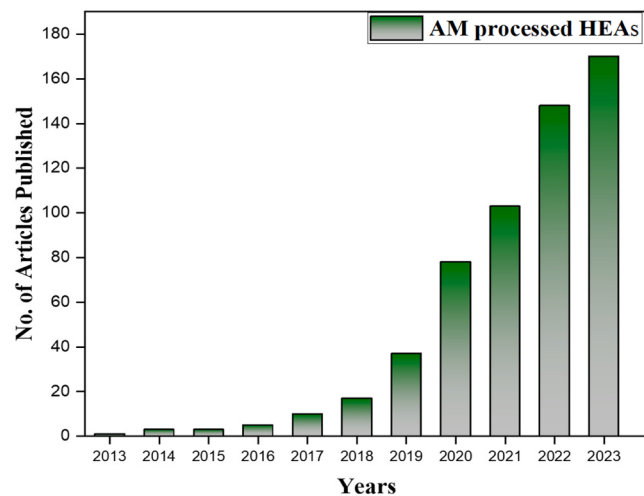


**Fig. 2.** Number of articles published on HEAs under the AM process (source: Scopus).

for the final product, making it less viable for mass production scenarios [21]. Fig. 2 illustrates the extensive body of research conducted thus far on AM-processed HEAs.

Based on available literature in terms of AM processing techniques in HEA, possible applications, and mechanical properties of AM-HEA, this study discusses the progress of these alloys. The need to conduct a review article on this topic arises from the growing interest in the AM of HEAs and its potential applications in various industries. By reviewing the advancements and prospects of AM in HEA applications, this article provides significant contributions to researchers and the industry. The review article offers a comprehensive overview of the current state of AM in HEA applications. It gathers and synthesizes information on various aspects, including powder feedstock, microstructural features, phase formation, strengthening mechanisms, and resulting mechanical properties. This comprehensive overview serves as a valuable resource for researchers seeking to understand the latest developments and trends in this field. Furthermore, the article provides detailed insights into the fabrication, stability, and intricate phase structures of AM-processed HEAs. Analyzing the interplay between microstructure, phases, precipitation, and strengthening mechanisms, enhances the understanding of the fundamental properties and behavior of these materials. This knowledge is crucial for researchers aiming to optimize the AM process and tailor the properties of HEAs for specific applications. The review also explores diverse applications of AM-processed HEAs in various industries, including medical, hydrogen storage, aerospace, nuclear, coating, and automotive sectors. By highlighting the specific advantages and potential applications of AM-processed HEAs in each industry, the article offers valuable insights to researchers and industry professionals. This information can guide decision-making processes and inspire new avenues of research and development. Additionally, the article discusses the challenges encountered during the AM process for HEAs. Identifying and addressing these challenges guide researchers and practitioners in overcoming technical barriers and improving the quality of customized products. This information is instrumental in advancing the practical implementation of AM-processed HEAs in real-world manufacturing scenarios. Thus, this study unveils the characterization of AM-processed HEAs, delving deep into their fabrication, stability, and intricate phase structures. Through detailed analysis, this review elucidates the interplay between microstructure, phases, precipitation, and strengthening mechanisms. It also highlights the enhanced properties exhibited by AM-processed HEAs, emphasizing recent advancements across diverse sectors such as medical, hydrogen storage, aerospace, nuclear, coating, and automotive industries. Additionally, the study systematically addresses the existing challenges and provides insights into the future prospects of

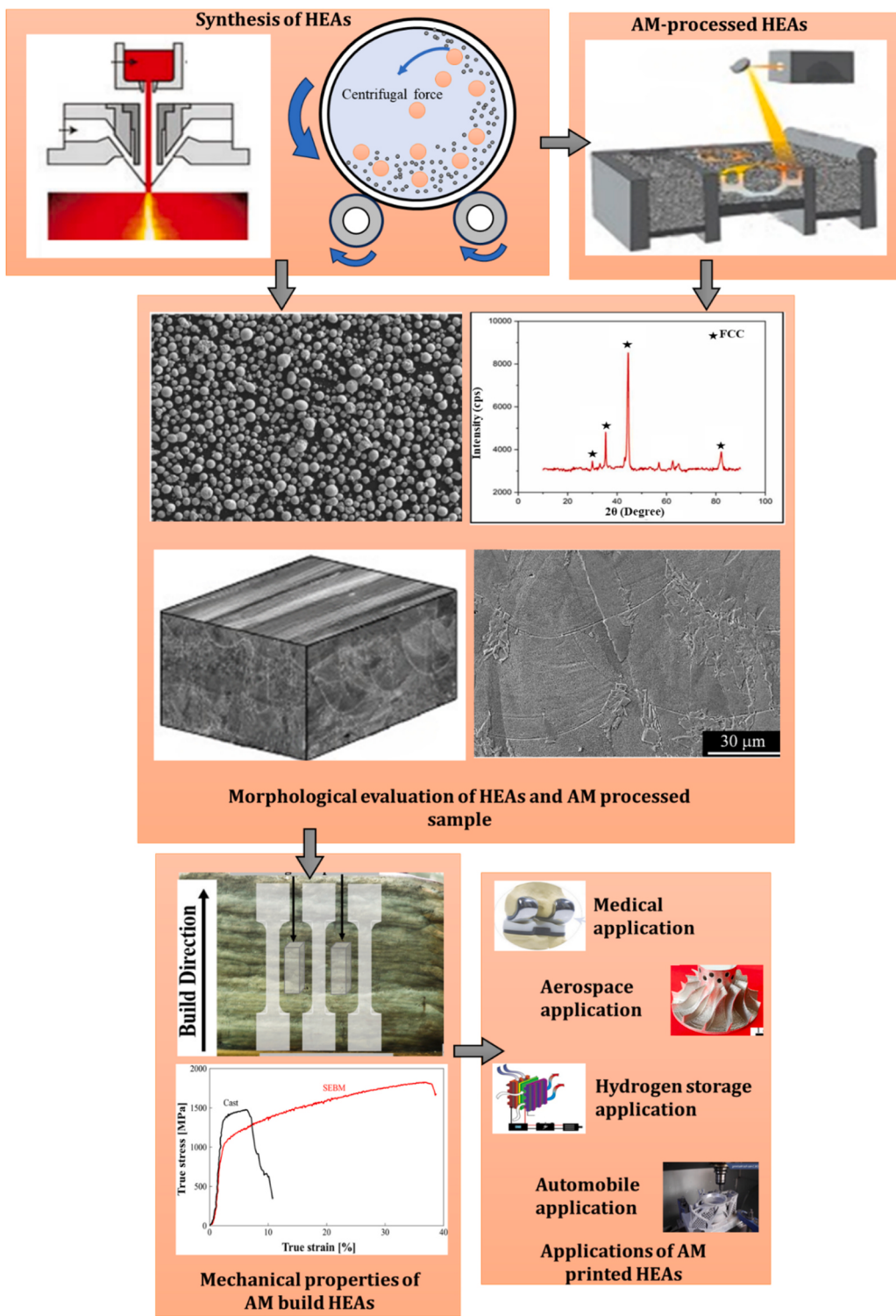


**Fig. 3.** Workflow chart of AM processed HEA - an overview. It is reproduced from [14,22–26] with permission of the publisher (Elsevier and Taylor & Francis).

AM processes in the context of HEAs. Fig. 3 illustrates the comprehensive methodology employed in this review of AM-processed HEAs.

## 2. High-entropy alloys

The strengthening properties of synthesized HEAs depend significantly on the choice of principal elements and their atomic percentages. The selection of the composition of constituent elements is a crucial process that involves investigating the thermodynamic core effects and

phase diagrams to ensure the formation of a single-phase solid solution.

### 2.1. Core effects of HEAs

HEAs distinguish themselves from other conventional alloys through their exceptional properties, including enhanced mechanical characteristics, superior stability at elevated temperatures, and exceptional resistance to wear and corrosion. These properties are achieved by tailoring the elemental composition and their ratio, which hinders

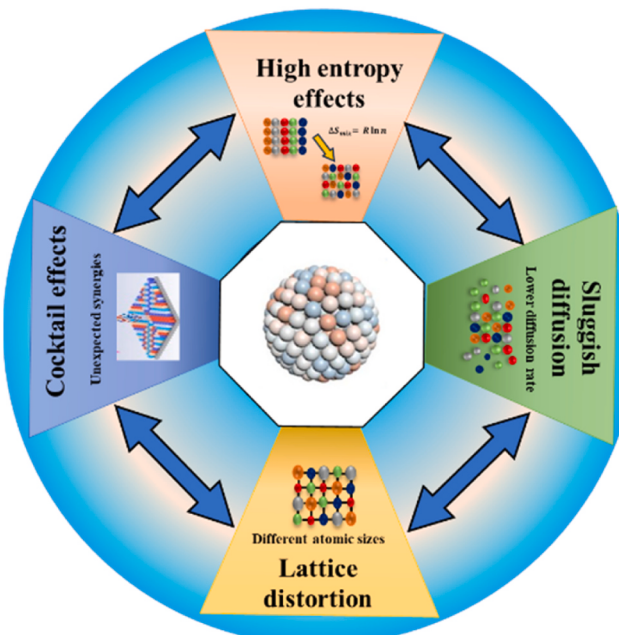


Fig. 4. Core effects of high entropy alloys.

dislocation movements, improves solid solution strengthening, and promotes the formation of oxide layers against corrosive environments [27]. The microstructure and mechanical properties of synthesized HEAs are governed by core effects, including high entropy effects, sluggish diffusion, cocktail effects, and severe lattice distortion (Fig. 4) [28]. The high entropy effect contributes to the formation of a solid solution and its associated thermodynamic features. The stability of the solid solution is achieved by minimizing Gibbs free energy, leading to an equilibrium state as per the thermodynamic second law [27,29]. The higher number of constituent elements results in lower free energy, which inhibits the formation of intermetallic phases [30]. The sluggish effect plays a role in controlling atomic diffusion, phase transformation, the formation of coarse particles, grain growth, fine precipitation,

recrystallization, and creep behavior. It influences the microstructural and morphological features, thereby enhancing the performance of HEAs [31]. However, investigations into the sluggish effect of HEAs have yielded conflicting results, leading to uncertainty and controversy [32,33]. The sluggish effect reduces diffusion and phase transformation rates during HEA fabrication, impacting phase transformation kinetics [34]. The diffusion rate is highly dependent on the elements and their composition, and the phenomenon of sluggish diffusion cannot be uniformly applied to all HEAs [33]. The improved structural properties of HEAs result from severe lattice distortion caused by the interaction of constituent elements. Each atom is surrounded by atoms of varying atomic sizes, leading to lattice stress and strain. The interfacial bonding, crystal structure, non-symmetrical binding, and varied electronic structures of the contributing elements result in severe lattice distortion throughout the lattice, varying from site to site [35,36]. The cocktail effect highlights the properties of at least quinary constituent elements. The phase structures of HEAs can be single or multiple, depending on the elemental composition and synthesis methods. The rule of mixture and the interaction of constituent elements through severe lattice distortion are significant factors for the enhanced properties of HEAs [28]. From the above discussion, the HEAs exhibit remarkable properties, including enhanced mechanical strength, stability at high temperatures, and resistance to wear and corrosion from tailored elemental compositions, hindering dislocation movements, enhancing solid solution strengthening, and core effects.

## 2.2. Strengthening mechanism of HEAs

The morphology and crystallographic structure of HEAs contribute to strengthening mechanisms by impeding and creating a barrier effect against dislocation motion. These strengthening mechanisms include solid solution strengthening, precipitation strengthening, phase transformation strengthening, and grain boundary strengthening (Fig. 5) [37]. The enhanced mechanical properties are achieved through the influences of solid solution strengthening [34]. The interaction of solute atoms with gliding dislocations effectively leads to solid solution strengthening, improving the yield strength of synthesized HEAs [38]. In substitutional solid solutions, solute atoms and solvent atoms are of the same size and occupy lattice sites. In interstitial solid solutions, solute

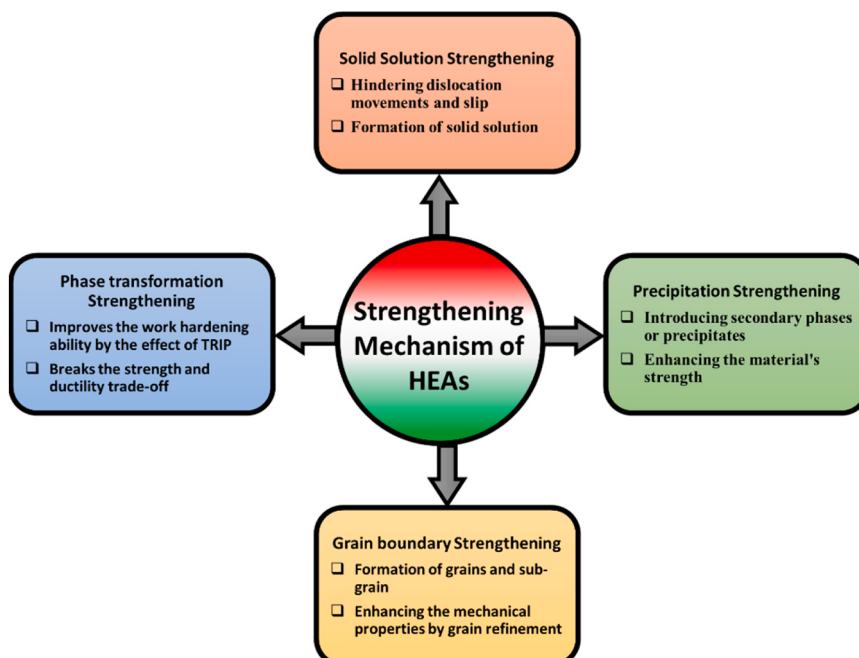
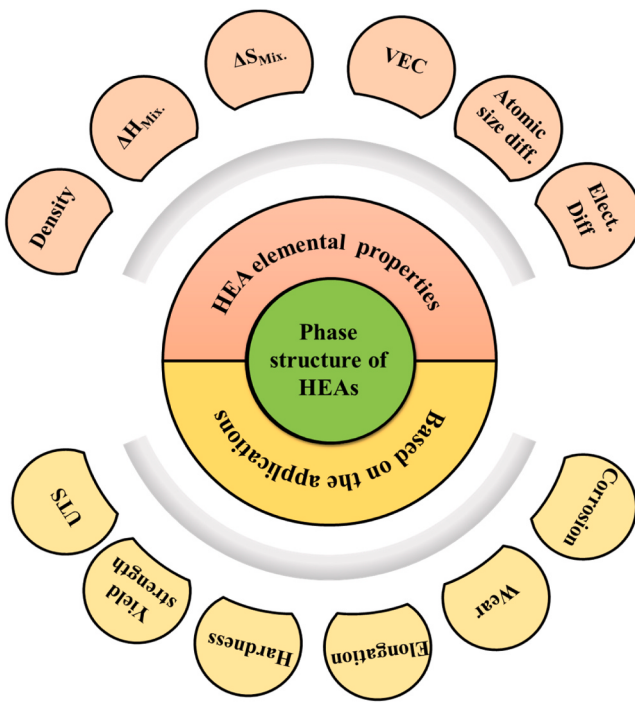


Fig. 5. Strengthening mechanism of high entropy alloys.



**Fig. 6.** Phase selection of HEAs according to their properties.

atoms are smaller than the solvent atoms and occupy interstitial sites. Precipitation strengthening is commonly employed to enhance the strength of HEAs through compositional modifications and heat treatment processes. By achieving a suitable composition and heat treatment, a high fraction of small-sized precipitates is obtained, resulting in excellent strengthening. The small precipitates create new interfaces, stacking fault energy, modulus mismatch, and coherency strains that interact with gliding dislocations. Conversely, the Orowan process is observed with large precipitates and gliding dislocations [39]. The coherent strengthening phase is achieved through the formation of an intermetallic phase obtained through precipitation strengthening [40]. Twinning and ductility are improved by the effect of twinning-induced plasticity in precipitation strengthening, thanks to the low stacking fault energy [41]. Coherent precipitates that exhibit exceptional mechanical properties receive significant attention from researchers. Grain boundary strengthening improves the strength of synthesized HEAs by impeding gliding dislocations. In grain boundaries, atoms move in their lattice sites to compensate for mismatches in adjacent grains, resulting in high energy at the grain interior [42]. Grain boundaries are a significant source of effective strengthening due to their ability to interact with dislocations. The introduction of nano-twins induced by grain boundary strengthening overcomes the trade-off between strength and ductility. Grain refinement restricts dislocation motion and crack propagation by overcoming the hindrance of coarse grains, thereby enhancing grain morphology [37]. Work hardening and ductility are improved by stress concentration resulting from self-refinement under reversible martensite transformation. The increase in the volume of the martensite phase ( $\epsilon$  HCP) enhances the yield strength of HEAs while preserving the TRIP effect [37].

Overall, the varying elemental composition of HEAs plays a crucial role in their behavior under applied stress, leading to the transformation from a single-phase structure to a metastable HEA. This transformation is influenced by the diverse composition of elements in HEAs, which can induce unique mechanical properties and behavior. One of the notable effects observed in HEAs is the TRIP effect, which enhances their work-hardening ability and disrupts the traditional trade-off between strength and ductility [43]. The TRIP effect is attributed to the simultaneous formation of twinning, slips, and stacking faults in the matrix phase of

HEAs. These microstructural features contribute to the delayed exhaustion of plasticity, allowing the material to sustain higher levels of deformation and maintain both strength and ductility [44]. In addition to the microstructural changes induced by the TRIP effect, the chemical composition of HEAs and their thermomechanical processing significantly impact their mechanical properties. Through heat treatment and straining, the chemical changes within the composition of HEAs can be optimized to enhance specific mechanical properties. This involves fine-tuning the grain size, managing the distribution of phases, and customizing the mechanical behavior of the material [37]. HEAs exhibit exceptional mechanical properties through a combination of strengthening mechanisms, including solid solution strengthening, precipitation strengthening, phase transformation strengthening, and grain boundary strengthening. These mechanisms impede dislocation motion and enhance the yield strength of the materials. The TRIP effect influences the traditional strength-ductility trade-off by inducing twinning, slips, and stacking faults, thereby delaying plasticity exhaustion and maintaining both strength and ductility. Overall, HEAs demonstrate promising potential for diverse applications due to their unique microstructural features and versatile mechanical response.

### 2.3. Evaluation of phase stability in HEAs

The evaluation of phases plays a vital role in influencing the properties and performance of materials, particularly in the context of single-solid solutions. The formation of the phase structure is governed by the elemental properties of HEAs and their intended applications (Fig. 6). The phase structure generated in synthesized HEAs has a significant impact on their mechanical, physical, thermal, chemical, and functional properties. Therefore, researchers can tailor the phase evaluation by carefully selecting constituent elements with specific atomic percentages and considering the thermodynamic properties involved.

The phase stability of HEAs is governed by the reduced Gibbs free energy, which is determined by the interplay between entropy and enthalpy mixing. This interplay is a dominant factor in the formation and stability of single-solid solutions within HEAs [37].

$$\Delta G_{mix} = \Delta H_{mix} - T\Delta S_{mix} \quad (1)$$

where  $\Delta G_{mix}$ ,  $\Delta S_{mix}$ , and  $\Delta H_{mix}$  are Gibbs free energy, entropy mixing, and enthalpy mixing, respectively. The reduced Gibbs free energy is obtained by increasing entropy mixing or decreasing enthalpy mixing for the stability of the solid phase. The entropy mixing is the summation of vibrational entropy, configurational entropy, magnetic dipole entropy, and electronic randomness entropy [45].

$$\Delta S_{mix} = \Delta S_{conf.} + \Delta S_{vib.} + \Delta S_{elec.} + \Delta S_{mag.} \quad (2)$$

Configurational entropy plays a vital role in the other entropy contributions; therefore, the mixing of entropy could be represented by configurational entropy to minimize complex calculations. The increase in the number of constituent elements in HEAs leads to a corresponding increase in configurational entropy [46]. In a reduced free energy state, the effect of configurational entropy is based on the irreversible process in the second law of thermodynamics [30]. The configurational entropy could be calculated using Boltzmann's analysis.

$$\Delta S_{conf.} = -R \sum X_i \ln X_i \quad (3)$$

where R is the universal gas constant and  $X_i$  is a mole fraction. The maximum configurational entropy, the value of  $X_i$  is 1/n. Hence,

$$(\Delta S_{conf.})_{max} = R \ln n \quad (4)$$

Where n is the number of constituent elements in HEAs. In addition to configurational entropy, the following factors, such as enthalpy of mixing and size factor, contribute to the stability of a single solid solution phase structure [47].



**Fig. 7.** Classification of the AM methods.

$$\Delta S_{\text{conf.}} > 1.5 \quad R \quad (5)$$

$$-15 \text{ kJ/mol.} < \Delta H_{\text{mix}} > 5 \text{ kJ/mol.} \quad (6)$$

$$\Delta H_{\text{mix}} = \sum_{i=1, j \neq i}^n \Omega_{ij} C_i C_j \quad (7)$$

$$\Omega_{ij} = 4 \Delta H_{AB}^{\text{mix}} \quad (8)$$

$$\Omega = \frac{T_m \Delta S_{\text{mix}}}{\Delta H_{\text{mix}}} \quad (9)$$

$$\delta > 6.6 \quad \% \quad (10)$$

Where  $\delta$  is a size factor,  $C_i, C_j$  are elements of the  $i^{\text{th}}$  and  $j^{\text{th}}$  atomic percentile.  $\Delta H_{AB}^{\text{mix}}$  is an enthalpy mixing of binary alloy AB. The positive and negative values represent that the HEAs tend to segregate and formation of intermetallic, respectively. Hence,  $\Omega$  plays an essential role in the solid solution formation ability of HEAs [48–50]. The Valence Electron Concentration (VEC) is also one of the factors that confirm the formation of the phase structure in HEAs through quantitative prediction.

$$\text{VEC} = \sum_{i=1}^n C_i \quad \text{VEC}_i \quad (11)$$

where  $C_i$  and  $\text{VEC}_i$  are the  $i^{\text{th}}$  elements atomic percentile and VEC. The stability of BCC, FCC, and the coexistence of BCC and FCC phase structures are identified by the value of  $\text{VEC} \leq 6.87$ ,  $\geq 8$ , and between 6.87 and 8, respectively [37]. The evaluation of phases in single-solid solution HEAs plays a significant role in determining their mechanical properties, wear resistance, and corrosion resistance. The phase structure, influenced by constituent elements and thermodynamic properties, can be tailored to enhance performance. The stability of the phase structure in HEAs is governed by the relationship between entropy and enthalpy mixing, specifically the configurational entropy. Boltzmann's

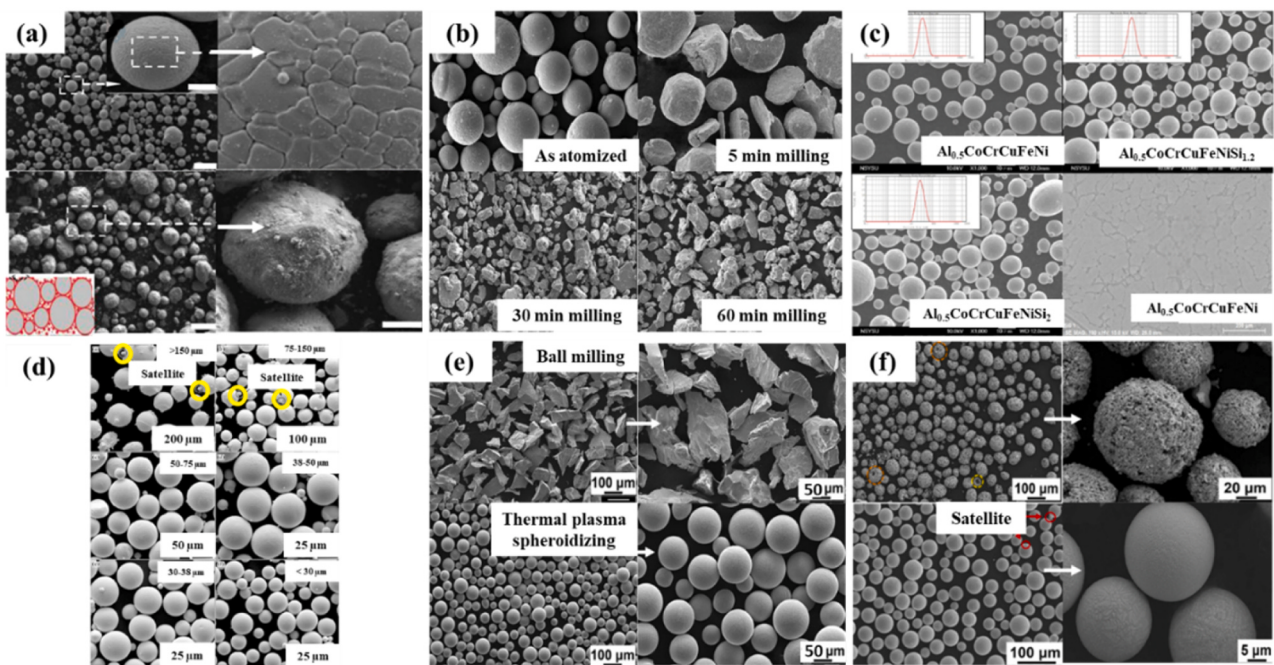


**Fig. 8.** SEM morphology of HEAs (a) TiN particles – CoCrFeMnNi HEA.

(a) Reproduced from [62], (b) CoCrFeMnNi HEA. (b) Reproduced from [66], (d) Al<sub>0.6</sub>CoCrFeNi HEA. (c) Reproduced from [70], (f) MoNbTaWZr HEA. (d) Reproduced from [63], (c) Al<sub>0.5</sub>CoCrCuFeNiSi<sub>x</sub> HEA. (e) It is reproduced from [71] with permission of the publisher (Elsevier). (f) Reproduced from [69], (e) WTaMoNbV RHEA.

analysis is used to calculate configurational entropy, reducing the complexity of the calculations involved. The VEC provides a quantitative prediction for phase structure formation in HEAs. The significance of these factors emphasizes their role in understanding and designing HEAs with desired properties and performance characteristics.

### 3. Additive manufacturing in HEA fabrication

The AM is a new technology that prints complex geometric models layer by layer of raw materials, including metals, ceramics, polymers, composites, and human tissue [51]. The 3D objects are built by two main categories - Powder Bed Fusion (PBF) and Directed Energy Deposition (DED) techniques (Fig. 7). The processes use high-energy resources such as laser and electron beams to melt the raw powders layer-by-layer through a heating or cooling rate of  $10^3$  to  $10^8$  K/s. In DED methods, the raw metals are melted into powders and wire form through high energy sources such as electron beam, laser, or electric arc. It includes Laser Engineering Net Shaping (LENS), Direct Metal Deposition (DMD), Direct Laser Deposition (DLD), and Laser Metal Deposition (LMD) [52, 53]. In PBF, laser or electron beams are usually employed to melt the raw metals in the form of powders such as Ti and nylon on the substrate in a powder bed layer by layer [15]. It includes Selective Laser Melting (SLM), Direct Metal Laser Sintering (DMLS), Selective Laser Sintering (SLS), and Electron Beam Melting (EBM) [15]. Among the various PBF methods, the SLM process is the most frequently used technique in the automotive, aerospace, defense, and medical industries due to its short fabrication time, economical process, and suitability for manufacturing both small and large complex products [54]. In SLM, localized heating and rapid solidification lead to fast cooling rates, which contribute to enhanced mechanical properties such as high strength and hardness [55]. However, the uneven microstructures and residual stresses induced in the AM process are a result of the rapid heating and cooling. The heat treatment process helps achieve a fine surface finish, stability, microstructural refinement, and improved mechanical properties by minimizing residual stress and porosity [56].

#### 3.1. Integration of AM with HEAs

The flowability of powder plays a vital role in AM in achieving a homogeneous distribution and packing density, thereby improving the strengthening properties. The near-net shape is achieved in the developed AM products through an effective feedstock of powders using laser and electron beam energy. Spherical and near-spherical shaped powders exhibit sufficient flow characteristics, resulting in improved surfaces and reduced manufacturing defects such as porosity, blow holes, and cracks. Therefore, the use of fine spherical powders is highly desirable for AM. Commonly employed methods for fabricating spherical-shaped powders to enhance flowability during AM include ball milling (mechanical mixture), gas atomization, and inductively integrated thermal plasma spheroidizing [57].

##### 3.1.1. Ball milling

High-energy planetary ball milling is one of the mechanical alloying methods used to fabricate near-spherical HEAs for the AM process, providing an economical and straightforward approach. Obtaining a fine and spherical shape for HEAs is crucial, and it relies on several factors, including milling speed, duration, ball-to-powder ratio, elemental materials, milling environments, temperature, and post-processing techniques [58,59]. Therefore, optimizing these parameters is essential for obtaining near-spherical powders. Notably, by optimizing the parameters to moderate speed and a low ball-to-powder ratio, significant progress can be made in achieving the near-spherical morphology of the powders [60].  $\text{Al}_{0.8}\text{Co}_{0.5}\text{Cr}_{1.5}\text{CuFeNi}$  HEA was fabricated by high-energy ball milling, which produces spherical fragment particles of size 10.4–16.1 nm for 48 hours. A 15:1 ball-to-powder ratio leads to fine spherical particles by collision and grinding, whereas

Ar environments avoid oxidation during the synthesis [61]. 12 wt% TiN powders are mixed with gas atomized pre-alloyed CoCrFeMnNi powder by ball milling with 150 rpm for 2 hrs in Ar atmosphere [62]. These pre-alloyed powders (41.5  $\mu\text{m}$ ) are refined to less than 2  $\mu\text{m}$  for AM through SLM. Fine spherical morphology of pre-alloyed powders is almost retained near spherical morphology by ball milling with a strong texture (Fig. 8a). The free-state TiN particles occupy gaps within pre-alloyed powders to enhance packing density. The pre-alloyed gas atomization CoCrFeMnNi HEAs are subjected to 800 rpm ball milling for 60 min. Ball-milled powders exhibit an enhanced strengthening and sintering ability by refined microstructure. A 97  $\mu\text{m}$  fine spherical shape gas atomized powder is refined to a partial spherical morphology of 30  $\mu\text{m}$  after 60 min of milling time by severe plastic deformation (Fig. 8b). The hardness and yield strength of milled powders are increased by 40% and 64.7% respectively [63].

##### 3.1.2. Gas atomization

Gas atomization is one of the methods of atomization used to fabricate a fine spherical morphology powder for the AM process. The better flowability and high thermomechanical stability of prepared powders lead to enhanced mechanical properties through densely packed components [57,64,65].  $\text{Al}_{0.5}\text{CoCrCuFeNiSi}_x$  ( $X=0,1,2,2$ ) HEAs are fabricated by gas atomization in a nitrogen atmosphere. The powder exhibits a fine spherical morphology of 27 nm size and is distributed homogeneously (Fig. 8c). A 73.3% hardness is improved due to the effect of solid solution strengthening by the addition of Si element, which reduces segregation due to a fast-cooling rate. A high crystallinity of HEAs is potentially used for the AM process [66].  $\text{AlCoCrCuFeNi}$  HEA is synthesized by gas atomization in an Ar atmosphere. The spherical morphology of powders is distributed homogeneously in the range of 2–98.1  $\mu\text{m}$  with an average of 27.2  $\mu\text{m}$ . The synthesized powders are effectively applied to the SLM-AM process for 40–50  $\mu\text{m}$  layer thickness. The SLM-processed HEA offers an increased hardness of 29.5% over the traditionally fabricated powders [67]. The gas atomization is used to fabricate  $\text{AlCrCoNiCu}$  HEA with FCC phase structure. The prepared powder exhibits a spherical shape of 10–50  $\mu\text{m}$ , which leads to better flowability and uniform composition for stable performance [68].  $\text{Al}_{0.6}\text{CoCrFeNi}$  HEA is synthesized by high-pressure gas atomization, which produces a spherical shape of powders in the range of 75–150  $\mu\text{m}$  with a mean of 78.65  $\mu\text{m}$ . The refined particles are attained by the increment of cooling rate by  $1.11 \times 10^6$  from  $3.19 \times 10^4$  K/s. Finer particles are more likely to adhere to the surface compared to larger particles. Moreover, larger particles require more time to solidify than fine particles. By reducing the particle size, planar crystals exhibit more uniform and finer particles (Fig. 8d). The FCC phase transitions to a combination of FCC and BCC phases, and eventually transforms into a fully BCC phase structure as a result of the refined grain size [69]. The gas atomization process is commonly employed under the vacuum or argon/nitrogen environments to avoid the oxidation and low oxygen content required for AM circumvents from porosity.

##### 3.1.3. Inductively coupled thermal plasma spheroidizing

The thermal plasma spheroidizing process is integrated with ball milling for synthesizing Refractory High Entropy Alloy (RHEA) powders, which are challenging to fabricate using gas atomization. The irregularly shaped ball-milled  $\text{WTaMoNbV}$  RHEA is transformed into a fine spherical shape through spheroidizing using inductively coupled thermal plasma exclusively designed for the AM process. A 25–63  $\mu\text{m}$  size ball-milled powders are subjected to  $10^4$  K thermal plasma processing to attain a homogeneously distributed 45.1  $\mu\text{m}$  (Fig. 8e). A BCC phase structure with nearly 3.194 Å lattice parameter is retrieved after synthesizing [70]. The lightweight RHEAs exhibit exceptional mechanical properties such as high yield strength and elongation [72]. A fine spherical shape of RHEA- $\text{WTaMoNbZr}$  is fabricated by plasma spheroidization from disk-milled powder. The alloy ingot is melted and hydrogenated by vacuum EBM and a compressive stress of 1973 MPa

**Table 1**

summarizes data on synthesized HEAs and induced phase structures for various AM processes.

HEAs	Synthesis methods	Phase	Powder size ( $\mu\text{m}$ )	AM	Ref.
CoCrFeNiMn (CrMnFeCoNi) <sub>1-x</sub> Fe <sub>x</sub>	Gas atomization	FCC	-	SLM	[62]
	-	FCC	130	LMD	[74]
		BCC			
CrMnFeCoNi	-	FCC	120	LMD	[75]
MoNbTaW	-	BCC	45–150	DED	[76]
AlCoCrCuFeNiTi	Gas atomization	FCC, B2 phase	27.2	SLM	[67]
WTaMoNbZr	Plasma spheroidization	BCC	12.1–66.8	Vacuum EDM	[73]
VNbMoTaW	Plasma spheroidization	BCC	15–53	SLM	[77]
Ni <sub>2.1</sub> CoCrFeNb <sub>0.2</sub>	Plasma-rotating electrode process	FCC, Laves, and Nb carbide phase.	-	DLD	[78]
Al <sub>0.3</sub> CoCrFeNi	Gas atomization	FCC and B2 phase	110	LMD	[79]
AlCoCrFeNi <sub>2.1</sub>	Gas atomization	BCC and FCC	75–150	DLD	[80]
CoCrFeNiMn	-	FCC	50–100	LENS	[81]
Al <sub>0.3</sub> CoCrFeNi	-	FCC	50	LENS	[82]
AlCoCrFeNiTi <sub>0.5</sub>	Gas atomization	BCC (B2-order) & BCC (A2-disorder)	5–120	LENS	[83]
AlCrFeMoV <sub>x</sub>	-	BCC	-	LENS	[84]
CoCrFeMnNi	Gas atomization	FCC	45–75	LENS	[85]
ZrTiVCrFeNi	-	C14 lave phase	0.5–260	LENS	[86]
SiFeCoCrNi	3D Mixer	FCC	15–53	SLM	[87]
AlCoFeNi <sub>1.9</sub> V <sub>0.9</sub> Sm <sub>0.1</sub> AlCoFeNiV <sub>0.9</sub> Sm <sub>0.1</sub>	-	FCC	20–80	SLM	[88]
FeCoCrNi	-	FCC	-	SLM	[89]
CoCrFeMnNi	Arc melting and Mechanical milling	FCC	27.2	SLM	[90]
AlCoCrFeMnNi	Gas atomization	BCC	<90	SLM	[91]
Ni <sub>6</sub> Cr <sub>4</sub> WFe <sub>9</sub> Ti	Gas atomization	FCC	15–53	SLM	[92]
CoCrFeMnNi	Gas atomization	FCC	20–80	SLM	[93]
Al <sub>0.2</sub> Co <sub>1.5</sub> CrFeNi <sub>1.5</sub> Ti <sub>0.3</sub>	Gas atomization	FCC	65	SLM	[94]
Al <sub>x</sub> CrCuFeNi <sub>2</sub>	-	BCC			
Al <sub>x</sub> CrCuFeNi <sub>2</sub>	-	FCC	27–33	SLM	[95]
CoCrFeMnNi	-	-	5.98–15.66	SLM	[96]
TiZrNbMoV	-	BCC	50–100	LENS	[97]
CoCrFeMnNi	Gas atomization	BCC	15–53	Laser PBF	[98]
CrMnFeCoNi	-	FCC	120	LMD	[99]
CoCrFeMnNi	-	FCC	9.7–50.4	LMD	[100]
CoCrFeNiTi	Gas atomization	FCC	<45	SLM	[101]
CoCrFeNiW <sub>0.2</sub>	Gas atomization	FCC	15–45	SLM	[102]
CoCr <sub>2.5</sub> FeNi <sub>2</sub> TiW <sub>0.5</sub>	-	BCC	25–65	SLM	[103]
CoCrFeMnNi	-	FCC	0.2–1	LMD	[104]
CoCrFeNb <sub>x</sub>	Plasma rotation electrode process	FCC	50–150	LMD	[105]
FeCoCrNiMn	Gas atomization	FCC	<53	SLM	[106]

with a 17.63% strain. A distributed range of 1.56–59.5  $\mu\text{m}$  size irregular milled powders are refined to 37.5  $\mu\text{m}$  fine spherical powders with BCC phase structure by spheroidization for a potential application of the AM process [73]. The spray granulation MoNbTaWZr HEA is refined to a fine spherical shape by plasma spheroidization. The subsequent process exhibits a flowability of 8.89 s/50 g with a dense structure of 7.27 g/cm<sup>3</sup>. The spherical, bowl, and apple-shaped 45.7  $\mu\text{m}$  spray granulation MoNbTaWZr HEAs are transformed to a mean size of 43.2  $\mu\text{m}$  particles with a smooth and good sphericity burr-free surface are obtained by plasma spheroidization (Fig. 8f). The most of finer particles of granulated HEAs are varnished by absorbing sufficient heat at a high plasma temperature of 10<sup>4</sup> K. The granulated powders melt instantly by feeding plasma flow. The evaporation of finer particles is the foremost reason for the high mean particle size by plasma spheroidization [71]. In the fabrication of HEAs for AM, the attainment of optimal powder flowability is crucial to achieve a homogeneous distribution and packing density, thereby enhancing strengthening properties. The use of spherical or near-spherical powders is highly desirable to minimize manufacturing defects such as porosity and cracks. Table 1 provides an overview of the different synthesis methods utilized to fabricate various HEA elemental compositions for the AM process and the resulting developed phase structure concerning powder size.

### 3.2. Benefits of AM in HEA fabrication

HEA powders can be utilized in bulk form or reinforced with base materials through various fabrication processes, including arc melting, induction melting, vacuum arc melting, spark plasma sintering, hot

pressing, powder metallurgy, and AM. Among these processes, the AM process offers numerous advantages over conventional manufacturing methods. Table 2 highlights the benefits of the AM process in comparison to traditional fabrication techniques.

The AM process offers design freedom, allowing for the production of complex geometrical shapes that are challenging to achieve using traditional manufacturing methods. The exceptional strength and ductility of AM-processed CoCrFeNi HEAs are attributed to the complexity and geometrical freedom of the design [107]. Compared to arc melting, AM is a bottom-up technique that provides better material usage and sample construction through design freedom [108]. Materials utilization in the AM process involves building samples layer by layer, typically ranging from 25 to 150  $\mu\text{m}$ . This method results in higher densification, reduced porosity, and minimized material waste compared to traditional fabrication techniques. For HEAs, effective material utilization is crucial in achieving a single-phase structure during synthesis [109]. The mechanical properties of AM-built samples depend on factors such as the feed rate of materials, layer thickness, and build orientation angle [110]. Minimizing material waste and implementing recycling practices are significant aspects of modern manufacturing industries to control pollution [111]. The AM process enhances the material properties of the built samples, including improved mechanical properties, wear resistance, and corrosion resistance compared to conventional fabrication processes. These desirable characteristics, including the unique microstructure, high homogeneity, high density, reduced porosity, and preservation of the single-phase solid solution, are achieved in HEAs. The optimization of AM process parameters, such as laser power, scan speed, hatching space, layer

**Table 2**

Benefits of the AM process.

Sl. No.	Benefits of the AM process
1.	<b>Design freedom:</b> <ul style="list-style-type: none"> <li>The intricate shapes with complex geometries can be effortlessly manufactured at an affordable cost.</li> <li>The customized parts and nanoscale-level components are effectively produced.</li> <li>The AM process achieved a near-net shape without any additional process.</li> <li>The AM can produce multifunctional parts (functional integration), which minimizes the number of parts and reduces the assembly.</li> <li>The modification and customization of models are effectively completed with the help of 3D CAD modeling.</li> </ul>
2.	<b>Special tooling cost:</b> <ul style="list-style-type: none"> <li>The AM process does not require any special tools or attachments for intricate shapes.</li> <li>Direct production is done from 3D models without any intermediate tools or molds.</li> </ul>
3.	<b>Materials utilization:</b> <ul style="list-style-type: none"> <li>The layer-by-layer production of the AM process minimizes the material loss during the fabrication, and the raw materials are effectively utilized.</li> <li>The mesh-type production of the AM leads to a high strength-to-weight ratio.</li> </ul>
4.	<b>Properties of AM-built samples:</b> <ul style="list-style-type: none"> <li>The AM printed sample exhibits high strength, hardness, tribological properties, and excellent corrosion resistance by controlling the process parameters.</li> <li>The AM processed structures including honeycomb, lattices, and foams attributed to a high strength to weight ratio, and high stiffness than the conventional manufacturing process.</li> <li>The process reduces the inventory cost and minimizing the porosity of final components.</li> </ul>

thickness, and feed rate, contributes to improved microstructures [112]. However, samples produced by AM often exhibit porosity, which diminishes the properties of the final products. Therefore, post-processing techniques such as hot compression, hot isostatic pressing, infiltration, and spark plasma sintering are employed to reduce internal porosity and improve material densification [113]. Parameters such as laser power, scanning speed, and feed rate are optimized through experimental design to enhance hardness by improving the microstructure. The AM process enables rapid prototyping by facilitating the creation of complex geometric shapes through the optimized design of AM-built samples. The exceptional features of AM are extensively utilized in engineering and medical applications, allowing for the exploration of new compositions and processing techniques. Comparatively, AM offers significant advantages over traditional fabrication methods, including reduced lead time through faster iteration, design freedom, and process optimization. It is particularly well-suited for fabricating new compositions, small-batch production, and prototype models [21].

### 3.3. Challenges of AM in HEA fabrication

The AM process provides numerous features that enhance the properties of built samples for various applications. However, researchers face particular challenges during the fabrication of HEAs using the AM process, including materials usage, process parameters, post-processing, and microstructural changes. Table 3 illustrates the challenges encountered during the AM process in HEA fabrication.

The AM process is suitable for a wide range of materials, including metallic materials, biomaterials, polymers, and ceramics [114,115]. In the case of HEAs, various categories of elements, including lightweight, refractory, and transition elements, can be utilized in the AM process. However, brittle materials, highly reactive, possess elastic properties, have extremely high melting temperatures, are toxic, or have low

**Table 3**

Challenges of the AM in HEA fabrication.

Sl. No.	Challenges of the AM process
1.	<b>Production:</b> <ul style="list-style-type: none"> <li>The AM process is more suitable for rapid prototyping and batch production. The process is not economical for the mass production.</li> <li>The layer-by-layer production of the AM process is attributed to increasing lead time.</li> <li>The AM process is cost-effective due to the lower production speed compared to conventional methods.</li> </ul>
2.	<b>Size of the product:</b> <ul style="list-style-type: none"> <li>The AM process is not suitable for significant components due to the equipment capacity, lead time, and raw materials.</li> <li>The process is more significant for micro and nano-sized components.</li> <li>Achieving a high dimensional accuracy and tolerance can be difficult for large and complex geometric components.</li> </ul>
3.	<b>Post-processing:</b> <ul style="list-style-type: none"> <li>Post-processing, including heat treatment, HIP, etc, is required to further improvements of properties such as mechanical properties, surface finish, and quality.</li> <li>Additional processes such as heat, pressure, and binding agents are required to deposit two or more layers over the base substrate.</li> </ul>
4.	<b>Materials availability:</b> <ul style="list-style-type: none"> <li>The AM process is limited to certain materials like metals, polymers, and ceramics.</li> <li>The highly reactive, brittle nature and high melting materials are not suitable for the AM fabrication methods.</li> <li>The thermal expansion of elements, warping, and layer adhesion can affect the final dimensions of the printed components.</li> </ul>
5.	<b>Cost considerations:</b> <ul style="list-style-type: none"> <li>The initial investment of AM equipment (3D printers and software) is expensive for capable of producing parts with high precision and speed.</li> <li>The raw materials used in the AM process are economically high for aerospace and medical applications.</li> <li>Significant maintenance is frequently required for the smooth processing of AM equipment.</li> </ul>
6.	<b>Process parameters:</b> <ul style="list-style-type: none"> <li>The AM process parameters, including laser power, layer thickness, scanning speed, and hatching space, need to be optimized to achieve the desired microstructure and properties.</li> <li>The process parameters are controlled tightly to maintain reproducibility across the multiple prints. The accurate process parameters minimized the variability and defects of processed samples.</li> </ul>

filament quality, are not suitable for AM [112]. Process optimization is crucial in AM and relies on parameters of scanning speed, laser power, hatching distance, building orientation, and layer thickness. These parameters directly impact the microstructure, mechanical properties, wear resistance, and corrosion behavior of the built samples. The solidification rate, controlled by laser power and energy density, influences the microstructural features such as grain size and phase structures. Low scanning speeds result in coarse grains, while higher scanning speeds lead to finer grains but insufficient bonding between layers. The layer thickness affects grain bonding and processing time, with improper parameters contributing to defects like porosity, cracks, pores, and foreign material inclusions [25]. Morphological analysis of AM-built samples reveals essential characteristics such as uniform grain distribution, phase formation, stability, densification, porosity, chemical homogeneity, mechanical properties, and texture. The size and dispersion of grains contribute to improved mechanical properties through mechanisms like grain boundary strengthening, solid solution strengthening, and precipitation strengthening. The formation and stability of phase structures also play a role in enhancing strength. By optimizing process parameters solidification rate, and implementing post-processing techniques, the microstructure and properties of AM-built samples can be effectively improved. Post-processing of

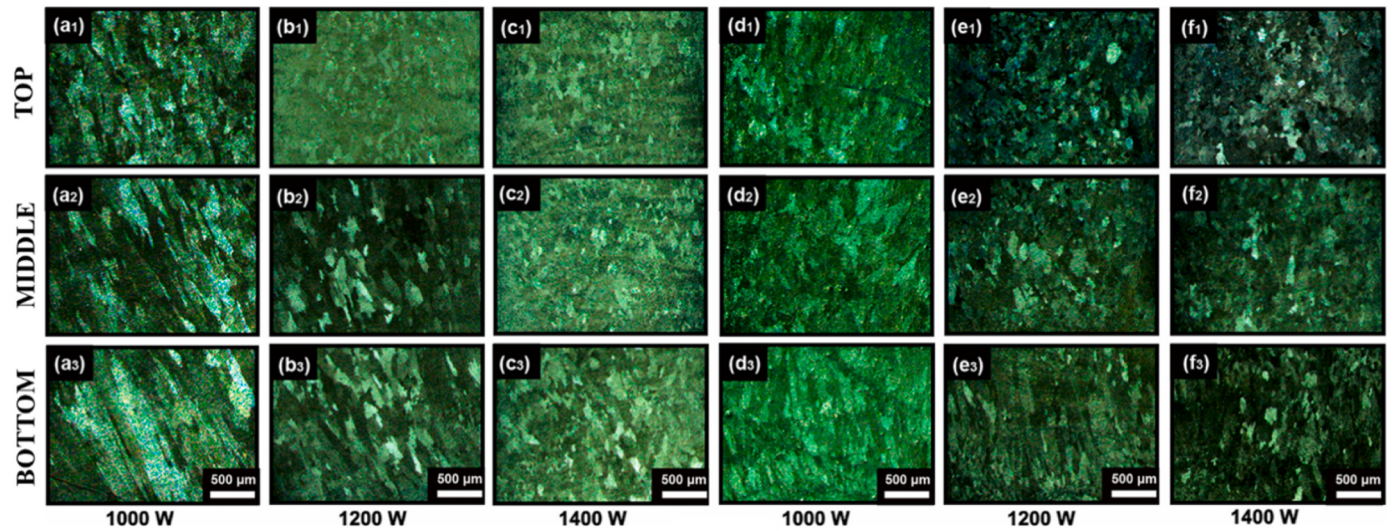


**Fig. 9.** Metallographic structures of LMD CrMnFeCoNi HEA with scanning strategies of (a-c) single direction, (d-f) dual direction. It is reproduced from [121] with permission of the publisher (Elsevier).

AM-built samples is essential for enhancing mechanical properties by reducing porosity and making microstructural modifications [116]. However, it should be noted that heat treatment processes can lead to the formation of secondary phases, which may negatively impact the properties of the built samples. For example, in the heat treatment of AlCrFeCoNi HEA-built samples, the formation of the sigma phase, along with FCC and BCC/B2 phase structures, can occur [117]. Cost considerations are a crucial aspect of the AM process. The equipment and HEAs used in AM can be economically expensive. Furthermore, the

maintenance and processing costs associated with AM are slightly higher compared to conventional manufacturing methods. Precise control units are necessary to optimize process parameters such as power, temperature, feed rate, and scanning speed [21,118].

#### 4. Microstructural aspects and phase formation in AM-built HEAs

The microstructure and phase formation are critical factors that

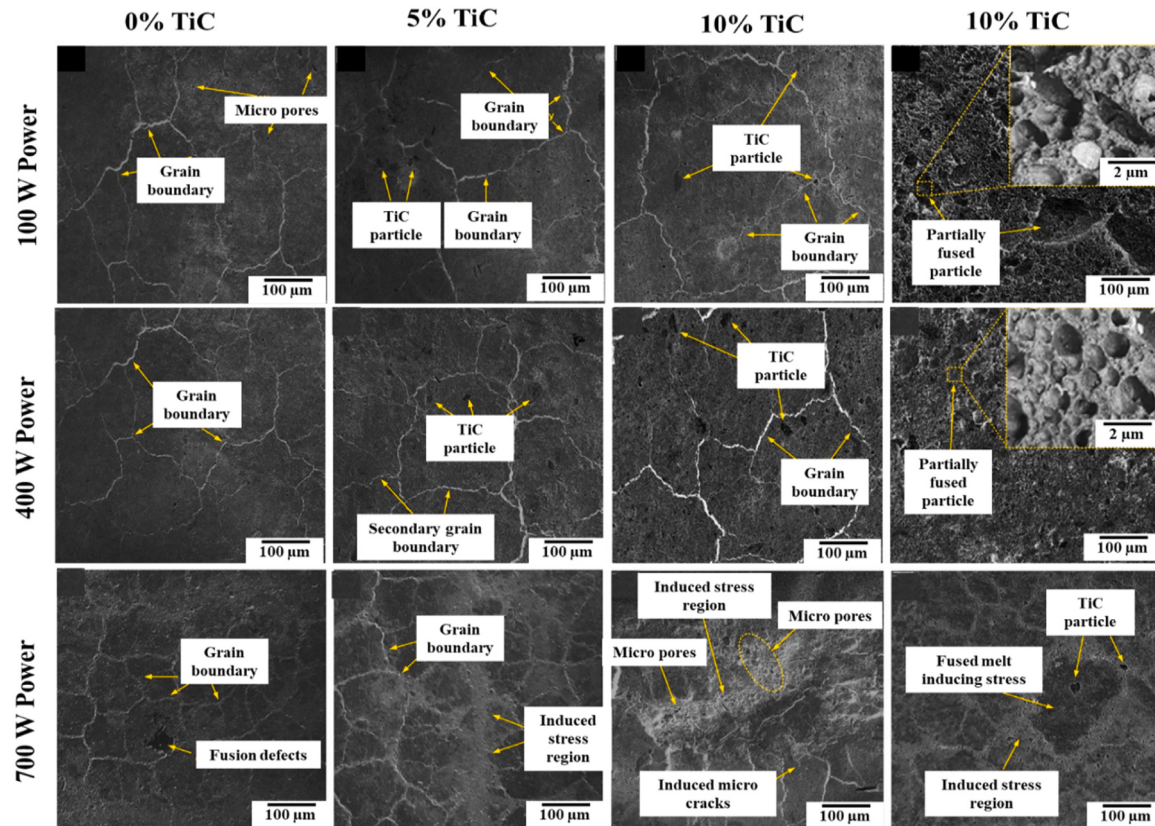


**Fig. 10.** Morphological evaluation of 0, 5, 10, and 15% TiC addition of CoCrFeMnNi HEA under different laser power. It is reproduced from [123] with permission of the publisher (Elsevier).

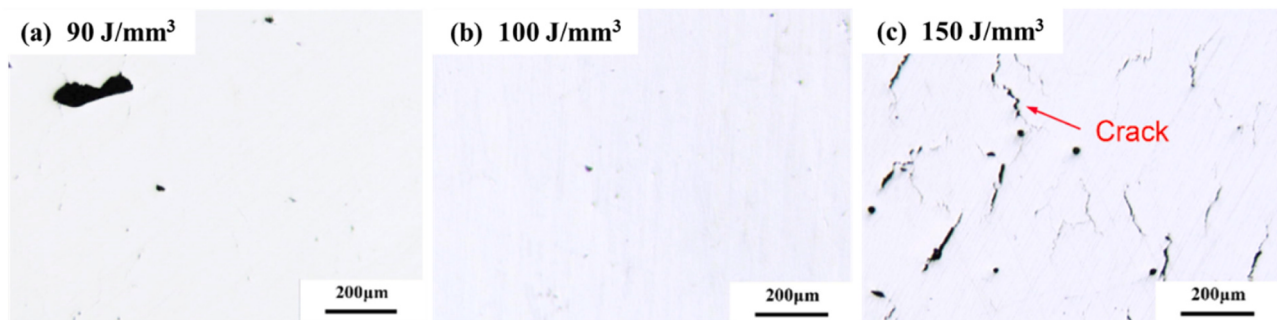


**Fig. 11.** Optical microscopy of SLM processed  $\text{Al}_{0.3}\text{CoCrFeNiCu}$  HEA (a)  $90 \text{ J/mm}^3$  VED, (b)  $100 \text{ J/mm}^3$  VED, (c)  $150 \text{ J/mm}^3$  VED. It was reproduced from [128] with permission of the publisher (Elsevier).

determine the mechanical properties of AM-built samples. The AM process parameters, including laser power, scanning speed, hatching space, and layer thickness, play a significant role in producing a fine microstructure and a single-solid phase. These parameters are optimized through the design of experiments to achieve optimal results and desired material properties [119].

#### 4.1. Influence of AM process parameters on microstructure

The AM-SLM process is used to build an  $\text{Al}_{0.5}\text{CoCrFeNi}$  HEA sample with varying process parameters of laser power, scanning speed, and hatching space. A 99.92% relative density is achieved by 320 W laser power, 800 mm/s scanning speed, and 60  $\mu\text{m}$  hatching space. The cracks and pores are exhibited in the built sample due to the insufficient molten flow, which generates a harsh balling phenomenon. The non-melting particles and cracks are minimized by increasing the laser power. The heat accumulation of HEA powders and molten temperature is decreased with the addition of scanning speed and hatching space [120]. The effect of laser power and scanning strategies analyzes the microstructure of AM-LMD processed  $\text{CrMnFeCoNi}$  HEA samples. A significant impact of columnar to equiaxed transitions (CET) is observed on the microstructure of AM-built samples due to the temperature gradient and heat flux direction. The microstructure and crystal growth of LMD

samples are demonstrated in the metallographic structures (Fig. 9). The columnar to equiaxed grains are varied from the bottom to the top surface of samples with different laser power. The dual direction exhibits more equiaxed grains with higher laser power than the single direction. The refined and equiaxed grains are achieved on the entire regions of a built sample at 1400 W laser power. The rapid cooling rate and small molten size lead to a solute-trapping effect and prevent the elemental segregation that improves the distribution of the elements homogeneously [121]. The laser cladding is employed to fabricate  $\text{FeNi-CoCrTi}_{0.5}$  HEA by scanning speed of 4–8 mm/s and specific energy of 54.17–108.33  $\text{J/mm}^2$  along with a laser power of 1000–1600 W. The columnar and dendritic structures are improved with the addition of particular energy. A  $72.22 \text{ J/mm}^2$  specific energy offers a higher microhardness and wear resistance through the improved microstructure with the absence of cracks and pores [122].

The AM-SLM process is used to fabricate  $\text{CoCrFeMnNi}$  HEA with 5–15% TiC powders to enhance the strength with different laser power. The microstructure of the SLM-built samples under the 100, 400, and 700 W laser power is shown in Fig. 10. A micro pores and partially fused particles are exhibited under the 100 W laser power. A 400 W laser-powered sample exhibits minimized pores and refined grains of 18.88  $\mu\text{m}$  due to the fast solidification rates. Some of the regions of 700 W laser-powered samples demonstrate induced stress region,

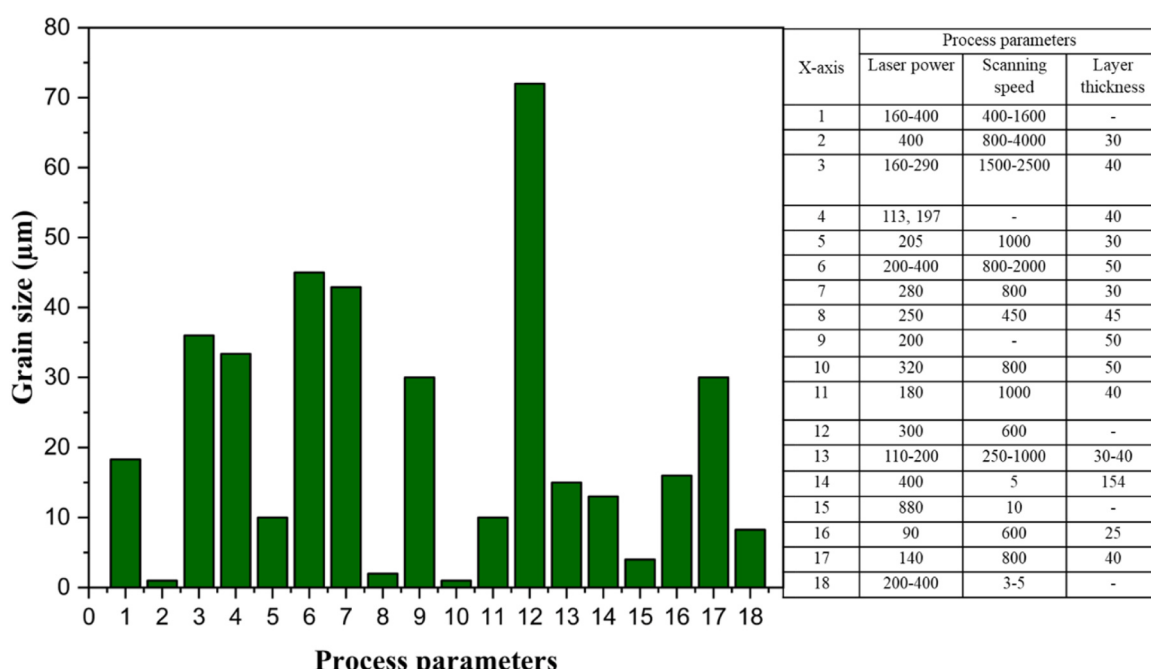


**Fig. 12.** Influence of process parameters on the grain size of AM processed HEAs.

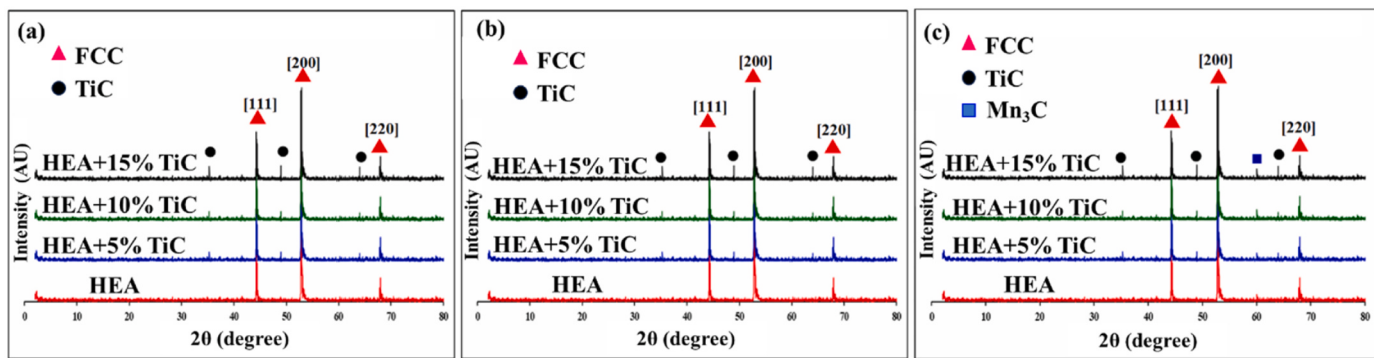


**Fig. 13.** Phase structure of SLM processed CoCrFeMnNi HEAs (a) 100 W laser power, (b) 400 W laser power, (c) 700 W laser power. It is reproduced from [123] with permission of the publisher (Elsevier).

micropores, and cracks ascribed to decreased strength. A 10% TiC with 400 W laser-powered sample exhibits a higher microhardness and UTS by enhanced densification with minimum porosity [123]. The laser deposition techniques used to build AlCoCrFeNiCu and AlTiCrFeCoNi HEA with the effect of 600, 800 W laser power, 4,8, and 12 mm/s scanning speed. The columnar dendritic and equiaxed dendritic structures are exhibited on the AlCoCrFeNiCu and AlTiCrFeCoNi HEA samples. The minimum scanning speed and high laser power lead to a high microhardness due to the higher solidification rate. A 1.54496 mm and 1.34272 mm clad height is obtained on the Cu and Ti-based HEA samples at the 800 W laser power [124]. The AM-SLM process is effectively employed to add TiC with FeCoCrNiMn HEA. The 99.0% relative density is attained under the 150 J/mm<sup>3</sup> VED, 300 W laser power, and 400 mm/s scanning speed. The excellent dense structure of the built sample is attributed to higher yield strength and notch fracture toughness of 725 MPa and 81.0 MPa. m<sup>0.5</sup> respectively [125].

The AlTiCrFeCoNi and AlCoCrFeNiCu HEAs are coated on an A301 steel plate through the AM-LAM process to achieve excellent structural properties on aerospace components. A defect-free homogenous distributed coating is attained by the optimized process parameters of 1200–1600 W laser power and 8–12 mms scanning speed with 50%

overlap [126]. A higher energy density in the AM process leads to the production of high-densification samples by increasing the fluidity of the HEA material. The elevated temperature of the molten pool effectively fills any developed pores, resulting in a higher density of the final product [127]. In the AM-SLM process, an Al0.3CoCrFeNiCu HEA sample is fabricated with varying scanning speeds and laser power. The built sample exhibits columnar grains aligned in the building direction of the SLM process. The Volumetric Energy Density (VED), scanning speeds, and laser power directly influence the density of the built sample. When a 90 J/mm<sup>3</sup> VED is employed, irregularly large pores are observed, resulting in un-melted particles due to an insufficient VED (Fig. 11a). However, a high relative density of 99.1% is achieved with a VED of 100 J/mm<sup>3</sup>, along with 500 mm/s scanning speed and 150 W laser power. The complete melt pool formation increases the fluidity of the material, effectively filling the pores and cracks, thus resulting in higher density (Fig. 11b). On the other hand, a much higher VED of 150 J/mm<sup>3</sup> leads to low density due to the formation of hot crack regions (Fig. 11c) [128]. The different AM processes, such as SLM, LMD, and laser cladding, have been extensively investigated for fabricating HEA samples with improved structural properties. The optimization of process parameters, including laser power, scanning speed, and

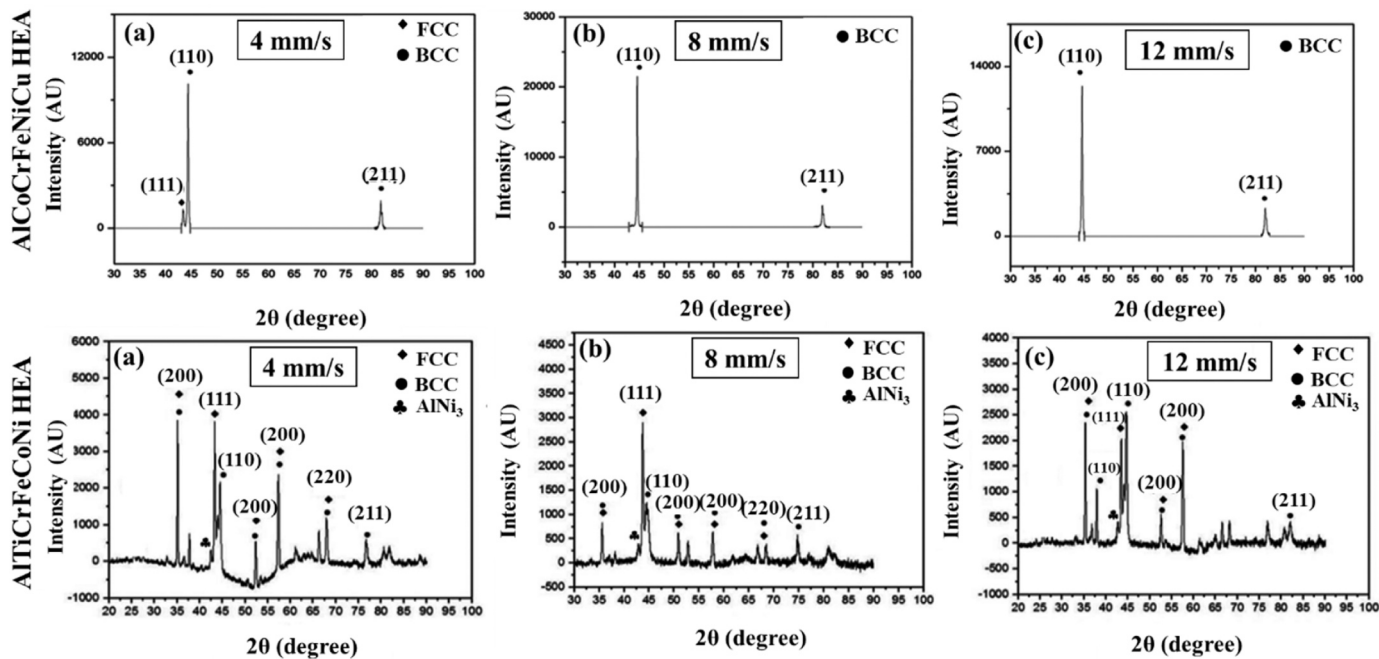


**Fig. 14.** Phase structure of AlCoCrFeNiCu and AlTiCrFeCoNi HEAs (a) 4 mm/s, (b) 8 mm/s, (c) 12 mm/s of scanning speed. It is reproduced from [124] with permission of the publisher (Elsevier).

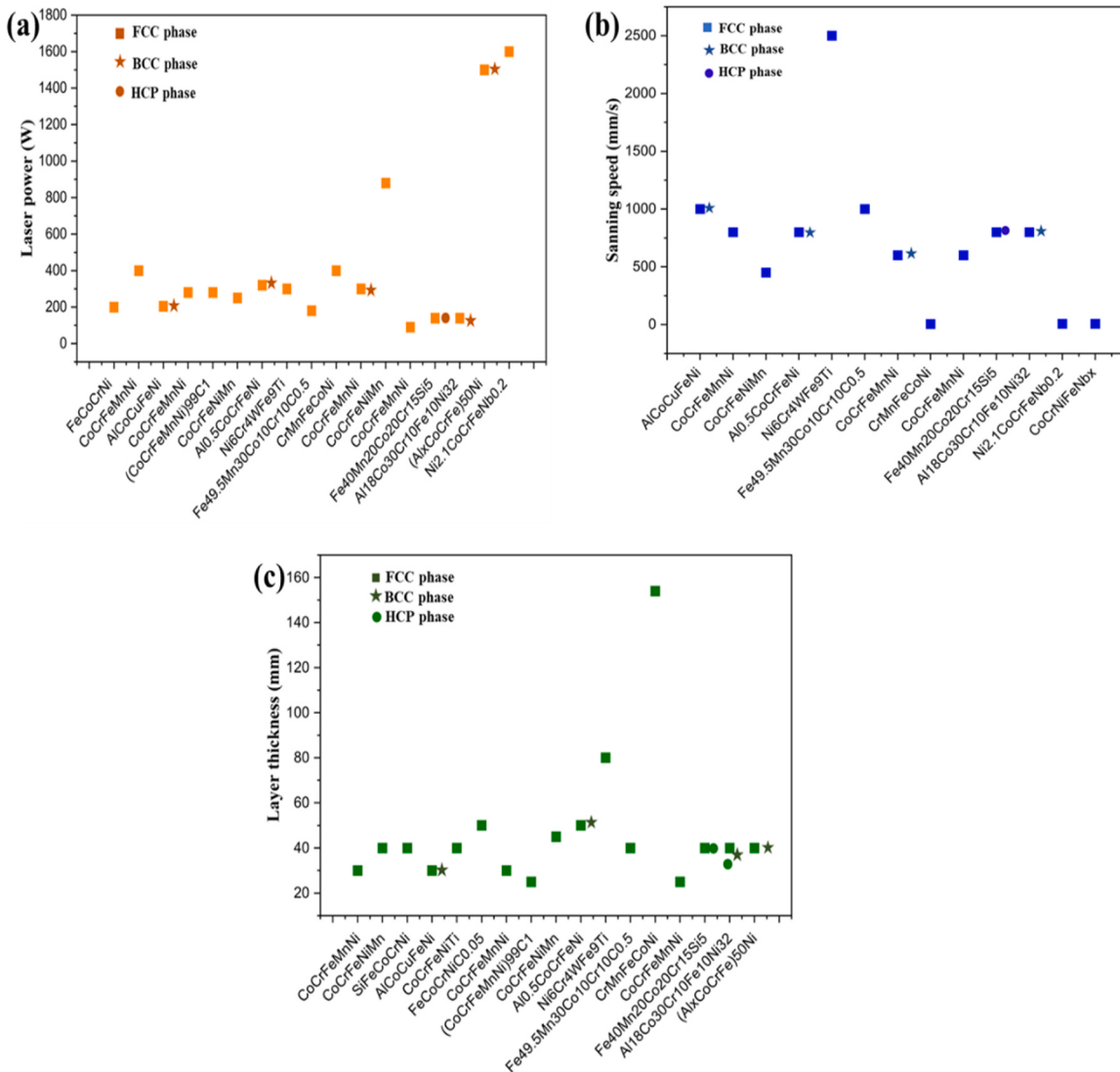


**Fig. 15.** Effect of process parameters on phase structure of HEAs (a) Laser power, (b) Scanning speed, (c) Layer thickness.

hatching space, is crucial in achieving significant microstructures and desirable mechanical properties. Higher laser power tends to minimize cracks and pores while promoting the formation of finer grains and enhanced densification. Additionally, the AM-LAM process provides defect-free coatings with excellent structural properties, making it suitable for aerospace components. A comprehensive understanding of the interaction between process parameters and material characteristics is vital for advancing the application of HEAs in various industries. Fig. 12 demonstrates the influence of process parameters on the grain size of the AM-HEAs.

#### 4.2. Phase formation and composition control

The AM-SLM techniques are used to build CoCrFeMnNi HEA with 5–15% TiC by varying laser power. The strength and microhardness of the processed samples are improved with the addition of laser power from 100 to 400 W. Subsequently, and the properties are decreased further with the addition of laser power of 700 W. A single-phase BCC structure without any intermetallic phases are observed of samples under 100 and 400 laser power (Fig. 13 a and b). A high laser power of 700 W leads to increased melting temperature. The Mn<sub>3</sub>C is induced as a secondary phase due to the high-temperature reaction (Fig. 13c) [123]. The rapid solidification rate of the AM process leads to improvement in

the solid solution phase formation by the diffusion of atoms of HEAs. The optimized process parameters ascribe a high cooling rate, which is attributed to the rapid solidification rate [129]. The supersaturated solid solution formation is promoted by enhancing the solubility limit of HEA elements, which is obtained by rapid heating and solidification rate of laser cladding [130,131].

Laser deposition techniques are employed to build AlCoCrFeNiCu and AlTiCrFeCoNi HEA samples with 600–800 W laser power and 4–12 mm/s scanning speed. The rapid solidification rate and high mixing entropy effect are attributed to a simple solid solution phase without any intermetallic components. The XRD pattern of AlCoCrFeNiCu HEA build samples is illustrated in Fig. 14. A BCC phase with a small amount of FCC structures is observed under the 4 mm/s scan speed. A high-volume fraction of the BCC phase is exhibited with the addition of scan speed. The FCC phases are hindered due to the high cooling rate, which is attained by the effect of higher scan speed. A BCC, FCC, and a small amount of AlNi<sub>3</sub> (L12, FCC) intermetallic phase structures are exhibited in the AlTiCrFeCoNi HEA build samples (Fig. 14). The induced phase structures contribute to the enhancement of mechanical properties. As the scan speed increases, the diffraction peaks of the phases become sharper, indicating improved crystallinity [124]. A high scanning speed is attributed to a rapid cooling rate that hampers the FCC phase structure by moving FCC to BCC, which

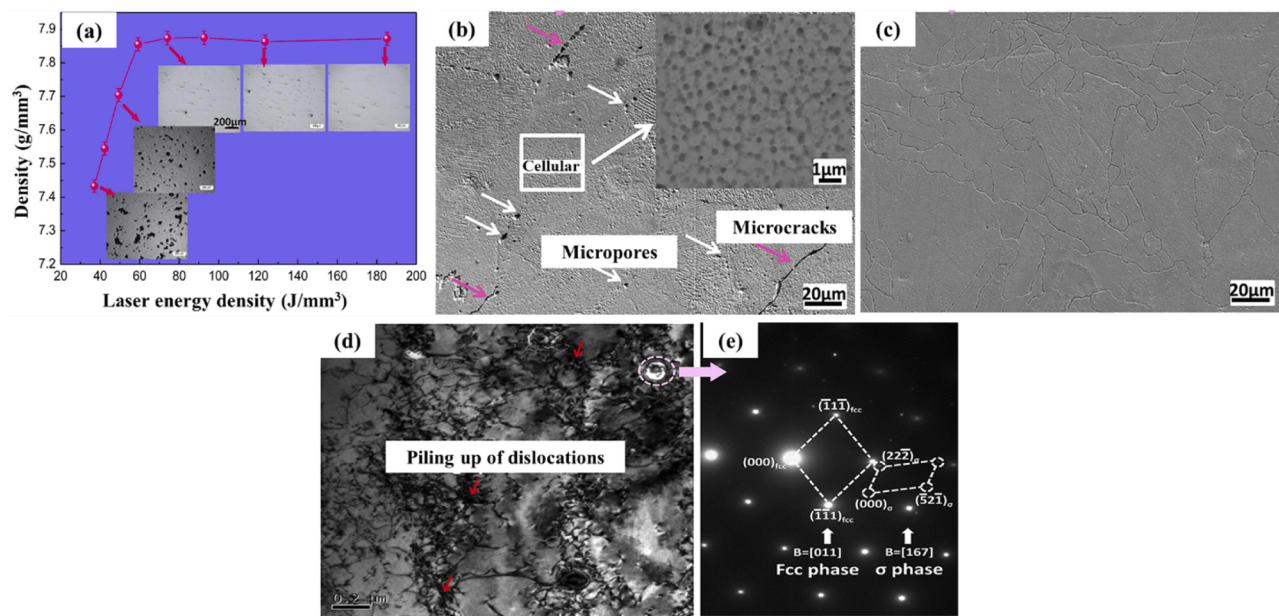


**Fig. 16.** (a) Effect of laser energy density, (b) SEM morphology of SLM printed sample, (c) SEM morphology of SLM printed HIP sample, (d) TEM image of high-density dislocation, (e) SAED pattern of SLM printed CoCrFeMnNi HEA. It was reproduced from [138] with permission of the publisher (Elsevier).

improves the mechanical properties [132,133]. The high entropy effect reduces the Gibbs free energy, which enhances the stability of the solid solution [134,135]. The AM-laser cladding is used to coat FeNiCoCrTi<sub>0.5</sub> HEA with steel 45 with optimized process parameters. The formation of a stable solid solution improves by reducing free energy due to the high entropy effect of HEA. The mixing enthalpy and entropy contribution ( $\Omega$ ) is more than 1.1, which thermodynamically supports the formation of a solid solution. The higher specific energy leads to a sizeable molten pool and elevated molten pool temperature that enhances the diffusion rate of Ti, which forms Ti-rich phases. The mismatch of elemental atomic radii with Ti elements generates the secondary phase and Ti-rich phase, which is also the reason for the second phase formation [122]. The AM process is effectively utilized to enhance the properties of built samples through the formation of a phase structure. The optimization of process parameters, including laser power, scanning speed, and layer thickness, leads to the development of a single-phase structure, which contributes to improved strength and microhardness. Rapid solidification rates and high entropy effects play crucial roles in stabilizing solid solutions and enhancing the mechanical properties of the fabricated samples. Fig. 15 presents the impact of laser power in the formation of the phase structure of the AM-HEAs.

## 5. Mechanical properties of AM-processed HEAs

### 5.1. Powder bed fusion techniques

The PBF techniques produce significant homogenous grains with the least porosity of HEAs samples. The properties of fabricated samples are majorly depending on the suitable processing parameters, the composition of elements in the HEA system, and post-processing methods [136]. The PBF techniques attain the near-net shape of products. The unique microstructure and exceptional mechanical properties are achieved due to the high cooling rate of the PBF process [137]. The equiautomic CoCrFeMnNi HEA is synthesized by gas atomization with a mean particle size of 36 μm. The SLM-AM process is employed to build a layer surface of a single-phase FCC structure. The density of the SLM-printed samples increased gradually with the increment of Volumetric Energy Density (VED) up to 74 J/mm<sup>3</sup> (Fig. 16a). The VED >74 J/mm<sup>3</sup> leads to flowability due to the high-temperature field. In addition, the Hot Isostatic Pressing (HIP) is employed to enhance the

mechanical properties by improving relative density to 99.1% through impidement of micropores and microcracks of SLM printed sample (Fig. 16b and c). The rapid solidification process in SLM printing results in the formation of high dislocation pile-up, entanglement, and kinking within the cellular grain structure, as indicated by the red arrows in Fig. 16d and e. The HIP process is employed to enhance the mechanical properties of the sample. This process increases the tensile strength to 649 MPa while reducing the elongation to 18% [138]. A 15–53 μm size spherical morphology of gas atomized Ni<sub>6</sub>Cr<sub>4</sub>WFe<sub>9</sub>Ti HEA is used to build a sample by SLM process of 300 W laser power, 2500 mm/s scanning speed, and 80 μm scanning space. A fine grain structure is obtained by the effect of a higher nucleation rate, which is higher than the growth rate. The uniform nano-particles are observed during the SLM process by dispersed coarse grain boundaries. The SLM-printed HEA sample exhibits improved yield strength and UTS by 50% and 93% over the vacuum arc melting HEA sample [92]. The equimolar CoCrFeMnNi HEA is used to fabricate a sample using the SLM process. The effect of rapid solidification and high-temperature gradients obtains the cellular subgrains with less than 5° grain boundary angles. The creep resistance is mainly dominated by the deformation of dislocation motion [93]. The spherical morphology of 22.7–65 μm size Al<sub>0.2</sub>Co<sub>1.5</sub>CrFe-Ni<sub>1.5</sub>Ti<sub>0.3</sub> HEA is synthesized by gas atomization. The SLM-printed samples are subsequently annealed at 750 °C and aged for 50 hrs. The aged SLM sample exhibits a higher yield and UTS of 1235 MPa and 1550 MPa by precipitation strengthening of the L<sub>2</sub><sub>1</sub> phase structure. Moreover, the aged SLM promotes the sub-micron dendritic segregation, nano oxides, internal stress, and dispersion of the L<sub>1</sub><sub>2</sub> phase [94]. The SLM process employed on AlCoFeNiV<sub>0.9</sub>Sm<sub>0.1</sub> and AlCoFeNiTiV<sub>0.9</sub>Sm<sub>0.1</sub> HEAs produces a high phase stability. The SLM-printed samples exhibit exceptional corrosion resistance at high temperatures [88]. The SLM process effectively fabricates a 33.6 μm mean size of Al<sub>0.75</sub>CrCuFeNi<sub>2</sub> HEA. The addition of Al leads to a columnar-to-equiaxed transition mechanism, which attributes a defect-free surface with FCC and BCC phase structures [95]. A 1.5% Si element is fabricated with equimolar FeCoCrNi HEA by the SLM process. The process optimization and remelting strategy obtain a high dense structure of 99.78%. A single-phase FCC structure of columnar grains and numerous subgrains without precipitation is obtained on the SLM-printed sample. The solid solution and dislocation loop strengthening mechanism leads to excellent tensile properties [87]. The equiautomic CoCrFeMnNi HEA is used to

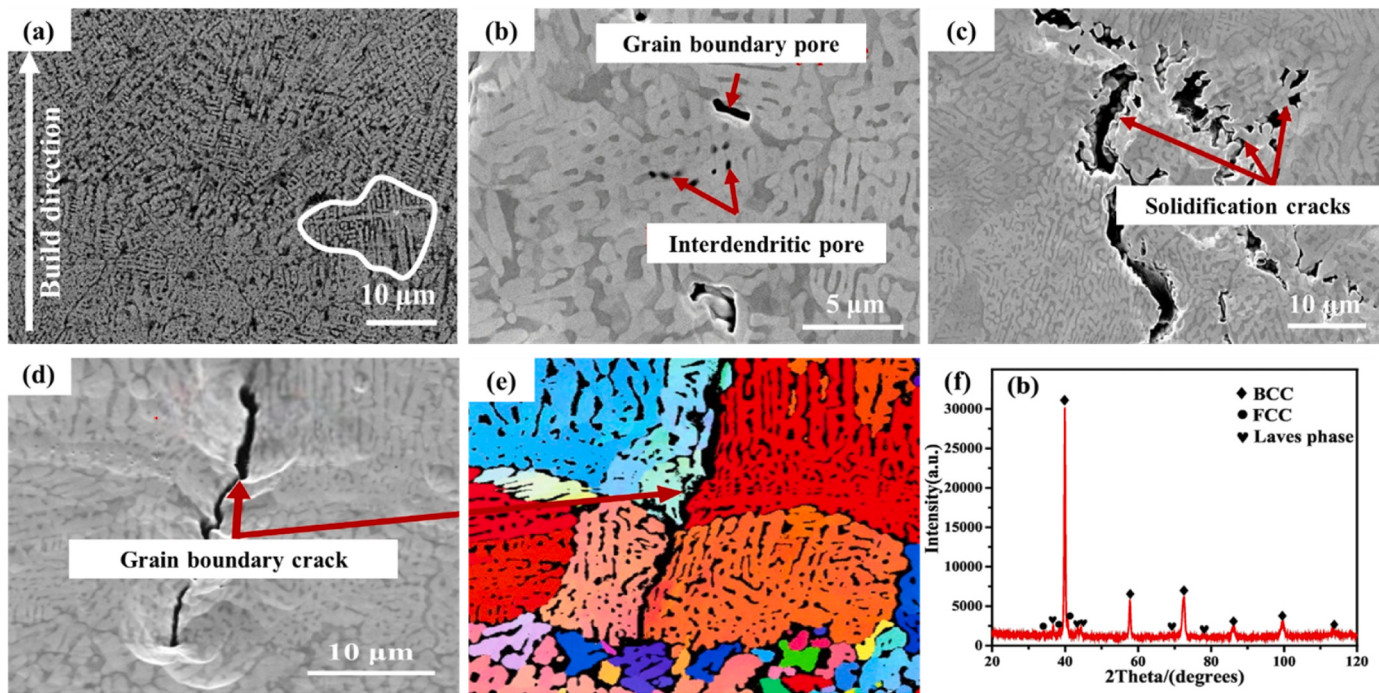


**Fig. 17.** (a) SEM image, (b) Porosity, (c) Solidification cracks, (d) Secondary electron mode of grain boundary crack, (e) IPF mode of grain boundary crack, and (f) XRD pattern of SEBM-processed WMoTaNbVFeCoCrNi RHEA. It is reproduced from [144] with permission of the publisher (Elsevier).

build a sample using the AM-SLM process. The random single-phase FCC structure is observed along with a dislocation network,  $\text{Mn}_2\text{O}_3$  nano-sized oxides, and epitaxial growth grains. The exceptional mechanical properties are obtained by a high dislocation density, fine grains, and precipitates at room and elevated temperatures. The slip and deformation twins ( $25^\circ\text{C}$  to  $600^\circ\text{C}$ ), slip and partial recrystallization ( $>700^\circ\text{C}$ ) are the major induced deformation mechanisms [139]. In the field of stress mechanics, the deformation mechanisms observed in HEAs, such as dislocation slip and twinning, are influenced by the grain orientation. At elevated temperatures, the plastic deformation of fine-grained HEAs is described by the grain boundary sliding mechanism

[140]. At intermediate temperatures, dislocation movements within the grains are hindered by the dynamic strain aging mechanism. The mechanical properties of HEAs are predominantly influenced by the deformation rate, which determines the high strain rate. Dislocation motion is more dominant at lower temperatures, while diffusion processes become more significant at elevated temperatures [141]. The planar dislocations, deformation twins, and stacking faults are attributed to the fatigue deformation mechanisms of HEAs. Planar dislocation slip improves deformation homogeneity by minimizing irreversibility. Additionally, the work-hardening ability is enhanced by deformation twins and stacking faults. Moreover, planar deformation improves the

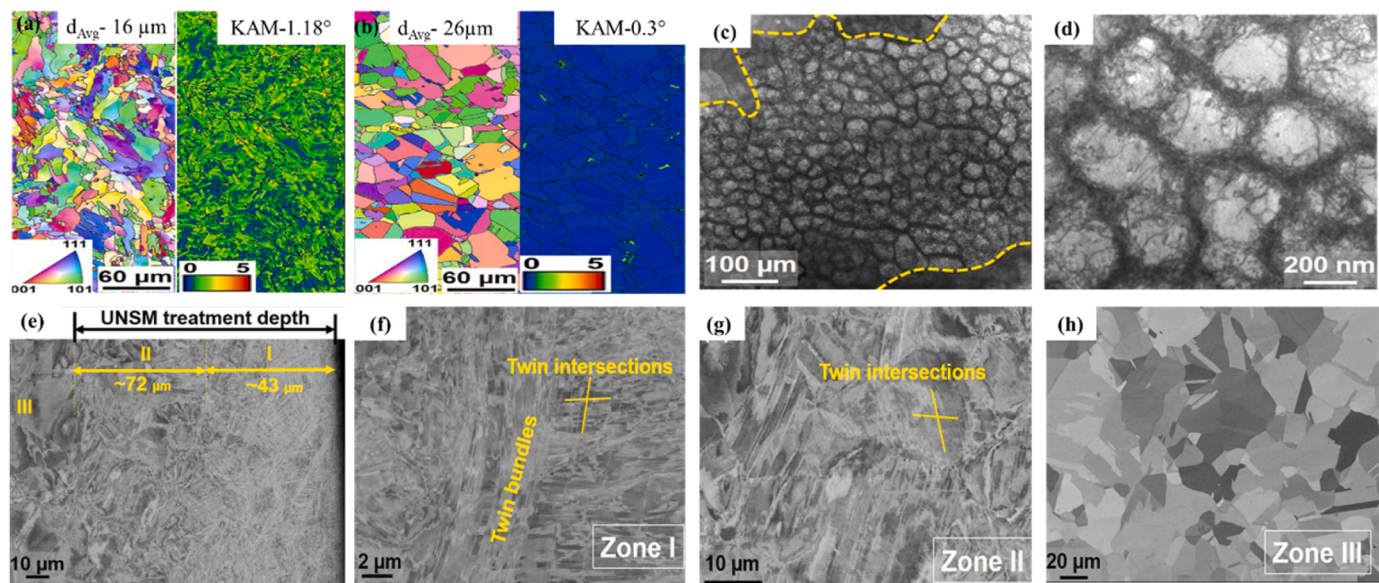


**Fig. 18.** Heterogeneous microstructures of (a) LPBF sample, (b) As-cast sample, (c) Fine cellular dislocation structure of LPBF sample, (d) Higher magnification of cellular dislocation structure, (e) UNSM treated region of LPBF sample, (f) Zone I, (g) Zone II, (h) Zone III of LPBF-printed CoCrFeMnNi sample. It was reproduced from [149] with permission of the publisher (Elsevier).

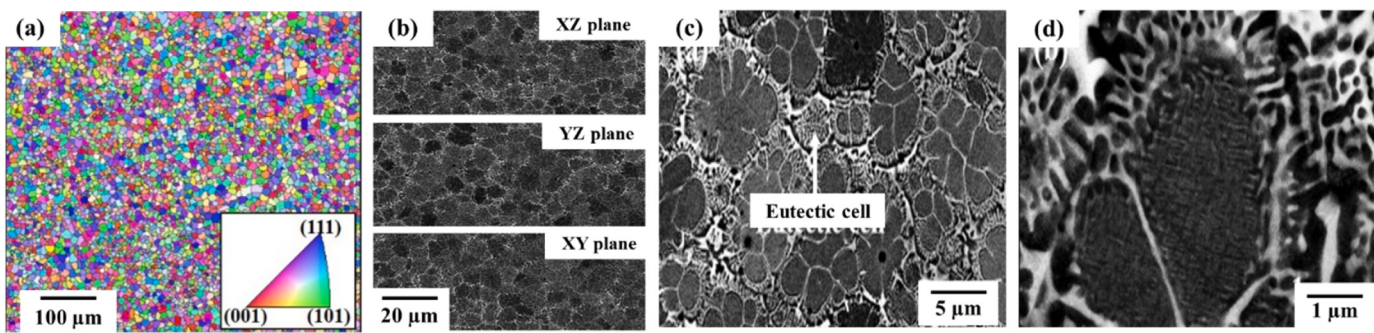


**Fig. 19.** (a) Equiaxed grains by EBSD evaluation, (b) Equiaxed grain microstructures in 3D space by BSE images of XZ, YZ, and XY plane, (c) Equiaxed grains and eutectic cell at grain boundary by intergranular bright phase, and (d) Corresponding high magnification eutectic structure clinging to pro-eutectic dendrites of AlCoCrFeNiTi<sub>0.5</sub> HEA by LENS. Reproduced from [83] with permission of the publisher (Elsevier).

fatigue resistance of HEAs [142]. The AM build samples exhibit the amorphous phase, which is characterized by excellent mechanical properties caused by dispersion hardening [143]. The FeCoCrNiMn HEA is fabricated using the AM-SLM technique to improve fracture strength by achieving high thermal stability of HEA and homogenous distribution of heared amorphous phase [106].

Selective Electron Beam Melting (SEBM) is effectively employed to build a WMoTaNbVFeCoCrNi RHEA by the mixture of pre-alloyed FeCoCrNi and WMoTaNb. The random orientation of refined dendritic structures is observed on the SEBM-printed samples by a higher collating rate (Fig. 17a). The solidified grains exhibit both grain boundary pores and interdendritic pores in different regions of dark contrast, attributed to the presence of lower melting point elements (Fig. 17b). The lower melting points and lack of melt flow on final solidification stage attribute solidification cracks (Fig. 17c). During solidification, inadequate feeding flow can cause the pores to expand into cracks at various grain orientations (Fig. 17d and e). A higher microhardness of 836±17 HV and compressive yield strength of 915±47 MPa are obtained by refined grain strengthening, elemental segregation, and induced multiple phases of 87% BCC, 13% FCC, and laves phases (Fig. 17f) [144]. The AM-SEBM process and solution treatment improve the tensile and corrosion resistance of gas-atomized Co1.5CrFeNi1.5Ti10.5Mo0.1 HEA. The excellent tensile strength > 900 MPa and ductility < 4% are obtained by SEBM. The excessive Ni3Ti intermetallic phase of the SEBM sample is observed to have minimized ductility. Moreover, a considerable synergistic improvement in tensile and corrosion resistance is observed through the subsequent process of solution treatment by homogeneous precipitation of refined grains [145]. A 70 μm size gas-atomized equimolar AlCoCrFeNi HEA is used to fabricate a sample by the AM-SEBM process. The mechanical and corrosion behaviors of SEBM samples are increased compared to the as-cast sample by the fine <100> structure of columnar grains in the building direction. The SEBM sample offers a 37% reduced corrosion pitting potential compared to the as-cast samples due to the refined microstructure [146]. The gas atomization and high-temperature remelting spheroidization method of Ni<sub>8</sub>Cr<sub>4</sub>Co<sub>4</sub>Fe<sub>6</sub>W<sub>2</sub> HEA is used to build a sample using the AM-SLM technique. The enhanced microhardness of 193 GPa is observed in the spheroidization SLM processed samples. The mechanical properties of yield strength, UTS, and elongation of spheroidization SLM processed samples increased by 33.7%, 25.9%, and 30.6% over the gas atomization SLM processed sample. The fabricated samples are potentially applicable to high-temperature environments such as aviation engine blades [147].

A significant dense structure of Fe<sub>30</sub>Mn<sub>50</sub>Co<sub>10</sub>Cr<sub>10</sub> and Fe<sub>50</sub>Mn<sub>30</sub>Co<sub>10</sub>Cr<sub>10</sub> HEAs is produced by Laser Powder Bed Fusion (LPBF) techniques with 105.82 J/mm<sup>3</sup> VED. A single-phase FCC and HCP, along with FCC phase structures, are observed in the Fe<sub>30</sub>Mn<sub>50</sub>Co<sub>10</sub>Cr<sub>10</sub> and Fe<sub>50</sub>Mn<sub>30</sub>Co<sub>10</sub>Cr<sub>10</sub> HEAs. A 580.65 MPa yield strength and 32.5% elongation are attained in FCC-structured Fe<sub>30</sub>Mn<sub>50</sub>Co<sub>10</sub>Cr<sub>10</sub> HEA, which is 16% and 10% higher than the dual phase of Fe<sub>50</sub>Mn<sub>30</sub>Co<sub>10</sub>Cr<sub>10</sub>

HEA [148]. A 10–55 μm spherical morphology of gas-atomized CoCr-FeMnNi HEA is used to build a sample by the LPBF process. The LPBF samples are processed by Ultrasonic Nanocrystal Surface Modification (UNSM) for gradient microstructures, which leads to gradient properties caused by heterodeformation-induced strengthening. The LPBF-built sample observes unique heterogeneous microstructures of 16 μm grain size with a higher Kernel Average Misorientation (KAM) of 1.18° than the as-cast sample, which shows equiaxed recrystallized grains of 26 μm (Fig. 18a and b). A fine cellular dislocation within the columnar grains LPBF-build sample is achieved by repeated reheating and melting process, as well as solidification conditions (Fig. 18c and d). A higher microhardness of 620 HV, yield stress of 665±10 MPa, UTS of 771 ±12 MPa, and reduced elongation of 25±6% by UNSM-treated LPBF samples through gradient microstructures zone. The microstructure zone exhibits a high density of twins, twin bundles (Zone I), twin intersections (Zone II), and unaffected (zone III), as shown in Fig. 18(e-h) [149]. A 45±15 μm size of gas-atomized Fe<sub>40</sub>Mn<sub>20</sub>Co<sub>20</sub>Cr<sub>15</sub>Si<sub>5</sub> HEA is used for the LPBF process. The as-build LPBF sample exhibits 71.9% HCP and 28.1% FCC phase structures. The printed LPBF sample offers a high strength of 530±40 MPa yield strength, 1.1 GPa UTS, and 30% ductility by high work hardenability, transformation, and twinning-induced plasticity. In addition, 0.1% of voids demonstrate a high strength-ductility [150]. The LPBF technique is employed on gas-atomized Al<sub>18</sub>Co<sub>30</sub>Cr<sub>10</sub>Fe<sub>10</sub>Ni<sub>32</sub> HEA to build a crack-free dense structure. The LPBF printed sample exhibits exceptional strength of 1.06 GPa yield strength and 1.37 GPa UTS, along with 21.3% elongation by combined coarse cellular, fine cellular, and lamellar eutectic structures of FCC and BCC phases. The excellent thermal gradient and epitaxial grain growth are developed by the continuous melting and solidification of layers during LPBF [151]. The AM-SLM technique is employed to produce a fine-grain structure of NbMoTaTiNi HEA. The hardness and mechanical properties are decreased with annealing as-cast HEA by 800, 1000, 1200, and 1300°C. A slight improvement is observed under the 600 °C annealed as-cast HEA sample. The fast-cooling rate of the SLM, rapid formation of equiaxed fine crystals, and brittle nature of Mo elements in the HEA system decline the properties of annealed samples [152]. The post-processing treatments, such as HIP and annealing, applied to AM-processed HEA samples result in improved mechanical properties and microstructural features. The printed HEA samples demonstrate refined grain structures and enhanced mechanical properties, indicating potential solidification-related densification. These findings contribute to the advancement of knowledge regarding AM-enabled HEA fabrication and highlight its possible applications in high-performance engineering components.

## 5.2. Directed energy deposition techniques

DED techniques significantly produce complex shapes in large-scale components. Each layer of components is built by a laser beam of the

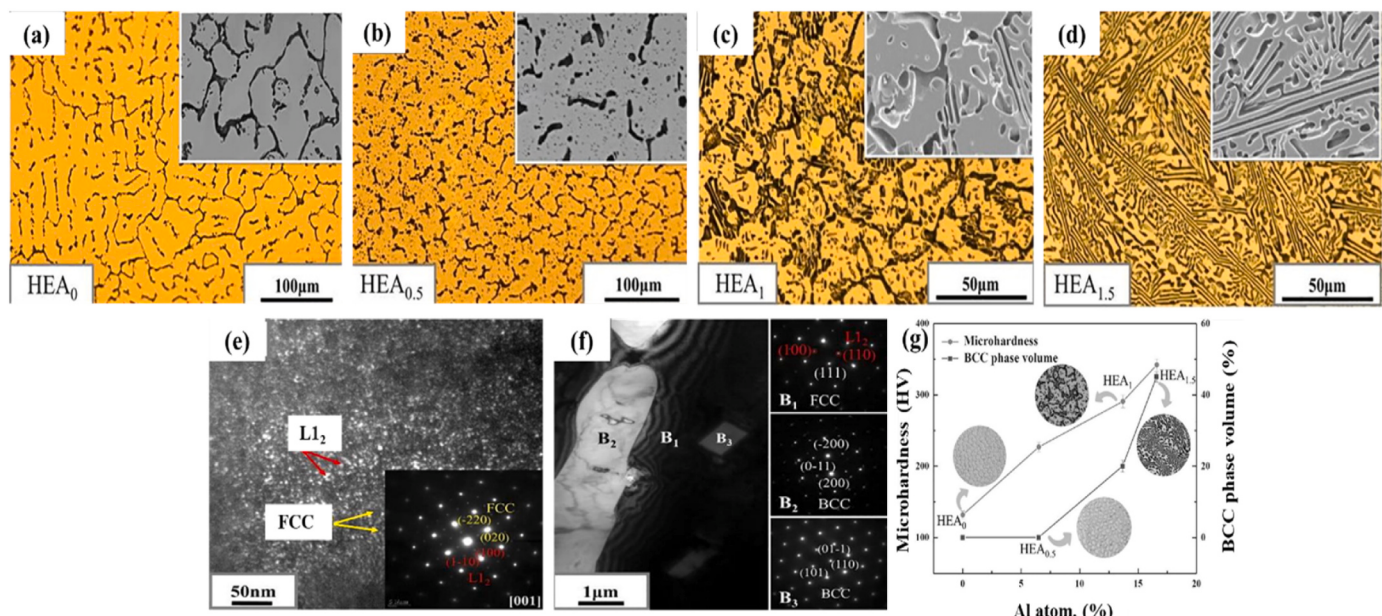


**Fig. 20.** (a) Dendritic microstructure of HEA<sub>0</sub>, (b) Dendritic microstructure with black contrast of HEA<sub>0.5</sub>, (c) Blocky phases B2 with irregular morphology of HEA<sub>1</sub>, (d) Lamellar microstructure C2 with all FCC/BCC eutectic structure of HEA<sub>1.5</sub>, (e) L1<sub>2</sub> crystal structure of HEA<sub>0.5</sub>, (f) B<sub>1</sub>, B<sub>2</sub>, and B<sub>3</sub> phases in the inter-dendritic areas of HEA<sub>1</sub>, and (g) Microhardness and BCC volume of DLD build (Al<sub>x</sub>CoCrFe)<sub>50</sub>Ni HEA. It is reproduced from [155] with permission of the publisher (Elsevier).

DED process, which creates a molten pool on the substrate. The layers are bonded with the previous layer in the molten pool by the powders that are poured coaxially with the laser beam. The enhanced mechanical properties are attained by reduced segregation and significant texture of DED techniques [153]. The AM-LENS technique is used to fabricate gas-atomized non-equiaxial AlCoCrFeNiTi0.5 HEA with an equalized grain structure (Fig. 19a). The further morphology, the XY, XZ, and YZ planes are investigated and show the fully equalized grains rather than columnar grains which is commonly exhibits on AM-built sample (Fig. 19b). The order BCC (B2) and disordered BCC (A2) phase structures are observed. The grains are equiaxed, which is described by intergranular discrete bright phases (Fig. 19c). The pro-eutectic dendrites cling to the rod morphologies, and the eutectic and pro-eutectic dendrites exhibit a single-grain structure (Fig. 19d) [83]. The non-equimolar Al0.3CoCrFeNi HEA is fabricated by the AM-LENS technique and followed by heat treatment to improve the yield strength. The intermetallic precipitates, formation of nanometer-scale clusters of Al-Ni-rich solute, and L1<sub>2</sub> precipitates contribute to the higher yield strength [82]. The AlCrFeMoV<sub>x</sub> ( $0 < x < 1$ ) HEA is used to fabricate a sample by the AM-LENS technique. A single solid structure of the BCC phase is observed in the processed sample. The existence of high solubility of the V element in the HEA system exhibits improved solid solution strengthening. By the addition of V elements (0.3–18.5 at%), the hardness is enhanced to 581 HV from 485 HV [84]. A 50–100  $\mu\text{m}$  size gas-atomized CoCrFeNiMn HEA is used to fabricate a sample by the LENS process. Subsequently, a heat treatment process is undergone at different temperatures of 673, 873, and 1073 K for 2 hrs under the Ar environment. The higher tensile properties of 725 MPa UTS and 510 MPa yield strength are obtained in 873 K due to the strain hardening ability, equiaxed columnar grains, and  $\sigma$  precipitates play a crucial role in deformation. The softening phenomenon by 1073 K leads to minimizing the yield strength, UTS, and improves the total elongation by 26% [81]. The LENS technique is used to fabricate equimolar ZrTiVCrFeNi HEA, and the prepared alloy exhibits excellent chemical homogeneity. A single-phase FCC structure with 4  $\mu\text{m}$  cellular microstructure and Mn-Ni-rich intercellular regions is obtained by a high cooling rate of the process. High corrosion resistance is observed due to the chemically homogeneous grains by annealing at 1100°C for 1 hr

[85]. The AM-processed Al0.78CoCrFeNi HEA displayed a uniform grain structure by various solid solutions and heat treatment processes. The sample exhibits an evenly distributed B2 phase structure at 1050 °C for 45 mins [154].

The gas atomized (Al<sub>x</sub>CoCrFe)<sub>50</sub>Ni ( $0 \leq x \leq 1.5$ ) HEA is employed to prepare the AM-DLD technique. The dendritic microstructure and black contrast are observed by the addition of Al content up to 7.5% (Fig. 20a and b). The interdendritic area exhibits an irregular morphology of blocky phases B2 at 12.5% of Al content (Fig. 20c). The eutectic structure of C<sub>2</sub> and FCC/BCC lamellar microstructure obtained when the Al content exceeds 12.5% (Fig. 20d). The addition of Al content, the FCC phase structure transforms into dual phase of FCC and BCC structure along with L1<sub>2</sub> precipitated nanophase of 5 nm (Fig. 20e and f). The enhanced microhardness of 342 HV is observed by precipitation and solid solution hardening due to an increment of Al content (Fig. 20g) [155]. A 50–110  $\mu\text{m}$  size of gas-atomized FeCoCrNiMn HEAs is used to fabricate DED samples to analyze the deformation and columnar to equiaxed transition. The microstructures exhibit equiaxed grains and columnar grains with low and high scanning speeds, respectively. The enhanced tensile properties of 330 MPa yield strength, 630 MPa UTS, and 55% elongation are observed in the DED build sample due to the high dislocation density and higher work hardening rate by equiaxed grains [156]. The plasma-rotating electrode processed Ni<sub>2.1</sub>CoCrFeNb<sub>0.2</sub> HEA employs the AM-DLD process to produce the defect-free sample. An 1127 MPa tensile strength and 17% elongation are exhibited in the DLD build samples due to the formation of  $\gamma'$  phase nano-scaled precipitation by heat treatment [78]. The AM-DLD process is used to construct a sample with the CoCrNiFeNb<sub>x</sub> HEA. The rapid solidification of the DLD process is attributed to uniform microstructure. The equiaxed structures are obtained from columnar structures by the addition of the Nb element in the HEA system. The exceptional strengthening properties and printability are obtained by the effect of precipitation strengthening [105]. A single-phase FCC structured CoCrFeNi HEA is fabricated by AM-LMD process by varying laser power of 1000, 1300, and 1600 W. The improved microhardness of 190.95 HV is observed in the CoCrFeNi HEA at 1300 W laser power. The optimum mechanical properties of 312.11 MPa yield strength, 574.25 MPa tensile strength, and 41.5% elongation are attained by a 1300 laser power HEAs [157].

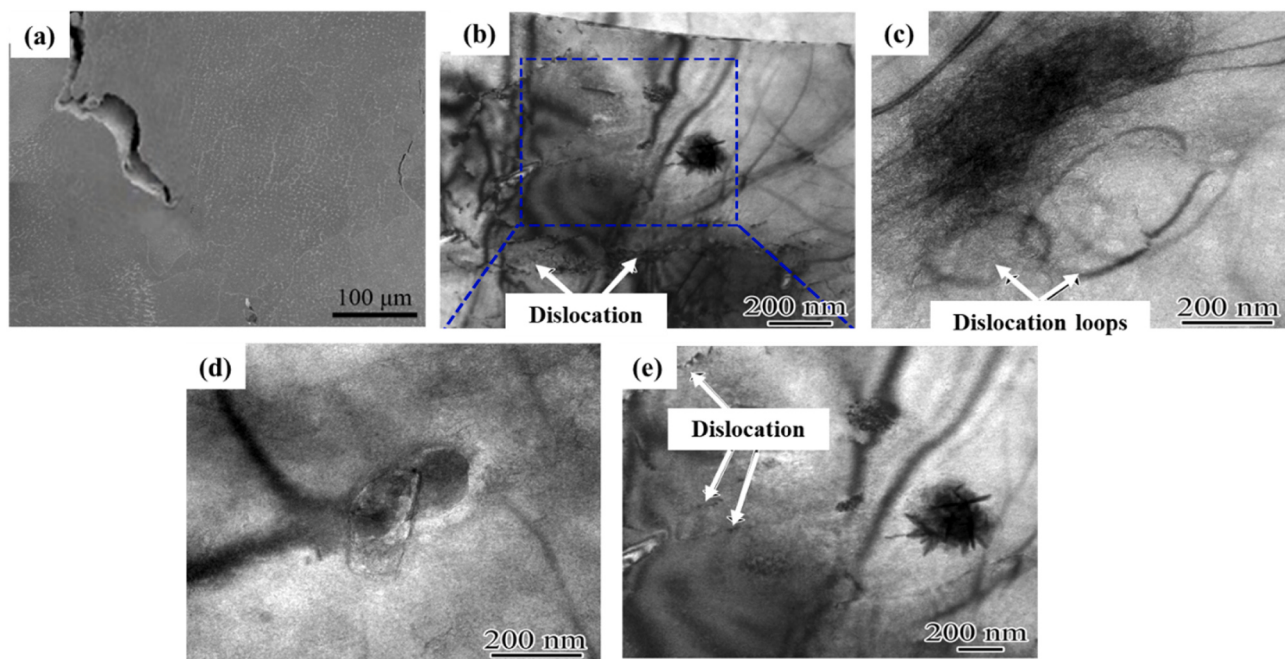


**Fig. 21.** (a) Crack formation, TEM image of (b) Dislocation, (c) Dislocation loops, (d) Precipitation particles, (e) High magnification of LMD processed  $\text{Al}_{0.3}\text{CoCrFeNi}$  HEA, reproduced from [79] with permission of the publisher (Elsevier).

The gas-atomized CoCrFeNiMn HEA is employed to fabricate the Laser Aided Additive Manufacturing (LAAM) sample. The AM-processed sample exhibits dendritic columnar grains of 3–4  $\mu\text{m}$  size. The grain boundary strengthening of fine grain structures exhibits excellent tensile properties of 518 MPa yield strength and 660 MPa UTS. The strengthening properties are improved by steady strain hardening behavior due to the formation of deformation twins at low temperatures (-130°C) [158]. The gas-atomized non-equimolar  $\text{Al}_x\text{CoCrFeNi}$  ( $x=0.3, 0.6$ , and 0.85) HEA is used to build a sample by direct laser fabrication. The different phase structures of FCC ( $x=0.3$ ), dual phases of B2 and BCC ( $x=0.85$ ), and mixtures of three phases ( $x=0.6$ ) are observed by XRD evaluation. The exceptional yield strength of 1400 MPa is obtained by the further addition of Al element in HEA ( $x=0.85$ ) due to the existence of the B2 phase along with the BCC structure [159]. The equiatomic TiZrNbHfTa RHEA is used to build a sample using the AM-LMD technique. The columnar specimen exhibits a high hardness of 509 HV due to the equiaxed uniform grain size of a single-phase BCC structure [160]. The AM-LMD process is used to build a sample of gas-atomized  $\text{Al}_{0.3}\text{CoCrFeNi}$  HEA with a strong  $<110>$  texture. The cracks are formed in between the phase boundary of FCC and B2 structures, which results in minimum tensile properties (Fig. 21a). The grain interior of the build sample exhibits precipitation particles and dislocation loops, as shown in the TEM image due to the ordered and disordered transformation thermal stress (Fig. 21b). The distribution high-density dislocation and precipitated particle are confirmed in the magnified pictures (Fig. 21c and d). Fig. 21e shows the precipitation clusters and dislocation observed on the further magnified image of Fig. 21b. The enhanced wear resistance and microhardness are obtained by precipitate B2 and  $\sigma$  phases and  $\text{L}1_2$  phase formation, which is induced due to the annealing at 650 °C for 5 hrs. However, insufficient shear stress induces for plastic deformation due to the dislocation recovery during annealing [79]. The excellent strength and ductility are obtained due to the partially and fully recrystallized region by a high strain hardenability of heterostructure CoCrFeMnNi HEA by the LMD process [161].

Cold Spray Additive Manufacturing (CSAM) is one of the deposition techniques used to attain a near-net shape and improve properties. The CSAM process is effectively used to prepare a CoCrFeMnNi HEA sample. The vertical and horizontal building direction of the CSAM processed

sample exhibits a yield strength, ultimate compressive strength, and strain deformation of 1036.6 MPa, 1117.8 MPa, 10.1%, and 1033.1 MPa, 1102 MPa, 5.6% respectively [162]. Various AM techniques, including LENS, DLD, and LAAM, have been successfully employed to fabricate HEAs with tailored microstructures and improved mechanical properties. These techniques have been particularly effective in producing equiaxed grain structures in non-equiatomic HEAs, resulting in enhanced yield strength and hardness. Furthermore, heat treatment has been found to further enhance the mechanical properties by promoting the formation of intermetallic precipitates and nanoscale clusters. These advanced manufacturing techniques offer promising avenues for the development of HEAs with superior mechanical performance, catering to various applications. Fig. 22 shows the effect of AM process parameters on the mechanical properties of HEAs.

### 5.3. Comparison of AM with conventionally manufactured HEAs

AM-processed samples exhibit exceptional mechanical properties, wear resistance, and corrosion behavior, making them suitable for high-performance applications. These improved properties are achieved by enhancing the microstructure, forming stable phases, achieving high relative density, and minimizing porosity. The optimization of process parameters enables the generation of a sufficient melt pool and fluidity of HEA powders, which effectively fills the pores and microcracks in the built sample, resulting in increased densification. The rapid heating and cooling rates inherent in the AM process contribute to the exceptional properties exhibited by AM-manufactured HEAs, surpassing those achieved through conventional manufacturing methods [57]. The mechanical properties of SLM-processed FeCoCrNi HEA are compared with the conventional manufacturing process of arc melting. The SLM-built sample produces a 600 MPa yield strength, 745 MPa UTS, and 238 microhardness, which is 68.6%, 38.6%, and 50.4% higher than the traditional arc melting process. The fine grains of the built sample, fast solidification rate, and higher temperature gradients are the responsible features for enhanced material properties [163]. The optimized process parameters of 1200 mm/s scan speed and 400 W laser power of SLM processed C addition of FeCoCrNi HEA samples exhibit a higher yield and UTS by a refined grain size of 40–50  $\mu\text{m}$  and solid-solution

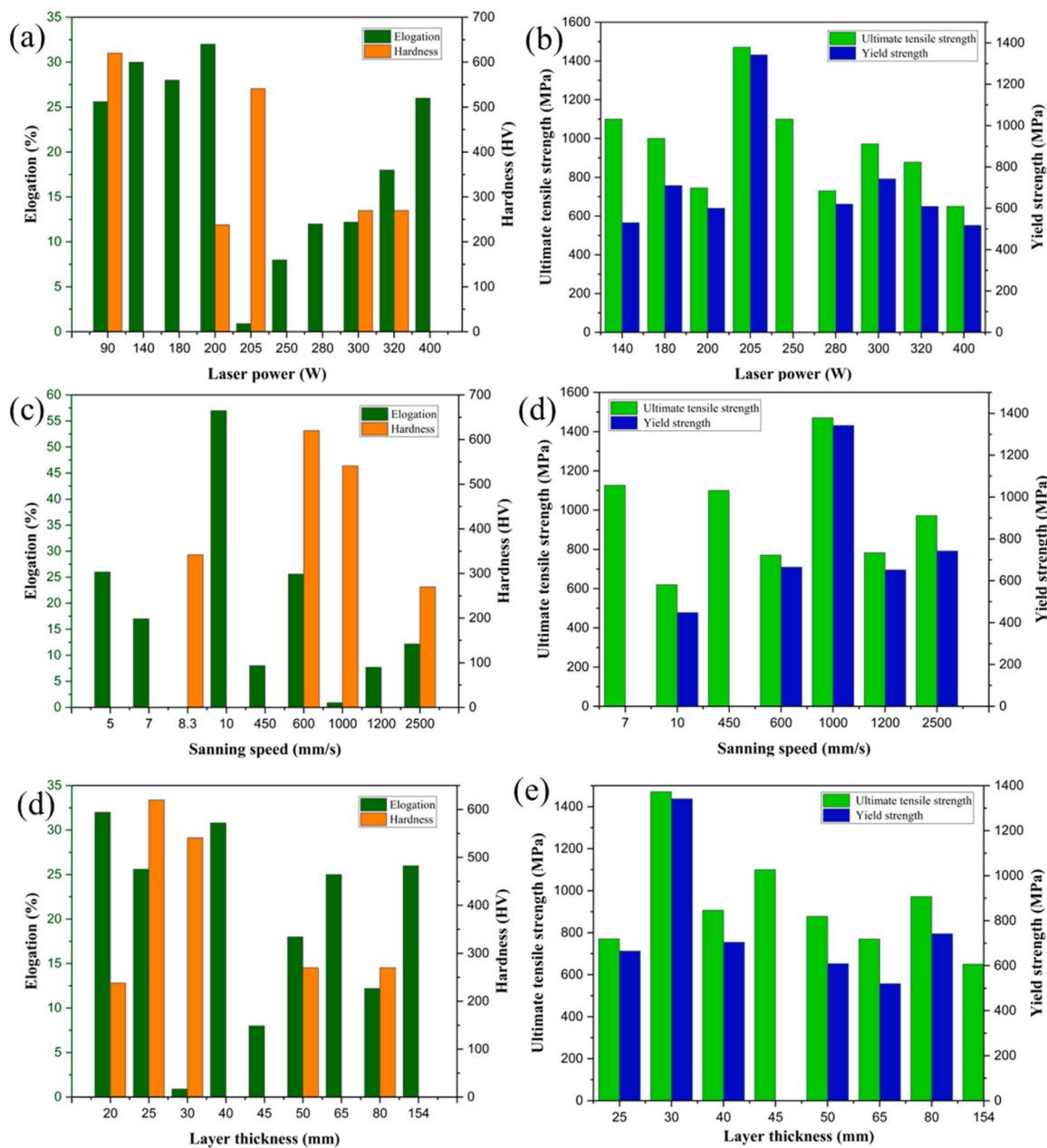


**Fig. 22.** Effect of the AM process parameters on mechanical parameters (a, b). Laser power, (c, d). Scanning speed, (e, f). Layer thickness.

strengthening [164]. A higher microhardness and yield strength are attained in the AM-LMD CoCrFeMnNi HEA samples than in the conventional casting method. The LMD technique is characterized by significant crystallographic textures and high cooling rates, which contribute to the improved strength of the built samples. The minimized Schmid factor resulting from the crystallographic textures requires stress to initiate dislocation motion, thereby enhancing the strength of the material. Additionally, the rapid heating and cooling rates associated with the LMD process lead to much higher yield strength compared to conventional manufacturing methods [165].

The AM-DED technique is utilized to build AlCoCrFeNi HEA samples, aiming to improve their mechanical properties through enhanced microstructure and phase composition compared to the as-cast method. Factors such as the equiaxed dendritic structure in the building direction, the presence of duplex BCC phase, specific crystallographic orientation, and excellent strong texture contribute to the enhancement of material properties. The presence of fine-grain dendrites and

interdendritic regions in the built samples results in a compressive strength of  $2976 \pm 96$  MPa and a strain of  $45.9 \pm 4.8\%$ . These values are 34.5% and 23% higher, respectively, than those achieved through conventional manufacturing methods [166]. The AM-LENS technology is used to build a thin-walled AlCoCrFeNi HEA with a different scanning rate. A dendritic microstructure of grains  $30.6 \pm 9.2$  mm in size is achieved with the addition of a scan rate of 40 mm/s. A higher microhardness of 543 HV is attained in the LENS sample, which is 13% higher than that of the as-cast sample. A fine grain structure and maximum cooling rate are the responsible factors for improving microhardness [167]. SEBM prepares the equiatomic AlCoCrFeNi HEA samples for structural applications. The microstructure and FCC phase precipitation, B2/BCC mixture phases of the AM build samples produce a maximum compressive strength of  $1668 \pm 72$  MPa (Fig. 23a). A higher plastic deformability is exhibited in the SEBM fabricated samples without any deviation of strength [168]. Direct Laser Fabrication (DLF) techniques of the AM process are employed to produce  $\text{Al}_x\text{CoCrFeNi}$  ( $X = 0.3, 0.6, 0.85$ )

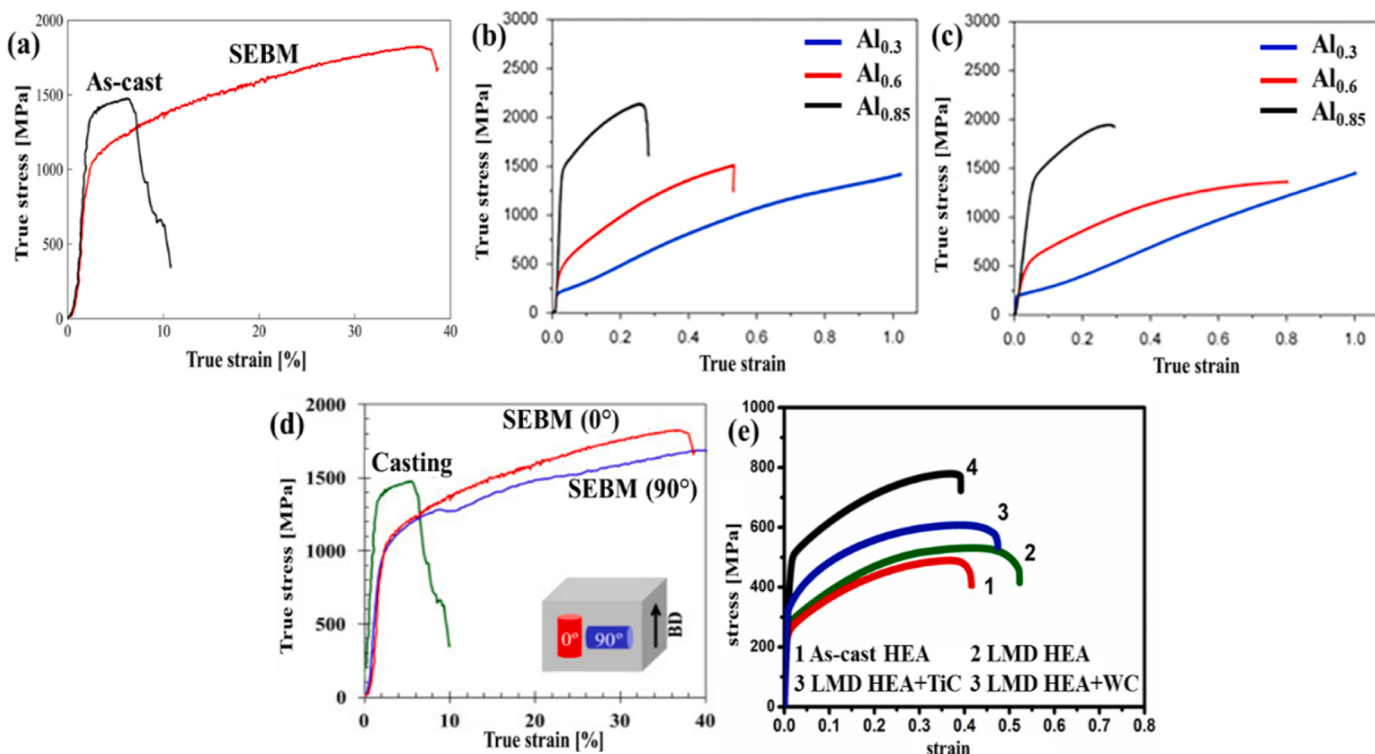


**Fig. 23.** Tensile strength of (a) SEBM-  $\text{Al}_{0.85}\text{CoCrFeNi}$  HEA.

(a) Reproduced from [168], (b) DLF-  $\text{Al}_x\text{CoCrFeNi}$ . (b) Reproduced from [169], (d) SEBM -  $\text{Al}_{0.85}\text{CoCrFeNi}$  HEA. (c) It is reproduced from [104] with permission of the publisher (Elsevier). (d) Reproduced from [169], (e) As-cast-  $\text{Al}_{0.85}\text{CoCrFeNi}$ . (e) Reproduced from [170], (e) LMD -  $\text{CoCrFeMnNi}$  HEA.

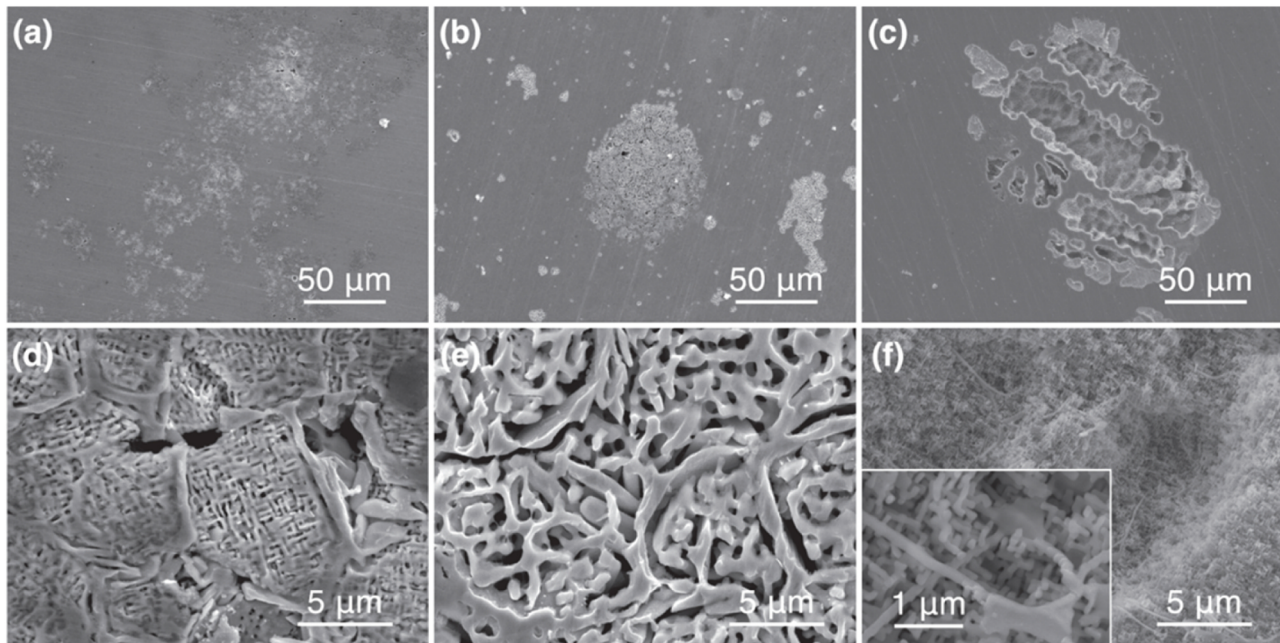


**Fig. 24.** (a) Top part of EBM processed sample, (b) Bottom part of EBM processed sample, (c) As-cast sample, (d-f) Corresponding magnified view. It is reproduced from [173] with permission of the publisher (Springer Nature).

HEA sample. The mechanical properties are improved with the increment of Al element in the HEA system by forming BCC structure from FCC, FCC+BCC phase on 0.85, 0.3, and 0.6 M addition of Al. Chemical homogeneity is produced by arc-melting by repeating remelting. A rapid prototyping DLF produces enhanced strength compared to conventional arc melting through the improved microstructure. Fig. 23b and c

demonstrate the tensile properties of the DLF sample and the as-cast method [169].

The AM-SEBM process is employed to build the  $\text{Al}_{0.85}\text{CoCrFeNi}$  HEA sample to produce higher mechanical properties than the as-cast method. A 1015 MPa yield strength and 1668.3 MPa fracture strength are made by SEBM (0°), which is higher than the SEBM (90°) and

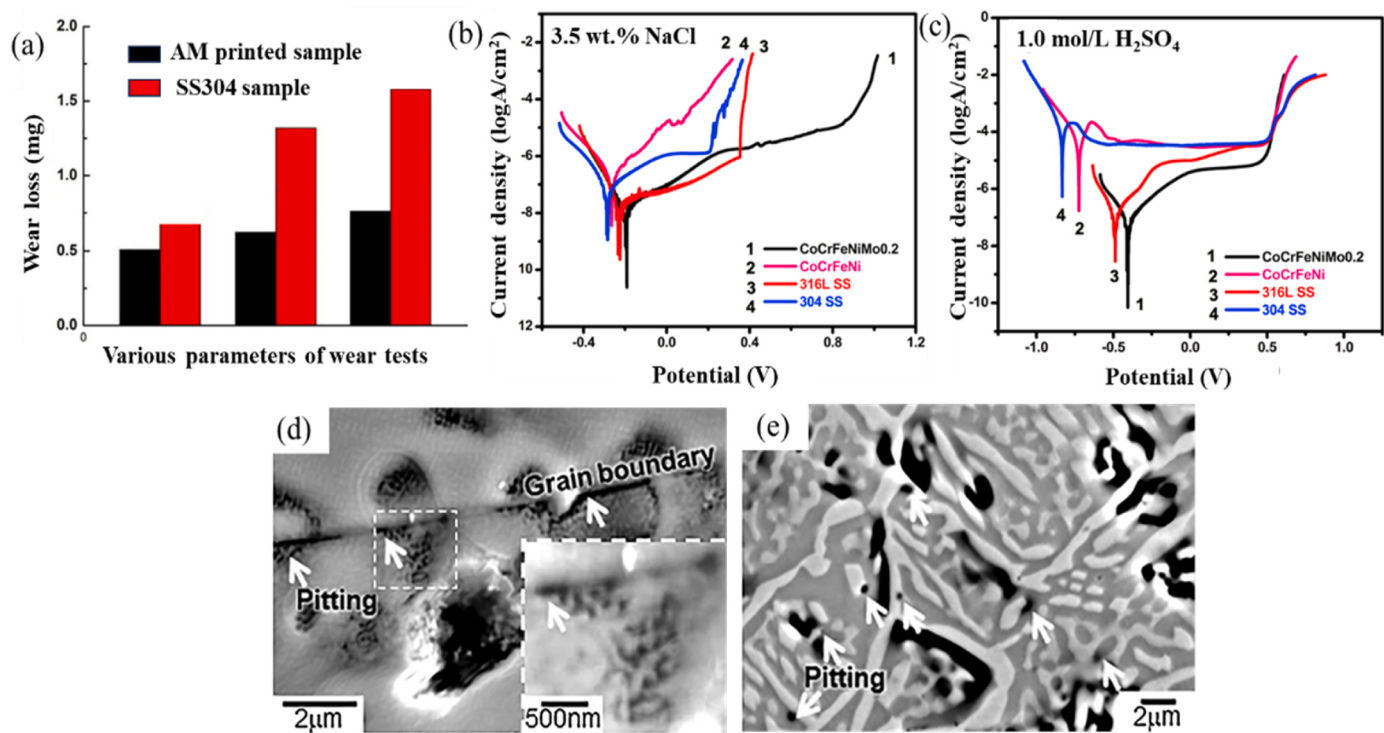


**Fig. 25.** (a) Wear loss of AM printed and unprinted SS304 samples.

(a) Reproduced from [174], (b) Corrosion behavior under NaCl atmosphere. (b) Reproduced from [175], (d) Corroded surface of SEBM printed sample. (c) It is reproduced from [146] with permission of the publisher (Elsevier). (d) Reproduced from [175], (c) Corrosion behavior under  $H_2SO_4$  atmosphere. (e) Reproduced from [146], (e) Corroded surface of as-cast sample.

traditional casting method (Fig. 23d). The SEBM exhibits an intergranular fracture surface, whereas cleavage fracture obtains on the as-cast method sample [170]. The LMD technique is used to fabricate CoCr-FeMnNi HEA with the addition of TiC and WC particles. The synergistic effect of grain refinement and precipitation reinforcement of the AM build sample produces a tensile strength of 550 MPa to 610 MPa and 776 MPa (Fig. 23e). The even distribution of WC particles,  $M_{23}C_6$  precipitation, and single deformation pattern leads to higher tensile strength [104]. The LMD process is employed to produce CrMnFeCoNi HEA samples with different process parameters. The enhanced UTS of 878 MPa, yield strength of 402 MPa, and 95% plastic strain are obtained in the LMD sample with 1400 W laser power. The columnar grains and equiaxed grains, heat flux direction, and solidification mode of LMD samples lead to improved mechanical properties [171].

The AM-LMD process is employed to fabricate AlCoCrCuFeNi HEA under varying laser power and scanning speed. A higher hardness and improved wear resistance are observed in the LMD fabricated samples than in the traditional arc melting process. The AM process parameters of 1600 W laser power, 12 mm/s scanning speed, and rapid solidification are attributed to enhanced properties [172]. The AM-EBM process is used to manufacture equimolar AlCoCrFeNi HEA. The EBM processed sample exhibits a better corrosion behavior than the as-cast sample under 3.5 wt% NaCl. The stability of passive film improves by the enrichment of Cr in the B2 phase. Large corrosion pits are observed on the as-cast samples than the top and bottom parts of EBM samples (Fig. 24). The bottom part of the EBM processed sample exhibits a 30% higher fraction of FCC phase than the top part of the EBM sample [173]. A 20–60  $\mu m$  size spherical-shaped AlCrFeCoNi HEA is printed onto SS304 using 80 KJ power, 1200 mm/s printing speed, and 80  $\mu m$  scanning track width under the Ar atmosphere. The reduced wear loss is observed in the HEA printed sample than the SS304 sample at the same process parameters (Fig. 25a). The improved hardness of 578 HV, single phase BCC structure, wear resistance HEA elements, high-temperature stability and oxidation properties of printed samples lead to higher

wear resistance [174].

The 80  $\mu m$  sized spherical shaped CoCrFeNiMo<sub>0.2</sub> HEAs are prepared by nitrogen gas atomization. The AM-LMD technique is effectively used to deposit as a successive layer over the SS316L substrate under different laser power. The larger crystal-size columnar grains are obtained by minimizing the temperature gradient by increasing the laser power. The improved corrosion resistance is observed over the SS304 and SS316L under 3.5 wt% NaCl and 1.0 mol/L  $H_2SO_4$  (Fig. 25b and c). The formation of a passive layer against the pitting leads to higher corrosion resistance [175]. The AM-SEBM technique is employed to fabricate an equimolar AlCoCrFeNi HEA. The corrosion behavior of SEBM and as-cast AlCoCrFeNi HEAs are evaluated under the sea water. The SEBM-processed HEA produces a lower pitting potential of 0.112 V vs. Ag/AgCl than the as-cast HEA of 0.178 V vs. Ag/AgCl. The small pits are observed in the interfacial regions of the SEBM sample, which are indicated in the white arrow mark (Fig. 25d). The as-cast sample exhibits a large pit around the grain boundaries (Fig. 25e) [146]. The AM techniques have demonstrated significant improvements in the mechanical properties, wear resistance, and corrosion behavior of HEA samples compared to conventional manufacturing methods. These improvements are attributed to optimized process parameters that lead to enhanced microstructure, formation of stable phases, higher relative density, and minimized porosity. Specifically, AM-produced HEA samples exhibit superior mechanical properties, including higher yield strength, UTS, and microhardness. These improvements can be attributed to factors such as a fine grain structure, rapid solidification rates, and specific crystallographic orientations. Moreover, the AM-processed HEAs showcase superior performance compared to conventional manufacturing methods, marking a significant advancement in materials engineering. Table 4 presents the mechanical properties of various AM-processed HEAs, along with the corresponding process parameters, induced phase structures, and the methods used for their synthesis.

**Table 4**

Properties of different AM-built HEA samples.

HEAs Elements	Synthesis of HEAs	AM	AM process parameters	Phase	Properties	Features	Ref.
AlCoCrCuFeNi	Gas atomization	SLM	Laser power – 160–400 W Scan speed – 400–1600 mm/s	FCC & BCC	Nanohardness – 756.16 HV Microhardness – 710.4 HV Elastic modulus – 200.28 GPa	A fine grain structure and high dislocation density induced by a rapid cooling rate	[67]
CoCrCuFeNiAl	Powder metallurgy	LENS	-	B2 & BCC	-	The order B2 and disordered BCC structure observe a dendritic grain structure.	[176]
AlCoCrFeNiCu & AlCoCrFeNiTi	-	LDT	Laser power – 1200–1600 W Scan speed - 8–12 mm/s	FCC & BCC	Corrosion rate - 0.00409 mm/year	Refined grains improve corrosion resistance by high scan speed and cooling rate of LDT (Laser Deposition Technique).	[177]
FeCoCrNi	Gas atomization	SLM	Laser power - 200 W Laser spot size - 50 µm Layer thickness- 20 & 50 µm	FCC	Microhardness - 238 HV UTS - 745 MPa Yield strength - 600 MPa Elongation - 32%	Enhanced strength and ductility are obtained, which are comparable to those of stainless steel.	[163]
CoCrFeMnNi	Gas atomization	SLM	Laser power - 400 W Scan speed – 800–4000 mm/s Laser beam dia. - 90 µm Layer thickness - 30 µm	FCC	UTS-649 MPa Yield strength - 445 MPa Elongation - 18%	High densification is obtained by improved laser energy density. Hot isostatic pressing is employed to enhance the strength.	[138]
CoCrFeNiMn	Gas atomization	SLM	Laser power – 160–290 W Scan speed – 1500–2500 mm/s Hatching space - 50 µm Laser beam diameter - 75 µm Layer thickness - 40 µm	FCC	Yield strength - 513 MPa	The SLM-built sample exhibits high strength and ductility by cellular structures.	[178]
SiFeCoCrNi	3D Mixer	SLM	Laser power - 113 & 197 W, Hatch spacing - 41 & 97 µm Layer thickness - 40 µm,	FCC	Tensile strength - 907±25 MPa Yield strength - 701 ±14 MPa Elongation - 30.8 ±2%	The sample exhibits numerous sub-grains of columnar grains without segregation. A novel dislocation loop and solid solution strengthening lead to high strength and ductility.	[87]
AlCoCuFeNi	Gas atomization	SLM	Laser power - 205 W Scan speed - 1000 mm/s Hatching space - 40 µm Layer thickness - 30 µm	FCC & BCC	Microhardness - 541 HV Tensile strength - 1471 MPa Yield strength - 1342 MPa Elongation - 0.9%	Rapid solidification of the SLM process and sluggish diffusion of HEAs lead to homogenous chemical distribution.	[179]
CoCrFeNiTi	Gas atomization	SLM	Laser power - 60–270 W Scan speed - 540–1350 mm/s Hatching space – 80–120 µm Layer thickness - 40 µm	FCC	UTS - 1178 MPa Yield strength - 773 ±4.2 MPa Elongation - 25.8 ±0.6% Corrosion pitting potential - 0.88 ±0.03 V	The enhanced mechanical properties are obtained by water quenching. The solution treatments depend on fine-ordered particles.	[101]
FeCoCrNiC <sub>0.05</sub>	Gas atomization	SLM	Laser power - 200–400 W Scan speed - 800–2000 mm/s Hatching space - 110 µm Layer thickness - 50 µm	FCC	Microhardness - 541 HV UTS – 797 MPa Yield strength – 656 MPa Elongation - 13.5%	The density and refined grains are obtained by the effect of high power and minimized scanning speed.	[164]
CoCrFeMnNi	In-situ alloyed	SLM	Laser power - 280 W Scan speed - 800 mm/s Hatching space - 60 µm Layer thickness - 30 µm	FCC	Tensile strength – 730 MPa Yield strength – 620 MPa Elongation - 12%	The strength of AM-processed samples improved by the Orowan strengthening. The voids are generated due to hindering the plastic deformation by sub-micron oxide particles	[180]
(CoCrFeMnNi) <sub>99</sub> C <sub>1</sub>	Gas atomization	SLM	Laser power - 280 W Scan speed -	FCC	UTS – 989 MPa Yield strength –	The solid solution, grain refinement, dislocation density, and nano-precipitation	[181]

(continued on next page)

**Table 4 (continued)**

HEAs Elements	Synthesis of HEAs	AM	AM process parameters	Phase	Properties	Features	Ref.
CoCrFeNiMn	Gas atomization	SLM	200–600 mm/s Hatching space - 80 µm Layer thickness - 25 µm Laser power - 250 W Scan speed - 450 mm/s Hatching space - 75 µm Layer thickness - 45 µm	FCC	829 MPa Elongation - 24.3%	lead to improved tensile properties. The addition of C elements ascribes substantial effect.	[62]
CrMnFeCoNi	-	LPBF	Laser power - 200 W Hatch spacing - 85 µm Exposure time - 80 µs Layer height - 50 µm Laser spot size - 65 µm	-	UTS - 770±10 MPa Yield strength - 520 ±10 MPa Elongation - 25%	The addition of TiN <sub>p</sub> leads to nucleation sites that improve the equalized ultrarefined grains of 2 µm. The enhanced strength and wear resistance are obtained by the effect of the Hall-Petch law due to the equiaxed HEA grains and nano-TiN <sub>p</sub> reinforcements. Dislocation slip and pores lack of fusions are the main sources of fatigue crack and cyclic plasticity.	[182]
Al <sub>0.5</sub> CoCrFeNi	-	SLM	Laser power - 320 W Scan speed - 800 mm/s Hatching space - 60 µm Layer thickness - 50 µm	FCC & BCC	Hardness - 270 HV Tensile strength - 878 MPa Yield strength - 609 MPa Elongation - 18% Relative density - 99.92%	The SLM process obtains improved mechanical properties through a fine cellular-dendritic structure without any intermetallic compounds.	[120]
Ni <sub>6</sub> Cr <sub>4</sub> WFe <sub>9</sub> Ti	Gas atomization	SLM	Laser power - 300 W Scan speed - 2500 mm/s Hatching space - 80 µm	FCC	Hardness- 270 HV Fracture strength - 970 MPa UTS - 972 MPa Yield strength - 742 MPa Elongation - 12.2%	The strength and ductility of SLM-processed samples are improved by the refined grains	[92]
Fe <sub>49.5</sub> Mn <sub>30</sub> Co <sub>10</sub> Cr <sub>10</sub> C <sub>0.5</sub>	Gas atomization	SLM	Laser power - 180 W Scan speed - 1000 mm/s Hatching space - 55 µm Layer thickness - 40 µm	FCC	UTS - 1 GPa Yield strength - 710 MPa Elongation - 28%	Strength-ductility of the SLM processed sample is improved by hierarchical microstructure and activation of multiple deformation mechanisms. (Dislocation slip, deformation twinning, and phase transformation)	[183]
CoCrFeMnNi	-	DLD	Laser power - 300 W Scan speed - 600 mm/min Laser beam dis. - 2 mm	BCC & FCC	UTS - 620 MPa Yield strength - 448 MPa Elongation - 57%	The exceptional tensile and ductility obtained by equiaxed- columnar transition structure.	[184]
Fe <sub>38.5</sub> Mn <sub>20</sub> Co <sub>20</sub> Cr <sub>15</sub> Si <sub>5</sub> Cu <sub>1.5</sub>	-	LPBF	Laser power - 110–200 W Scan speed - 250–1000 mm/s Hatching space - 100–120 µm Layer thickness - 30–40 µm	FCC	UTS - 1235 MPa Yield strength - 665 MPa Elongation - 17%	High strength and ductility are obtained and used for damage-tolerant structural materials. Passivation exhibited enhanced corrosion resistance.	[185]
CrMnFeCoNi	Plasma rotating electrode process	LENS	Laser power - 400 W Scan speed - 5 mm/s Hatching space - 460 µm Layer thickness - 154 µm	FCC	UTS - 650 MPa Yield strength - 517 MPa Elongation - 26% Relative density - 99.67%	Dislocation activities and deformation twinning accompany the tensile behavior of samples. The LENS-processed HEA sample demonstrates high-performance engineering applications.	[186]
CoCrFeNiMn	Gas atomization	DLD	Laser power - 880 W, Laser beam size - 2.5 mm, Scan speed - 10 mm/s, Powder feeding rate - 8.6 g/min.	-	UTS - 850±2 MPa Yield strength - 710 ±4 MPa Elongation - 40.2 ±1%	A 3–4 µm fine equiaxed grains of dendritic columnar leads to excellent tensile strength and ductility. LAAM techniques are used to fabricate large and complex parts.	[158]
CoCrFeMnNi	Gas atomization	LPBF	Laser power - 90 W Scan speed - 600 mm/s Hatching space - 80 µm Layer thickness - 25 µm	FCC	Microhardness - 620 HV, UTS - 771±12 MPa Yield strength - 665 ±10 MPa Elongation - 25 ±6%	The gradient microstructures obtained by UNSM enhance the hardness and tensile properties through the high density of twins, twin bundles, and twin intersections.	[149]
Fe <sub>40</sub> Mn <sub>20</sub> Co <sub>20</sub> Cr <sub>15</sub> Si <sub>5</sub>	Gas atomization	LPBF	Laser power - 140 W Scan speed - 800 mm/s Hatching space - 100 µm	HCP & FCC	UTS - 1.1 GPa Yield strength - 530 ±40 MPa Ductility - 30%	A high work hardenability, transformation, and twinning-induced plasticity leads to higher strength and ductility.	[150]

(continued on next page)

**Table 4 (continued)**

HEAs Elements	Synthesis of HEAs	AM	AM process parameters	Phase	Properties	Features	Ref.
Al <sub>18</sub> Co <sub>30</sub> Cr <sub>10</sub> Fe <sub>10</sub> Ni <sub>32</sub>	Gas atomization	LPBF	Layer thickness - 40 µm Laser power - 140 W Scan speed - 800 mm/s Hatching space - 100 µm Layer thickness - 40 µm	FCC & BCC	UTS - 1.37 GPa Yield strength - 1.06 GPa Elongation - 21.3%	The LPBF printed samples exhibit a crack-free dense structure. The excellent thermal gradient observed by continuous melting and solidification	[151]
(Al <sub>x</sub> CoCrFe) <sub>50</sub> Ni	Gas atomization	DED	Laser power - 1500 W Scan speed - 500 mm/min Laser beam dia. - 4–6 mm Layer thickness - 40 µm	FCC & L <sub>1</sub> / <sub>2</sub> /BCC	Microhardness - 342 HV	The solid solution and precipitation hardening are attributed to higher microhardness. 12.5% Eutectic precipitations were observed exceeding 12.5% of Al content.	[155]
FeCoCrNiMn	Gas atomization	DED	Laser power - 200–400 W Scan speed - 3–5 mm/s Powder feeding rate - 5.7–6.8 g/min Laser energy density - 66.7–80 J/mm	FCC	Yield strength - 330 MPa UTS - 630 MPa Elongation 55%	A higher work hardening rate and dislocation density obtain improved tensile properties. The varying scanning speed influences the grains.	[156]
Ni <sub>2.1</sub> CoCrFeNb <sub>0.2</sub>	Plasma-rotating electrode process	DED	Laser power - 1600 W Scan speed - 7 mm/s Laser spot dia. - 3 mm	FCC & Laves phase	Tensile strength - 1127 MPa Elongation - 17%	A defect-free samples are produced with high tensile strength by heat treatment.	[78]
CoCrNiFeNb <sub>x</sub>	-	DED	Laser power - 1600–1650 W Scan speed - 7 mm/s Laser spot dia. - 3 mm	FCC	Elongation 92.5%	High elongation and excellent printability obtained by the effect of precipitation strengthening	[105]

## 6. Potential applications of AM-processed HEAs

### 6.1. Medical applications

The Micro-plasma arc AM process is effectively used to fabricate samples of ball-milled 45–105 µm TiTaNbMoZr HEA powders on Ti6Al4V base substrate for knee implant applications. The biocompatibility evaluation of AM-processed samples underwent analysis of the cell viability, released metallic ions, and corrosion behavior. The major BCC fine dendritic structure and minor BCC inter-dendritic structures appeared on microscopy evaluation of the AM-processed HEA sample (Fig. 26a). The major and minor BCC phases are observed in the AM processed sample (Fig. 26b). The rapid heating and cooling lead to protecting BCC phases from decompositions and hampering the formation of intermetallic compounds. A significant AM parameter is used to fabricate a sample effectively in the size of 10 deposition layers with 3 tracks of 43×35 mm (Fig. 26c). A considerable corrosion resistance is exhibited on AM samples due to the formation of a stable passive layer by the existence of Zr, Nb, and Ta elements (Fig. 26d) [187]. Gas atomization pre-alloyed Ti<sub>1.4</sub>Nb<sub>0.6</sub>Ta<sub>0.6</sub>Zr<sub>1.4</sub>Mo<sub>0.6</sub> Bio-HEA is used for biomedical applications through the AM-SLM process. A high cooling rate of 10<sup>7</sup> K/s is employed for SLM to hinder elemental segregation and shape customization. The SLM built a densely packed sample of high yield stress, better biocompatibility, and reduced porosity [188]. The LPBF process is effectively used to produce a TiFeCrCoNi HEA with a higher hardness of 776.3 HV, which is 2.8 times higher than Ti. The higher hardness, grain refinement, and strengthening effect attributes enhanced wear resistance. The improved properties of the AM process samples are potentially applicable in dental and orthopedic surgery [189].

The spherical morphology of gas-atomized Ti<sub>1.5</sub>NbTa<sub>0.5</sub>ZrMo<sub>0.5</sub> HEA is used to build a sample of exceptional mechanical and biocompatibility by the AM-SLM process. The SLM-built sample attributes an excellent compressive property and upholds high strength at room temperature

due to the refined grains (Fig. 27a). The evenly distributed equalized grains of mean 5.416 µm lead to higher mechanical properties (Fig. 27b). The excellent grain refinement and impediment of element segregation by SLM process ascribes a dense structure. The Triply Periodic Minimal Surface (TPMS) lattice is fabricated with three different surfaces, which leads to a very close Young's modulus of human trabecular bone (Fig. 27c). The developed structures meet the current scenario in bone implant application by customized shape with high density [190]. The Gyroid (G) unit is used to construct the TPMS lattice and unit cell controlled by Schoen's gyroid mathematical Eq. (12).

$$\begin{aligned} \phi_G(x, y, z) = & \cos(\omega x)\sin(\omega x) + \cos(\omega y)\sin(\omega y) + \cos(\omega z)\sin(\omega z) \\ = & C \end{aligned} \quad (12)$$

where  $\phi_G(x, y, z)$  – Gyroid equation, x, y, and z - spatial coordinates, and C is a constant. The C value is used to control the surface area and shape of the TPMS lattice [190,191].

A Plasma rotating electrode processed Ti-25 Nb-3Zr-3Mo-2Sn HEA is used for medical implants through the AM-LENS techniques by 0.2–0.25 mm layer thickness. The anisotropic microstructure formed due to the solidification conditions of LENS by 10–20 µm precipitate-free bands. The radially aligned bands are attributing a high density of α phase precipitates, which is an interconnected unusual ring structure. The excellent adhesion properties are exhibited on HEA with human bone marrow-derived mesenchymal stem cells [192]. The SLM and in-situ alloying are fabricating Cu powder with gas-atomized CoCrFeNi powder. The synthesized quasi-equiaxial CoCrFeCuNi HEA powder exhibits excellent mechanical and antibacterial ability. The SLM-built HEA shows evenly distributed Cu elements with FCC phase structure. The biofilm formation by gram-negative Escherichia coli and gram-positive Staphylococcus aureus is prevented by Cu addition, which improves the antibacterial ability [193].

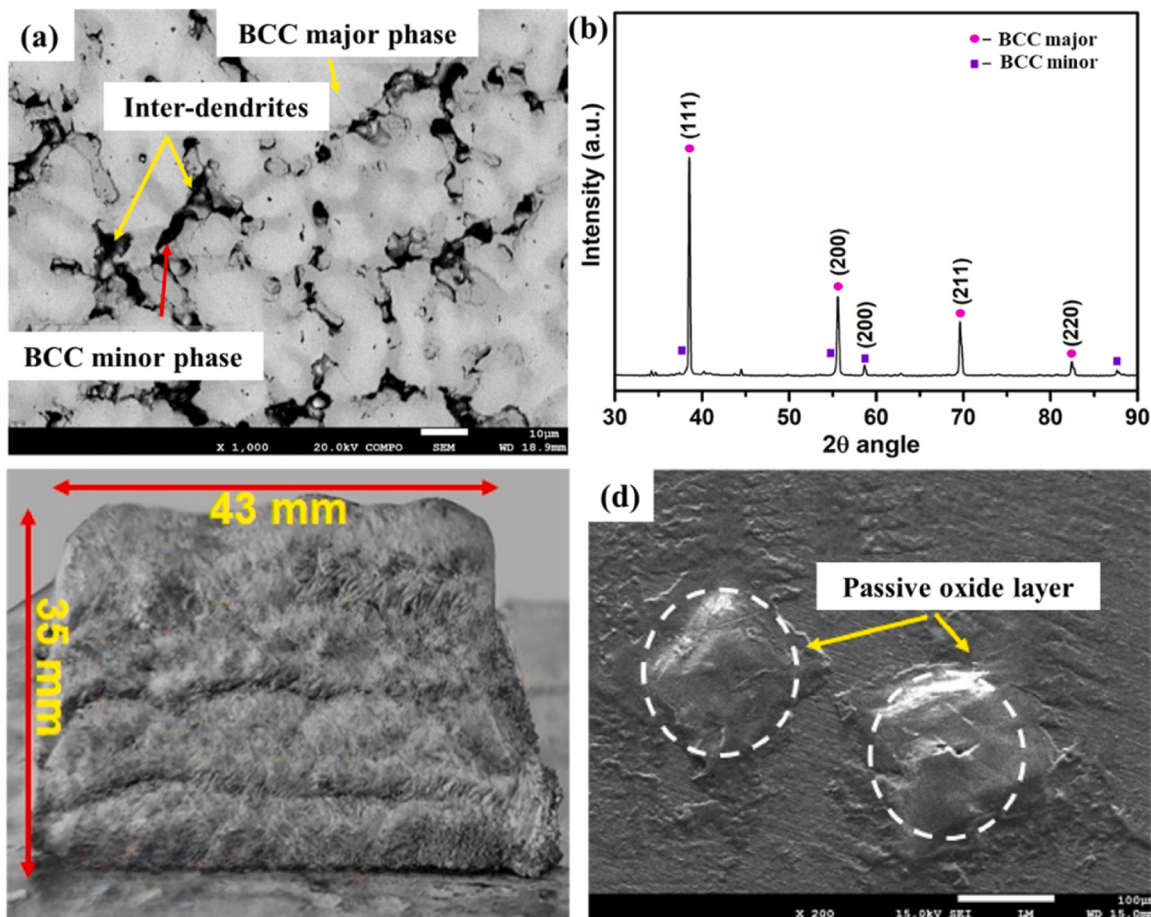


**Fig. 26.** (a) Microstructural view, (b) Phase evaluation, (c) Multi-layer build sample, (d) Formation passive layer of Micro-plasma arc AM processed TiTaNbMoZr HEA, reproduced from [187] with permission of the publisher (Elsevier).

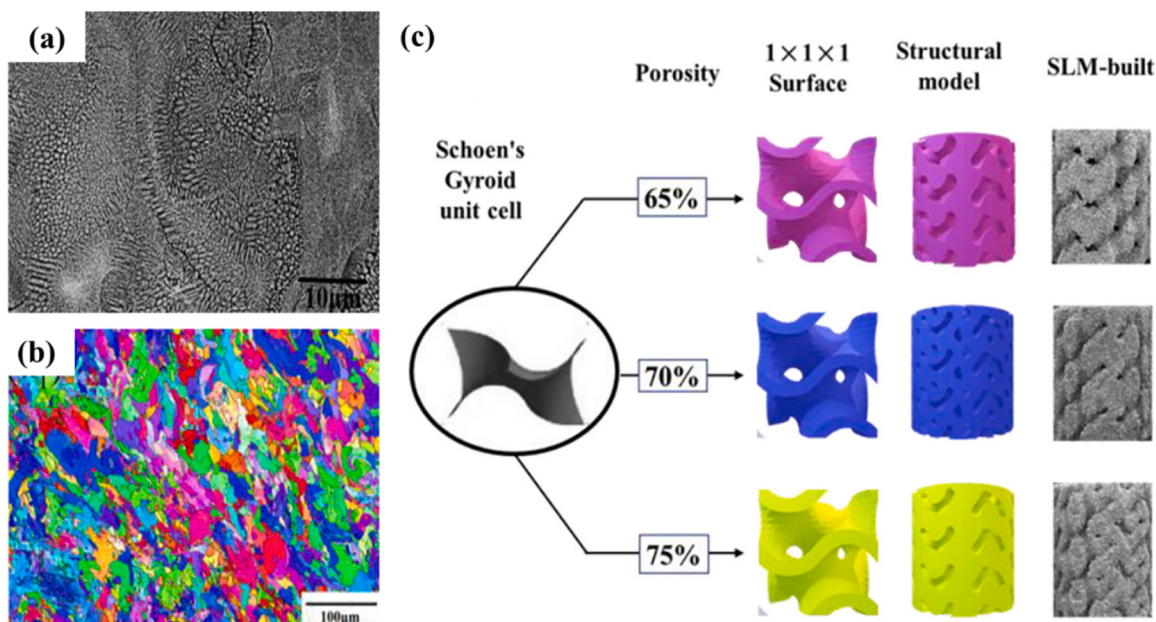


**Fig. 27.** (a) Microstructure of XY plane by BSE image, (b) Grain size of XY plane by IPF, (c) TPMS models with different densities of SLM build  $Ti_{1.5}NbTa_{0.5}ZrMo_{0.5}$  HEA. It is reproduced from [190] with permission of the publisher (Elsevier).

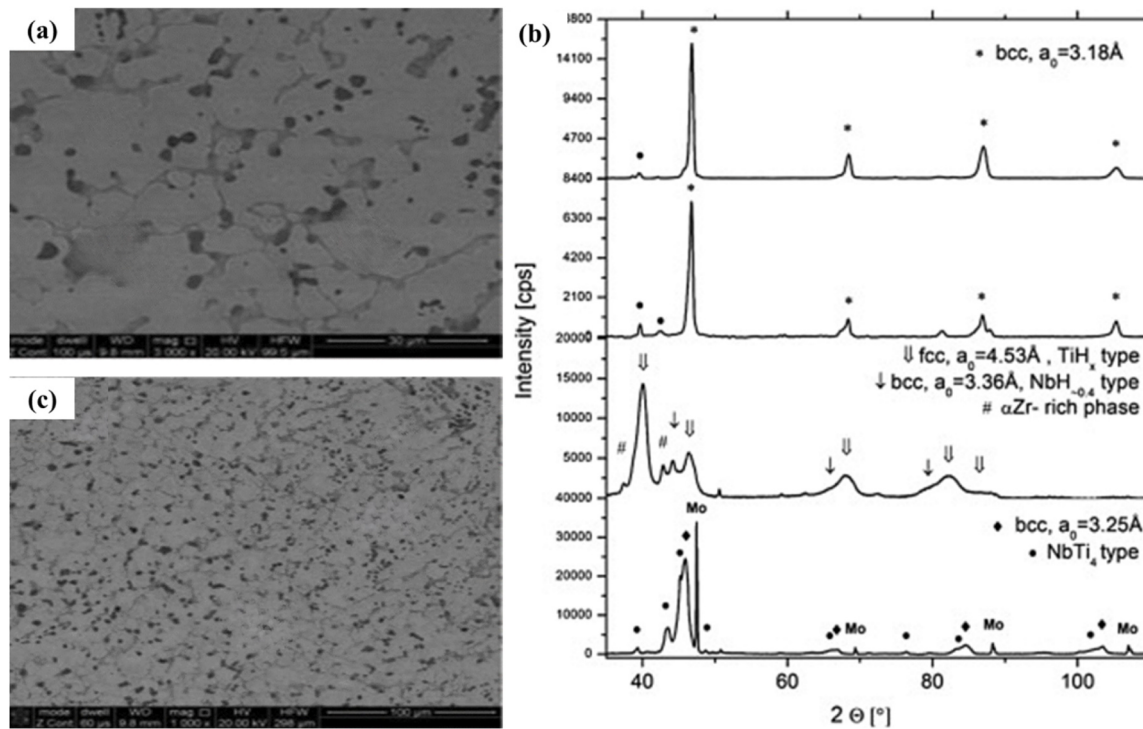


**Fig. 28.** (a) Microstructure of 1000 W laser power with threefold remelting LENS of TiZrNbMoV HEA, (b) Phase evaluation by XRD pattern, (c) Microstructure of 1000 W laser power with threefold remelting after LENS and hydrogenation of TiZrNbMoV HEA. It is reproduced from [97] with permission of the publisher (Elsevier).

## 6.2. Hydrogen storage applications

In renewable energy sources, hydrogen plays a crucial role in potential replacements for fossil fuels by their production, profusion, and

storage devices. The fast kinetics, reversible phase transformation for hydrogenation-dehydrogenation reactions, exceptional hydrogen storage capacity, and their activation of HEAs properties contribute a potential material for hydrogen containers [194]. A gas-atomized

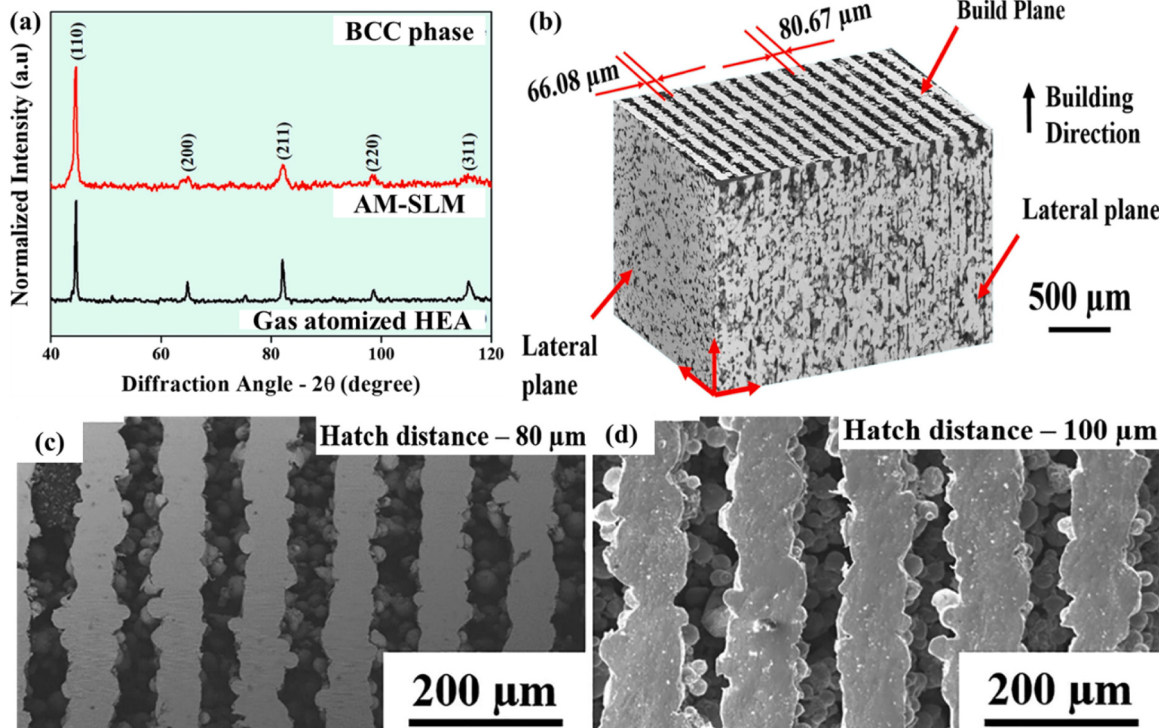


**Fig. 29.** (a) Phase evaluation of gas atomized HEA and as-printed SLM sample, (b) 3D SEM images, (c) SEM image of 80  $\mu\text{m}$  hatch distance, (d) SEM image of 100  $\mu\text{m}$  hatch distance of SLM build AlCoCrFeNi HEA. It is reproduced from [202] with permission of the publisher (Elsevier).

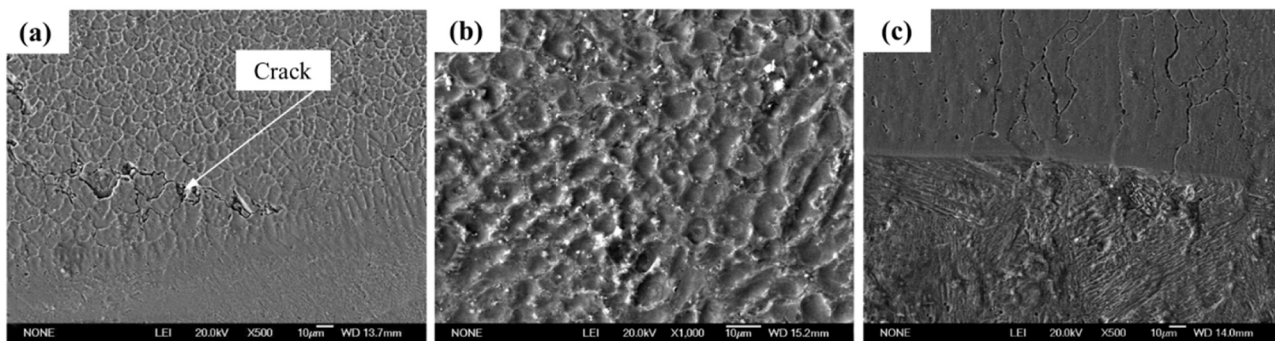


**Fig. 30.** (a) Crack formation of  $\text{Al}_2\text{CrFeCo}_0\text{CuNiTi}$ , (b) Cladding zone of  $\text{Al}_2\text{CrFeCo}_{1.5}\text{CuNiTi}$  HEAs, (c) Bonding zone of  $\text{Al}_2\text{CrFeCo}_2\text{CuNiTi}$  HEAs. It is reproduced from [209] with permission of the publisher (Elsevier).

TiZrNbMoV HEA powders are blended by AM-LENS technique with 300 W and 1 kW laser powers. The BCC phase and two-phase dendritic structure with some Mo particles are exhibited under the 300 W laser power. The dendritic structures disappeared gradually with the equimolar ratio of 3.18 Å lattice parameter (Fig. 28a). The BCC structure obtains 1 kW power at three times remelting, which is advantageous for hydrogen storages (Fig. 28b). Fig. 28c shows the SEM image of TiZrNbMoV HEA after hydrogenation at 1 KW power. A 0.59 and 0.61 wt% of hydrogen capacities are obtained by LENS and additional heat treatment, respectively. A triple remelting process with a stable bcc phase leads with no structural changes; hence, the synthesized HEA is favorable for hydrogen storage [97]. The AM-LENS process for hydrogen storage fabricates a pre-alloyed LaNiFeVMn HEA. The two primary phase structures of  $\sigma + \text{La}(\text{Ni}, \text{Mn})_5$  and FCC +  $\text{La}(\text{Ni}, \text{Mn})_5$  are observed. The capacity of hydrogen storage is proportional to the lanthanum atomic content, which is present in the observed phase structures. There is no relationship between the compositions of phase and pressure observed during the formation of the hydride phase [195].

The equimolar pre-alloyed ZrTiVCrFeNi HEA powder is synthesized using the AM-LENS technique. The HEAs are annealed at 1000°C to obtain an evenly dispersed chemical composition after synthesis. The major C14 Laves phase and few  $\alpha$ -Ti solid solutions are observed. A 1.81 and 1.56 wt% of hydrogen capacity are obtained on synthesis and annealed HEAs [86]. In addition, the electrochemical properties of admirable dielectric constant and excellent Li conductivity in HEAs served as battery electrodes and capacitors [196]. The physical and chemical properties, along with exceptional mechanical properties by the tailoring principle of HEA, are effectively applicable for conversion and energy storage [197]. The reversibility of hydrogen desorption is essential for practical applications.

### 6.3. Aerospace applications

AM-processed HEAs offer enormous applications in aerospace sectors due to their excellent strength, corrosion, and wear resistance, hardness, fatigue, and lightweight elements [198]. The synthesis of lightweight HEAs with single-phase structures is a crucial process due to the non-miscible nature of Al, Ti, Mg, and Be with transition elements like Cr, Fe, and Cu [199]. A 120  $\mu\text{m}$  size gas-atomized CrMnFeCoNi HEA powders are processed by the AM-LMD technique. The LMD-processed HEAs exhibit both columnar grains and equiaxed grains. These proportions are controlled by varying laser power due to the columnar to equiaxed transitions through heat flux direction and the solidification mode of LMD. A vane compressor prototype model is built with more flexibility of LMD and higher mechanical properties than the as-cast at cryogenic temperatures [171]. The AM process is employed to fabricate aviation turbine blades by LMD on FeCoCrAlCu HEA with SiB<sub>2</sub> and Yttria Partially Stabilized ZrO<sub>2</sub> (YPSZ)-HEA composites. A fine and free form of micro crack is exhibited on LMD samples by the effect of YPSZ

and ultrafine nanocrystals. The excellent wear behavior is obtained on the HEA composites rather than the FeCoCrAlCu LMD-HEA [200]. AM-processed laser techniques are effectively used to fabricate high-integrity aerospace components such as valve trains, exhaust nozzles, combustion chambers, compressor blades, and aero-engine gas turbines [201].

### 6.4. Nuclear applications

In nuclear sectors, various factors, including diffusion rate, recovery, thermal expansion, dislocation climb, phase transformation, vacancy concentration, creep, recrystallization, precipitation, and oxidation, are taken into account, particularly at elevated temperatures. Conventional alloys designed for nuclear reactor materials typically employ strategies such as microstructure modification through precipitation, heat treatments, solute atoms, and cold working to achieve the desired properties. However, in the present scenario, HEAs are being utilized to meet the requirements in nuclear applications [20]. The gas-atomized spherical morphology of the mean AM-SLM process fabricates 44  $\mu\text{m}$  equimolar AlCoCrFeNi HEA with a single-phase BCC structure (Fig. 29a). The SLM process is effectively used to produce a controllable gap size of mean  $67 \pm 1 \text{ mm}$  in layered microstructure (linear patterns). The processed sample exhibits a defined porous (gap) between the two melt hatches (Fig. 29b). The width and gap of the melt pool are controlled by the process parameters, VED, hatch overlaps, and hatch distance (Fig. 29c, d). The SLM-produced materials with a definable gap are more suitable for next-generation filters in extreme environments, including nuclear and oxidation [202]. The low activation energy, excellent creep, corrosion, and oxidation resistance of HEAs are effectively employed in thermonuclear reactors [203]. The 2 AM processes of SLM and EBM are effectively employed to fabricate SS316L ITER panel parts for nuclear applications. SLM obtains a smooth surface with better accuracy than the EBM with a one-step building process. The austenite phase sample leads to sufficient magnetic permeability properties. SLM obtains a fine regular element with sub-grains while EBM produces irregular grains of larger sub-grains [204]. The HEAs (CrMoNbTiV and Ti<sub>2</sub>ZrHfV<sub>0.5</sub>Mn<sub>0.2</sub>) are prime candidates for nuclear application, which are effectively produced by the AM process [205,206].

### 6.5. Coating applications

The parts of high-temperature jet propulsion and gas turbine usage are extended by coating through the AM process for some more years. The formation of a coating layer serves as a protective layer for high-temperature applications [207]. The excellent interfacial and bonding properties of HEAs are effectively used for coating base metal. The MoFe<sub>1.5</sub>CrTiWAlNb<sub>x</sub> ( $x=1.5, 2, 2.5$  and 3) HEA is designed for the coating of M<sub>2</sub> tool steel by AM-laser cladding. The microhardness and wear behavior of coated samples are improved by the addition of Nb



**Fig. 31.**  $\text{Al}_x\text{CrFe}_2\text{Ni}_2$  HEA - Centrifugal pump impeller for structural components.

content in HEA elements and formed BCC, (Nb, Ti)C, and C14-Laves phase structures. The coating exhibits fine grain structures that are obtained by the rapid heating and cooling of laser cladding. The fast-cooling behavior of the AM process inhibits grain growth. The cellular crystal structure transforms into columnar crystal, which leads to 910 HV microhardness and abrasive wear mechanism [208]. The AM-laser deposition process for structural applications improves the surface properties of aerospace components. The Cu and Ti-based HEAs ( $\text{AlCoCrFeNiCu}$  and  $\text{AlTiCrFeCoNi}$ ) serve as a coating material to enhance the surface properties of A301 steel. The process parameters are optimized for defect-free structures and homogeneous coating.

The coated samples achieved enhanced hardness by a high scan speed of 12 mm/s, leading to rapid solidification that improves grain refinement [126]. A 50  $\mu\text{m}$  spherical morphology of  $\text{Al}_2\text{CrFeCo}_x\text{CuNiTi}$  HEA powders is coated on Q235 steel by the AM-laser cladding process to enhance the surface and corrosion resistance. The equiaxed grains are evenly distributed on the coated surfaces, which are composed of columnar and equiaxed grains. The cracks appeared on the cladding surface due to the induced residual stress by rapid heating and cooling (Fig. 30a). The addition of 2% Si particles leads to the elimination of cracks by reducing internal stress. Fig. 30b shows the better bonding of HEA with Q235 steel with the absence of crack propagation. The columnar grains are formed near the bonding zone, and the segregation and grain growth are repressed (Fig. 30c). The corrosion behavior of coated surfaces is improved by equiaxed columnar grains and crack-free surfaces. The addition of Co content increases the corrosion rate by the formation of the intermetallic phase and coarse grain nature [209].

#### 6.6. Automotive applications

The low density and lightweight properties of HEAs, combined with their superior heat transfer capabilities, enable the reduction of engine weight, making them highly suitable for utilization in the automotive industry [28]. The feasible complex designs by the AM processes and the energy storage capacity of HEAs extended their application in electric vehicles [196]. The tunability, immense chemical space, excellent stability of metastable HEAs used in catalytic activities, and flexible design by the AM process lead to progressions in actuator prototypes [210]. The solid solution strengthening mechanism leads to high strength, creep resistance, and tribological behavior of HEAs, which is potentially applicable in various sectors like sports equipment, electronic equipment, and automobiles [92]. A lightweight design structure of the AM-processed HEA products extends the cruising range of electric vehicles. The shape-memory features of  $\text{TiZrHfNiCoCu}$  HEAs are used to fabricate a prototype of automotive actuators [211]. The LPBF plays a vital role in producing customized metallic parts that are extensively used in automotive, biomedical, and aerospace industries under a high

cooling rate of nearly  $10^6$  K/s [212]. The application of the AM-processed HEAs is not limited to the conclusion of the above-described applications. The utilization of the AM process is discovered in many engineering industries. A novel  $\text{Al}_x\text{CrFe}_2\text{Ni}_2$  HEA is used to produce a centrifugal pump impeller for structural components via Oerlikon AM using 3D printing (Fig. 31). The developed material serves as an alternative to super duplex stainless steels, offering comparable strength and corrosion resistance properties.

The utilization of AM techniques has demonstrated significant potential across various sectors, including medical, hydrogen storage, aerospace, nuclear, coating, and automotive applications. These techniques enable the fabrication of complex structures with tailored properties, providing exceptional mechanical strength, corrosion resistance, and biocompatibility. This versatility is crucial for applications ranging from knee implants in the medical field to aerospace components. HEAs, in particular, have shown promise in hydrogen storage applications due to their ability to facilitate fast kinetics and reversible phase transformations, making them potential replacements for fossil fuels. Furthermore, their ability to withstand extreme environments, such as those found in the aerospace and nuclear sectors, highlights their suitability for critical applications. The development of HEA coatings through AM processes has also been significant, as it enhances surface properties and extends the lifespan of components in high-temperature and corrosive environments. In the automotive sector, the lightweight nature and tunability of HEAs, coupled with the flexibility of AM processes, offer opportunities for innovation in electric vehicles, catalytic activities, and actuator prototypes. These advancements contribute to the progress of various engineering industries. Overall, the utilization of AM techniques with HEAs has opened up new avenues for advancements in multiple sectors, revolutionizing the way complex components are manufactured and providing improved performance and efficiency in a wide range of applications. The applications and properties of various AM-processed HEA samples, along with induced phases and synthesis of HEAs, are tabulated in Table 5.

#### 7. Obstacles and prospects

Despite the excellent results achieved by HEA in AM, there are still several challenges that need further attention in future research to address these gaps. Additionally, the synergistic effect of HEAs in AM-processed products is extensively covered in various fields, including medical, storage systems, transportation, aerospace, nuclear, and automotive industries. However, it is essential to summarize some of the challenges encountered during the process critically. These challenges are outlined below.

- The better flowability of HEAs powder obtains enhanced homogeneous distribution and packing density of AM-processed samples. Hence, the contributed HEAs should be spherical or near to spherical morphology that improves the AM build samples through the feedstock of powders.
- Despite as-printed multiphase HEAs have outstanding characteristics at ambient temperature, their mechanical qualities at higher temperatures are rarely described. HEAs, like Ni-based superalloys, exhibit intermediate-temperature embrittling ( $\sim 650\text{--}900$  °C). This type of behavior may also occur in as-printed HEAs, and addressing this critical issue ought to serve as among the primary goals of future study.
- The microstructure and phase stability of as-printed HEAs are critical factors in defining their working temperature range and engineering reliability. At room temperature, the inclusion of high-density dislocation networks is thought to improve the characteristics of the as-printed materials. However, understanding how these microstructures evolve at high temperatures is critical. Furthermore, the effect of these dislocation structures on resistance to high-temperature creep and oxidation needs to be further investigated.

**Table 5**

Applications and properties of fabricated HEA samples by the different AM process.

HEAs	Powder process	AM	AM parameters	Phase	Properties	Applications	Ref.
TiTaNbMoZr	Ball milling	Micro-plasma arc process	Laser Power - 418 W Mass flow rate HEA - 1.7 g/min Deposition speed - 53 mm/min Stand-off distance - 9 mm Shielding gas flow rate - 5 NL/min Plasma gas flow rate - 0.3 NL/min	BCC	Cell viability - 90% (HeLa), 88% (HEK-293), and 92% (BHK). Released ions - 37 (Ti), 26 (Ta), 57 (Nb), 38 (Mo), and 28 ppb (Zr) under simulated body fluid solution.	Biocompatibility is evaluated by cell viability, released ions, and corrosion behavior for knee implant applications.	[187]
Ti <sub>1.4</sub> Nb <sub>0.6</sub> Ta <sub>0.6</sub> Zr <sub>1.4</sub> Mo <sub>0.6</sub>	Gas atomization	SLM	Laser power - 360 W Scanning speed - 1200 mm/s Hatch distance - 80 μm Layer thickness - 60 μm	BCC	Proof stress - 1690 MPa	Complex shape customization with reduced porosity obtained by hindering elemental segregation	[188]
Ti <sub>25</sub> Nb <sub>3</sub> Zr <sub>3</sub> Mo <sub>2</sub> Sn	Plasma rotating electrode process	LENS	Laser power - 1.4–1.7 kW Laser beam dia. - 1.5 mm Laser scanning speed - 5–7 mm/s HEA feed rate - 1.5–2.0 g/min Carrier gas flow rate - 280–320 L/hr.	β & α phase	-	AM process supports cell adhesion and spreading.	[192]
Ti <sub>1.5</sub> NbTa <sub>0.5</sub> ZrMo <sub>0.5</sub>	Gas atomization	SLM	Laser power - 300 W Scanning speed - 1000 mm/s, Incubation distance - 0.1 mm Layer thickness - 0.05 mm.	BCC	Compressive yield strength - 253.62–523.76 MPa Young's modulus - 6.71–16.21 GPa	Achieved a very close Young's modulus of human trabecular bone.	[190]
TiZrNbMoV	-	LENS	Laser power - 300 W Scanning speed - 5 mm/s Layer thickness - 0.25 mm.	BCC	-	Formation of BCC phase, lattice distortion effect of HEAs, threefold remelting, and no structural damages observed under hydrogenation.	[97]
LaNiFeVMn	Gas atomization	LENS	Laser power – 200–300 W Scanning speed - 1.6 mm/s Layer thickness - 0.10 mm	BCC	-	The hydrogen storage depends on the atomic content of lanthanum, and no relationship is observed between phase and pressure compositions.	[195]
ZrTiVCrFeNi	Gas atomization	LENS	Laser power - 200–300 W, Scanning speed - 1.6 mm/s Layer thickness - 0.10 mm.	C14 leaves phase	-	The hydrogen capacity of 1.81 and 1.56 wt% are obtained on HEAs after synthesis and annealed at 1000°C for 24 hrs.	[86]
CoCrFeCuNi	Gas atomization	SLM	Laser power – 180–300 W, Scanning speed – 1000–2000 mm/s, Hatch distance - 0.05 mm Layer thickness - 0.03 mm Energy density - 60–160 J/mm <sup>3</sup>	FCC	Average yield strength – 516 MPa	The enhanced antibacterial ability of CoCrFeCuNi HEA is potentially applicable in medical and other environments.	[193]
CrMnFeCoNi	Gas atomization	LMD	Laser power - 1000–1400 W Laser beam dia. - 1.8 mm HEA feed rate - 7–9 g/min Ar gas flow rate - 15–18 L/hr	FCC	Tensile strength - 878 MPa Yield strength - 402 MPa % of plastic strain - 95%	Enhanced mechanical properties are obtained even at cryogenic temperatures.	[171]
FeCoCrAlCu	-	LMD	Laser power – 1000–3000 W Scanning speed –	-	-	A crack-free aviation turbine blade fabricated with an ultrafine nanocrystal structure.	[200]

(continued on next page)

**Table 5 (continued)**

HEAs	Powder process	AM	AM parameters	Phase	Properties	Applications	Ref.
AlCoCrFeNi	Gas atomization	SLM	1–15 mm/s HEA feed rate – 5–30 g/min Laser power –120 W Hatch distance - 50–80 µm Layer thickness - 25 µm	BCC	Hardness - 541±18 HV	The processed sample is used as a filter in nuclear and oxidation at extreme conditions due to the linear pattern microstructure.	[202]
AlTiCrFeCoNi, AlCoCrFeNiCu	-	laser deposition process	Laser power - 600–1200 W Scanning speed - 4–12 mm/s Laser beam dia. - 2 mm Layer thickness - 0.5 mm	FCC & BCC	Hardness - 389–837 HV (AlTiCrFeCoNi) & 380–527 HV (AlCoCrFeNiCu)	The surface properties of A301 steel are enhanced by defect-free structures for structural application. Laser power plays a significant factor in mechanical properties.	[126]
Al <sub>2</sub> CrFeCo <sub>x</sub> CuNiTi	-	Laser cladding	Laser power - 2000–3000 W Scanning speed - 3–6 mm/s Laser beam dia. - 4 mm Layer thickness - 1 mm	-	The corrosion rate is reduced to 1–2 orders of Q235 steel	A fine equalized columnar grain suppressed the crack by hindering the residual stress.	[209]
MoFe <sub>1.5</sub> CrTiWAlNb <sub>x</sub>	-	Laser cladding	-	BCC, & C14-Laves	Microhardness - 910 HV Wear volume - 0.045 mm <sup>3</sup>	The rapid heating and cooling of laser cladding leads to a fine-grain structure.	[208]

The behavior of HEAs under such conditions necessitates extensive research to determine their performance and reliability in high-temperature environments.

- The mechanical properties, wear resistance, corrosion behavior, and interfacial bonding strength of samples majorly depend on HEAs. Hence, more attention is required while selecting the principal elements in HEAs and synthesis methods.
- Further investigation is needed to comprehensively understand the role of laser power as a process parameter in AM. Specifically, its influence on grain formation and its effect on producing high-quality AM-HEA products should be studied. Besides, the presence of intermetallic precipitates and coarse grains can negatively affect the properties of AM-processed samples due to the rapid heating and cooling process. Future research should focus on developing strategies to minimize these issues and improve the overall properties of AM-HEA products.
- Surface defects such as voids, pores, and microcracks have a significant impact on the mechanical behavior of AM-processed samples, affecting properties such as creep, fatigue, and tensile strength. It is imperative to give prime attention to minimizing these defects to enhance the overall properties of AM-printed components. Additionally, investigating microcracks, intermetallic precipitation, and voids: In-depth investigations involving both experimental and mathematical modeling approaches are necessary to gain a comprehensive understanding of the mechanisms behind microcrack formation, intermetallic precipitation, and the presence of voids in AM-processed samples.
- The optimization of various process parameters, including laser power, layer thickness, hatching space, scanning speed, and their strategies, should be explored to achieve high-quality AM-HEA products with improved properties. Also, future investigations should focus on studying the formation of precipitation, phase structure, and microstructure in AM-printed samples to better understand their influence on the properties of HEAs.
- While the evaluation of microhardness and tensile properties has received significant attention, future research should also explore other essential properties, such as fatigue behavior, fracture toughness, and creep resistance in AM-HEA applications. These properties

play a crucial role in real-world applications and should be thoroughly investigated. Moreover, the formation of residual stresses during the AM process is an area that requires more attention. Investigating the mechanisms behind residual stress formation and its influence on the tensile properties of AM-processed samples will contribute to a deeper understanding of the overall behavior of HEAs.

- Atomistic simulation techniques, including molecular dynamics simulation, Monte Carlo simulation, density functional theory, ab initio molecular dynamics, and cluster expansion Methods, are used to understand the behavior of HEAs. These simulation techniques indeed provide insight into the mechanical properties, phase stability, and atomic-scale structure of HEAs.
- To achieve cost-effective optimization techniques for predicting phase and mechanical properties, the Machine Learning (ML) approach can be employed for rapid analysis. ML utilizes a backup database that includes influential parameters for HEA formation, such as atomic size difference, electronegativity, valence electron concentration mixing entropy, mixing enthalpy, as well as AM printing techniques and their process parameters, and induced mechanical, wear, and corrosion properties. ML algorithms are capable of constructing atomic interaction models based on atomistic simulation techniques, enabling the correlation of complex interactions within HEA elements. These models have evolved to encompass both atomistic simulations at the atomic scale and macro-scale predictions of physical properties. While ML offers promise in alloy screening and AM parameter optimization, the diverse range of ML algorithms and material descriptors necessitates a systematic approach to identify the optimal combination of descriptors and algorithms. Furthermore, many ML algorithms, particularly those involving deep learning, lack interpretability and are often considered as opaque "black boxes." Therefore, it is vital to prioritize efforts to improve the interpretability of ML models and enhance their efficiency and accuracy in decision-making processes.

## 8. Summary and concluding remarks

The review article presents a comprehensive analysis of recent

**Table 6**  
Summary of findings.

Key findings	Implications	Research gaps	Future directions
AM enables rapid prototyping and customization in HEAs.	Increased design flexibility and reduced lead times.	The research proficiency in the correlation between the design of intricate shapes, printing technologies, and raw materials could be a potential research direction.	Explore optimization of AM parameters such as laser power, scanning speed, layer thickness, and hatching space for HEAs
Rapid solidification in AM leads to enhanced mechanical properties, such as high strength and hardness in HEAs	Improved material performance in various applications	The research explores the constituent materials involved in the AM process, the cooling rate of each element, and layer thickness. The speed of cooling is crucial in determining the microstructure of the material.	Investigate the effect of cooling rates on microstructure and properties.
Residual stresses and uneven microstructures are inherent in AM-processed HEAs.	Further heat treatment can refine the microstructure and reduce residual stresses.	The research expertise is in the area of processing raw materials, flowability, bonding of adjacent layers, the thermal gradient of materials, and post-processing to reduce porosity and uneven microstructures of printed samples.	Develop post-processing methods to enhance AM-processed HEAs.
Surface finish in AM-processed HEAs may require additional polishing or post-processing steps.	Ensuring desired aesthetics and functional properties.	Existing characterization techniques like SEM and TEM might not be entirely suitable for evaluating the surface finish of AM-processed HEAs. Developing and validating specialized characterization techniques tailored to AM-processed HEAs could be a potential research direction.	Study surface treatment techniques for AM-processed HEAs.
AM in HEAs offers the potential to manufacture both small and large complex products.	Increased possibilities for intricate and customized designs	The AM techniques like PBF and DED have been successful in producing small intricate parts, but the process parameters and conditions for large complex parts are not well-defined. Research focusing on optimizing AM parameters such as scanning speed, laser power, and powder	Investigate scalability and cost-effectiveness for large-scale production.

**Table 6 (continued)**

Key findings	Implications	Research gaps	Future directions
			characteristics specifically for large-scale HEA components is needed.

advancements in AM-processed HEAs, aiming to address the current state of the field. The study encompasses the formation of HEAs, the utilization of powder feedstock in the AM process, the properties related to strengthening, and various applications. The article examines the impact of different AM process parameters on phase formation, as well as the resulting mechanical and microstructural properties of the built samples. The intricate relationship between microstructure, induced phases, and precipitates, and their influence on mechanical properties such as tensile strength, yield strength, and elongation, is described in great detail. Furthermore, the utilization of AM-processed HEAs across different sectors and their specific applications are highlighted towards the end of the paper. The article comprehensively explores the challenges encountered during the AM process, identifies current research gaps, and suggests future directions. This review provides valuable insights and opens up new avenues for expanding knowledge in the field of AM-processed HEAs. Additionally, Table 6 presents a summary of the findings, providing a concise overview of the key results and conclusions derived from the research.

#### CRediT authorship contribution statement

**Bassiony Saleh:** Writing – review & editing, Writing – original draft, Methodology, Investigation. **Radhika N:** Writing – review & editing, Validation, Supervision, Project administration. **Ragunath S:** Writing – original draft, Methodology, Investigation, Data curation, Conceptualization.

#### Declaration of Competing Interest

The authors declare that they have no known competing financial interests or personal relationships that could have appeared to influence the work reported in this paper.

#### Data Availability

No data was used for the research described in the article.

#### Acknowledgement

This research received no specific grant from any funding agency in the public, commercial, or not-for-profit sectors.

#### References

- [1] S.S. Basu, P.P. Jana, M. Ghosh, A new insight into the phase stability in high entropy alloys, Mater. Today Commun. 37 (2023) 107394, <https://doi.org/10.1016/J.MTCOMM.2023.107394>.
- [2] S. Ragunath, N. Radhika, S. Aravind Krishna, N. Jayaprakash, Synthesis of high entropy alloy for surface modification by friction stir process: recent advances and future directions, Met. Mater. Int. 2023 (2023) 1–30, <https://doi.org/10.1007/S12540-023-01584-7>.
- [3] S.A. Krishna, N. Radhika, B. Saleh, S. Manivannan, Microstructural mechanical and corrosion properties of SS304/HEA surface layer produced by Friction Stir Processing, J. Alloy. Compd. 953 (2023) 170153, <https://doi.org/10.1016/J.JALCOM.2023.170153>.
- [4] S.A. Krishna, N. Noble, N. Radhika, B. Saleh, A comprehensive review on advances in high entropy alloys: Fabrication and surface modification methods, properties, applications, and future prospects, J. Manuf. Process 109 (2024) 583–606, <https://doi.org/10.1016/J.JMAPRO.2023.12.039>.

- [5] N. Kaushik, A. Meena, H.S. Mali, High entropy alloy synthesis, characterisation, manufacturing & potential applications: a review, *Mater. Manuf. Process.* 37 (2022) 1085–1109, <https://doi.org/10.1080/10426914.2021.2006223>.
- [6] P. Das, R. Nandan, P.M. Pandey, A Review on Corrosion Properties of High Entropy Alloys Fabricated by Additive Manufacturing, *Trans. Indian Inst. Met.* 75 (2022) 2465–2476, <https://doi.org/10.1007/S12666-022-02610-9/FIGURES/6>.
- [7] Y. Chen, B. Li, B. Chen, F. Xuan, High-cycle fatigue induced twinning in CoCrFeNi high-entropy alloy processed by laser powder bed fusion additive manufacturing, *Addit. Manuf.* 61 (2023) 103319, <https://doi.org/10.1016/J.ADDMA.2022.103319>.
- [8] W.H. Guo, J. Li, M. Qi, Y. Xu, H.R. Ezatpour, Effects of heat treatment on the microstructure, mechanical properties and corrosion resistance of AlCoCrFeNiTi0.5 high-entropy alloy, *J. Alloy. Compd.* 884 (2021) 161026, <https://doi.org/10.1016/J.JALLCOM.2021.161026>.
- [9] F. Yousefan, A. Ashrafi, S.M. Monir Vaghefi, Corrosion and tribological behavior of CoCrFeMoNi high-entropy alloys as a potential vascular implant material, *J. Alloy. Compd.* 976 (2024) 172964, <https://doi.org/10.1016/J.JALLCOM.2023.172964>.
- [10] M.D. Alcalá, C. Real, I. Fombella, I. Trigo, J.M. Córdoba, Effects of milling time, sintering temperature, Al content on the chemical nature, microhardness and microstructure of mechanochemically synthesized FeCoNiCrMn high entropy alloy, *J. Alloy. Compd.* 749 (2018) 834–843, <https://doi.org/10.1016/J.JALLCOM.2018.03.358>.
- [11] O.T. Onawale, P.V. Cobinah, R.A. Nzeukou, W.R. Matizamhuka, Synthesis route, microstructural evolution, and mechanical property relationship of high-entropy alloys (HEAs): A review, *Mater.* 14 (2021), <https://doi.org/10.3390/ma14113065>.
- [12] Z. Li, K.G. Pradeep, Y. Deng, D. Raabe, C.C. Tasan, Metastable high-entropy dual-phase alloys overcome the strength–ductility trade-off, *Nature* 2016 534 (7606 534) (2016) 227–230, <https://doi.org/10.1038/nature17981>.
- [13] C. Chen, Y. Fan, W. Wang, H. Zhang, J. Hou, R. Wei, T. Zhang, T. Wang, M. Li, S. Guan, F. Li, Synthesis of ultrafine dual-phase structure in CrFeCoNiAl0.6 high entropy alloy via solid-state phase transformation during sub-rapid solidification, *J. Mater. Sci. Technol.* 113 (2022) 253–260, <https://doi.org/10.1016/J.JMST.2021.09.013>.
- [14] S. Ragunath, N. Radhika, S. Aravind Krishna, N. Jeyaprakash, Enhancing microstructural, mechanical and tribological behaviour of AlSiBeTiV high entropy alloy reinforced SS410 through friction stir processing, *Tribol. Int.* 188 (2023) 108840, <https://doi.org/10.1016/J.TRIBOINT.2023.108840>.
- [15] H. OSMAN, L. LIU, Additive manufacturing of high-entropy alloy composites: A review, *Trans. Nonferrous Met. Soc. China* 33 (2023) 1–24, [https://doi.org/10.1016/S1003-6326\(22\)66086-2](https://doi.org/10.1016/S1003-6326(22)66086-2).
- [16] M. Seifi, A. Salem, J. Beuth, O. Harrysson, J.J. Lewandowski, Overview of Materials Qualification Needs for Metal Additive Manufacturing, *JOM* 68 (2016) 747–764, <https://doi.org/10.1007/S11837-015-1810-0/FIGURES/14>.
- [17] S. Tammas-Williams, I. Todd, Design for additive manufacturing with site-specific properties in metals and alloys, *Scr. Mater.* 135 (2017) 105–110, <https://doi.org/10.1016/J.SCRIPTAMAT.2016.10.030>.
- [18] S. Chen, Y. Tong, P.K. Liaw, Additive Manufacturing of High-Entropy Alloys: A Review, Vol. 20, Page 937, *Entropy* 20 (2018) 937, <https://doi.org/10.3390/E20120937>.
- [19] B. Saleh, R. Fathi, Y. Tian, N. Radhika, J. Jiang, A. Ma, Fundamentals and advances of wire arc additive manufacturing: materials, process parameters, potential applications, and future trends, 2023 23:2, ACME 23 (2023) 1–71, <https://doi.org/10.1007/S43452-023-00633-7>.
- [20] S. Sonal, J. Lee, Recent advances in additive manufacturing of high entropy alloys and their nuclear and wear-resistant applications, 2021, Vol. 11, Page 1980, *Metals* 11 (2021) 1980, <https://doi.org/10.3390/MET1121980>.
- [21] T.D. Ngo, A. Kashani, G. Imbalzano, K.T.Q. Nguyen, D. Hui, Additive manufacturing (3D printing): A review of materials, methods, applications and challenges, *Compos. B Eng.* 143 (2018) 172–196, <https://doi.org/10.1016/J.COMPOSITESB.2018.02.012>.
- [22] A. Nouri, A. Rohani Shirvani, Y. Li, C. Wen, Additive manufacturing of metallic and polymeric load-bearing biomaterials using laser powder bed fusion: a review, *J. Mater. Sci. Technol.* 94 (2021) 196–215, <https://doi.org/10.1016/J.JMST.2021.03.058>.
- [23] R. Sundaram, R. Nachimuthu, A.K. Sivanandam, J. Natarajan, Electrochemical and hot corrosion behaviour of steel reinforced with AlSiBeTiV high entropy alloy using friction stir processing, *Sci. Technol. Adv. Mater.* 25 (2024), <https://doi.org/10.1080/14686996.2024.2320083>.
- [24] Y. Sun, R.J. Hebert, M. Aindow, Effect of laser scan length on the microstructure of additively manufactured 17-4PH stainless steel thin-walled parts, *Addit. Manuf.* 35 (2020) 101302, <https://doi.org/10.1016/J.ADDMA.2020.101302>.
- [25] Md.R.U. Ahsan, G.-J. Seo, X. Fan, P.K. Liaw, S. Motaman, C. Haase, D.B. Kim, Effects of process parameters on bead shape, microstructure, and mechanical properties in wire + arc additive manufacturing of Al0.1CoCrFeNi high-entropy alloy, *J. Manuf. Process.* 68 (2021) 1314–1327, <https://doi.org/10.1016/J.JMAPRO.2021.06.047>.
- [26] N. Noble, N. Radhika, M. Sathishkumar, B. Saleh, Characterisation and property evaluation of High Entropy Alloy coating on 316L steel via thermal spray synthesis, *Tribol. Int.* 185 (2023) 108525, <https://doi.org/10.1016/J.JTRIBOINT.2023.108525>.
- [27] D.B. Miracle, O.N. Senkov, A critical review of high entropy alloys and related concepts, *Acta Mater.* 122 (2017) 448–511, <https://doi.org/10.1016/J.ACTAMAT.2016.08.081>.
- [28] A. Kumar, M. Gupta, An Insight into Evolution of Light Weight High Entropy Alloys: A Review, 2016, Vol. 6, Page 199, *Metals* 6 (2016) 199, <https://doi.org/10.3390/MET6090199>.
- [29] E.J. Pickering, N.G. Jones, High-entropy alloys: a critical assessment of their founding principles and future prospects, *Int. Mater. Rev.* 61 (2016) 183–202, <https://doi.org/10.1080/09506608.2016.1180020>.
- [30] A. Kumar, A. Singh, A. Suhane, Mechanically alloyed high entropy alloys: existing challenges and opportunities, *J. Mater. Res. Technol.* 17 (2022) 2431–2456, <https://doi.org/10.1016/J.JMRT.2022.01.141>.
- [31] S. Praveen, H.S. Kim, High-Entropy Alloys: Potential Candidates for High-Temperature Applications – An Overview, *Adv. Eng. Mater.* 20 (2018) 1700645, <https://doi.org/10.1002/ADEM.201700645>.
- [32] Q. Li, W. Chen, J. Zhong, L. Zhang, Q. Chen, Z.K. Liu, On Sluggish Diffusion in Fcc Al-Co-Cr-Fe-Ni high-entropy alloys: an experimental and numerical study, 2018, Vol. 8, Page 16, *Metals* 8 (2017) 16, <https://doi.org/10.3390/MET8010016>.
- [33] J. Dąbrowska, M. Zajusz, W. Kucza, G. Cieślak, K. Berent, T. Czeppe, T. Kulik, M. Danielewski, Demystifying the sluggish diffusion effect in high entropy alloys, *J. Alloy. Compd.* 783 (2019) 193–207, <https://doi.org/10.1016/J.JALLCOM.2018.12.300>.
- [34] J.W. Yeh, Physical Metallurgy of High-Entropy Alloys, *JOM* 67 (2015) 2254–2261, <https://doi.org/10.1007/S11837-015-1583-5/FIGURES/16>.
- [35] H.S. Oh, D. Ma, G.P. Leyson, B. Grabowski, E.S. Park, F. Kormann, D. Raabe, Lattice Distortions in the FeCoNiCrMn high entropy alloy studied by theory and experiment, 2016, Vol. 18, Page 321, *Entropy* 18 (2016) 321, <https://doi.org/10.3390/E18090321>.
- [36] Z. Wang, J. Li, Q.H. Fang, B. Liu, L. Zhang, Investigation into nanoscratching mechanical response of AlCrCuFeNi high-entropy alloys using atomic simulations, *Appl. Surf. Sci.* 416 (2017) 470–481, <https://doi.org/10.1016/J.APSUSC.2017.04.009>.
- [37] N. Ali, L. Zhang, D. Liu, H. Zhou, K. Sanaullah, C. Zhang, J. Chu, Y. Nian, J. Cheng, Strengthening mechanisms in high entropy alloys: A review, *Mater. Today Commun.* 33 (2022) 104686, <https://doi.org/10.1016/J.JMTCOMM.2022.104686>.
- [38] I. Basu, J.T.M. De Hosson, Strengthening mechanisms in high entropy alloys: Fundamental issues, *Scr. Mater.* 187 (2020) 148–156, <https://doi.org/10.1016/J.SCRIPTAMAT.2020.06.019>.
- [39] R.S. Mishra, R.S. Haridas, P. Agrawal, High entropy alloys – Tunability of deformation mechanisms through integration of compositional and microstructural domains, *Mater. Sci. Eng. A* 812 (2021) 141085, <https://doi.org/10.1016/J.MSEA.2021.141085>.
- [40] J. Liu, X. Wang, A.P. Singh, H. Xu, F. Kong, F. Yang, The Evolution of Intermetallic Compounds in High-Entropy Alloys: From the Secondary Phase to the Main Phase, 2021, Vol. 11, Page 2054, *Metals* 11 (2021) 2054, <https://doi.org/10.3390/MET1122054>.
- [41] Y.H. Zhang, Y. Zhuang, A. Hu, J.J. Kai, C.T. Liu, The origin of negative stacking fault energies and nano-twin formation in face-centered cubic high entropy alloys, *Scr. Mater.* 130 (2017) 96–99, <https://doi.org/10.1016/J.SCRIPTAMAT.2016.11.014>.
- [42] L. Li, R.D. Kamachali, Z. Li, Z. Zhang, Grain boundary energy effect on grain boundary segregation in an equiatomic high-entropy alloy, *Phys. Rev. Mater.* 4 (2020) 053603, <https://doi.org/10.1103/PHYSREVMATERIALS.4.053603/FIGURES/9/MEDIUM>.
- [43] D. Huang, Y. Zhuang, Break the strength–ductility trade-off in a transformation-induced plasticity high-entropy alloy reinforced with precipitation strengthening, *J. Mater. Sci. Technol.* 108 (2022) 125–132, <https://doi.org/10.1016/J.JMST.2021.08.061>.
- [44] S. Fu, H. Bei, Y. Chen, T.K. Liu, D. Yu, K. An, Deformation mechanisms and work-hardening behavior of transformation-induced plasticity high entropy alloys by in-situ neutron diffraction, *Mater. Res. Lett.* 6 (2018) 620–626, <https://doi.org/10.1080/21663831.2018.1523239>.
- [45] W. Zhang, P.K. Liaw, Y. Zhang, Science and technology in high-entropy alloys, 2017 61:1, *Sci. China Mater.* 61 (2018) 2–22, <https://doi.org/10.1007/S40843-017-9195-8>.
- [46] M.C. Gao, P.K. Liaw, J.W. Yeh, Y. Zhang, High-entropy alloys: Fundamentals and applications, *High-Entropy Alloy.: Fundam. Appl.* (2016) 1–516, <https://doi.org/10.1007/978-3-319-27013-5/COVER>.
- [47] Y. Zhang, T.T. Zuo, Z. Tang, M.C. Gao, K.A. Dahmen, P.K. Liaw, Z.P. Lu, Microstructures and properties of high-entropy alloys, *Prog. Mater. Sci.* 61 (2014) 1–93, <https://doi.org/10.1016/J.PMATSCL.2013.10.001>.
- [48] X. Yang, S.Y. Chen, J.D. Cotton, Y. Zhang, Phase Stability of Low-Density, Multiprincipal Component Alloys Containing Aluminum, Magnesium, and Lithium, *JOM* 66 (2014) 2009–2020, <https://doi.org/10.1007/S11837-014-1059-Z/FIGURES/6>.
- [49] B. Chanda, J. Das, Composition Dependence on the Evolution of Nanoeutectic in CoCrFeNiNb<sub>x</sub> (0.45 ≤ x ≤ 0.65) High Entropy Alloys, *Adv. Eng. Mater.* 20 (2018) 1700908, <https://doi.org/10.1002/ADEM.201700908>.
- [50] J. li Zhou, J. yong Yang, X. feng Zhang, F. wen Ma, K. Ma, Y. hai Cheng, Research status of tribological properties optimization of high-entropy alloys: a review, 2023 58:10, *J. Mater. Sci.* 58 (2023) 4257–4291, <https://doi.org/10.1007/S10853-023-08255-3>.
- [51] S. Singh, S. Ramakrishna, R. Singh, Material issues in additive manufacturing: A review, *J. Manuf. Process.* 25 (2017) 185–200, <https://doi.org/10.1016/J.JMAPRO.2016.11.006>.
- [52] Y. Kok, X.P. Tan, P. Wang, M.L.S. Nai, N.H. Loh, E. Liu, S.B. Tor, Anisotropy and heterogeneity of microstructure and mechanical properties in metal additive

- manufacturing: A critical review, *Mater. Des.* 139 (2018) 565–586, <https://doi.org/10.1016/J.MATDES.2017.11.021>.
- [53] M. Molitech-Hou, Overview of additive manufacturing process, *Addit. Manuf.: Mater., Process., Quantif. Appl.* (2018) 1–38, <https://doi.org/10.1016/B978-0-12-812155-9.00001-3>.
- [54] S. Zhao, X. Shen, J. Yang, W. Teng, Y. Wang, Densification behavior and mechanical properties of nanocrystalline TiC reinforced 316L stainless steel composite parts fabricated by selective laser melting, *Opt. Laser Technol.* 103 (2018) 239–250, <https://doi.org/10.1016/J.OPTLASTEC.2018.01.005>.
- [55] B. Vrancken, L. Thijss, J.P. Kruth, J. Van Humbeeck, Heat treatment of Ti6Al4V produced by Selective Laser Melting: Microstructure and mechanical properties, *J. Alloy. Compd.* 541 (2012) 177–185, <https://doi.org/10.1016/J.JALLCOM.2012.07.022>.
- [56] M. Laleh, E. Sadeghi, R.I. Revilla, Q. Chao, N. Haghdam, A.E. Hughes, W. Xu, I. De Graeve, M. Qian, J. Gibson, M.Y. Tan, Heat treatment for metal additive manufacturing, *Prog. Mater. Sci.* 133 (2023) 101051, <https://doi.org/10.1016/J.PMATSCL.2022.101051>.
- [57] A. Ostovari Moghaddam, N.A. Shaburova, M.N. Samodurova, A. Abdollahzadeh, E.A. Trofimov, Additive manufacturing of high entropy alloys: a practical review, *J. Mater. Sci. Technol.* 77 (2021) 131–162, <https://doi.org/10.1016/J.JMST.2020.11.029>.
- [58] A. Ostovari Moghaddam, A. Shokuhfar, A. Cabot, Thermoelectric properties of nanostructured bornite Cu<sub>5-x</sub>CoxFeS4 synthesized by high energy ball milling, *J. Alloy. Compd.* 750 (2018) 1–7, <https://doi.org/10.1016/J.JALLCOM.2018.03.408>.
- [59] S.N. Kishan, R.A. Sree, U.V. Akhil, N. Radhika, Electrochemical and hot corrosion analysis of novel AlBeSiTiV light weight HEA coating on SS316, *Phys. Scr.* 99 (2024) 025979, <https://doi.org/10.1088/1402-4896/AD1F18>.
- [60] S.P. Dwivedi, S. Sharma, Synthesis of high entropy alloy AlCoCrFeNiCuSn reinforced AlSi7Mg0.3 based composite developed by solid state technique, *Mater. Lett.* 355 (2024) 135556, <https://doi.org/10.1016/J.MATLET.2023.135556>.
- [61] M. Huang, J. Jiang, Y. Wang, Y. Liu, Y. Zhang, Effects of milling process parameters and PCAs on the synthesis of Al0.8Co0.5Cr1.5CuFeNi high entropy alloy powder by mechanical alloying, *Mater. Des.* 217 (2022) 110637, <https://doi.org/10.1016/J.MATDES.2022.110637>.
- [62] B. Li, B. Qian, Y. Xu, Z. Liu, F. Xuan, Fine-structured CoCrFeNiMn high-entropy alloy matrix composite with 12 wt% TiN particle reinforcements via selective laser melting assisted additive manufacturing, *Mater. Lett.* 252 (2019) 88–91, <https://doi.org/10.1016/J.MATLET.2019.05.108>.
- [63] C. Nagarjuna, K. Yong Jeong, Y. Lee, S. Min Woo, S. Ig Hong, H. Seop Kim, S. J. Hong, Strengthening the mechanical properties and wear resistance of CoCrFeMnNi high entropy alloy fabricated by powder metallurgy, *Adv. Powder Technol.* 33 (2022) 103519, <https://doi.org/10.1016/J.APT.2022.103519>.
- [64] S. Ragunath, N. Radhika, S.A. Krishna, L. Rajeshkumar, A study on microstructural, mechanical properties and optimization of wear behavior of friction stir processed AlCrCoFeNi High Entropy Alloy reinforced SS410 using response surface methodology, *Heliyon* 10 (2024) e24429, <https://doi.org/10.1016/J.HELIYON.2024.E24429>.
- [65] A. Zavdoveev, Ł. Zrodowski, D. Vedel, P. Cortes, T. Choma, M. Ostrytz, O. Stasiuk, T. Baudin, A. Klapatuk, A. Gaivoronskiy, V. Bevz, E. Pashinska, M. Skoryk, Atomization of the Fe-rich MnNiCoCr high-entropy alloy for spherical powder production, *Mater. Lett.* 363 (2024) 136240, <https://doi.org/10.1016/J.MATLET.2024.136240>.
- [66] C.C. Yang, J.L. Hang Chau, C.J. Weng, C.S. Chen, Y.H. Chou, Preparation of high-entropy AlCoCrCuFeNiSi alloy powders by gas atomization process, *Mater. Chem. Phys.* 202 (2017) 151–158, <https://doi.org/10.1016/J.MATCHMPHYS.2017.09.014>.
- [67] Y. Wang, R. Li, P. Niu, Z. Zhang, T. Yuan, J. Yuan, K. Li, Microstructures and properties of equimolar AlCoCrCuFeNi high-entropy alloy additively manufactured by selective laser melting, *Intermet. (Barking)* 120 (2020) 106746, <https://doi.org/10.1016/J.JINTERMET.2020.106746>.
- [68] Z. Ren, S. Zhu, X. Wang, Y. Zhao, G. Han, K. Zhou, W. Wang, G. Tian, Preparation and Microstructure of Multi-Component High Entropy Alloy Powders Fabricated by Gas Atomization Method, 2023, Vol. 13, Page 432, *Metals* 13 (2023) 432, <https://doi.org/10.3390/MET13020432>.
- [69] S. cheng ZHOU, P. ZHANG, Y. fei XUE, F. chi WANG, L. WANG, T. qing CAO, Z. TAN, B. yuan CHENG, B. peng WANG, Microstructure evolution of Al0.6CoCrFeNi high entropy alloy powder prepared by high pressure gas atomization, *Trans. Nonferrous Met. Soc. China* 28 (2018) 939–945, [https://doi.org/10.1016/S1003-6326\(18\)64728-4](https://doi.org/10.1016/S1003-6326(18)64728-4).
- [70] J.M. Park, J.W. Kang, W.H. Lee, S.Y. Lee, S.H. Min, T.K. Ha, H.K. Park, Preparation of spherical WTaMoNbV refractory high entropy alloy powder by inductively-coupled thermal plasma, *Mater. Lett.* 255 (2019) 126513, <https://doi.org/10.1016/J.MATLET.2019.126513>.
- [71] M. Xia, Y. Chen, R. Wang, X. Liang, B. Shen, Fabrication of spherical MoNbTaWZr refractory high-entropy powders by spray granulation combined with plasma spheroidization, *J. Alloy. Compd.* 931 (2023) 167542, <https://doi.org/10.1016/J.JALLCOM.2022.167542>.
- [72] M.A. Khan, M. Hamza, J. Brechtl, Z. Nazir, N.A. Qaisrani, G. Yasin, T. Ahmad, W. B. Liao, P.K. Liaw, M.A. Afifi, Development and characterization of a low-density TiNbZrAlTa refractory high entropy alloy with enhanced compressive strength and plasticity, *Mater. Charact.* 205 (2023) 113301, <https://doi.org/10.1016/J.MATCHAR.2023.113301>.
- [73] M. Xia, Y. Chen, K. Chen, Y. Tong, X. Liang, B. Shen, Synthesis of WTaMoNbZr refractory high-entropy alloy powder by plasma spheroidization process for additive manufacturing, *J. Alloy. Compd.* 917 (2022) 165501, <https://doi.org/10.1016/J.JALLCOM.2022.165501>.
- [74] J. Li, H. Luan, L. Zhou, A. Amar, R. Li, L. Huang, X. Liu, G. Le, X. Wang, J. Wu, C. Jiang, Phase transformation - induced strengthening of an additively manufactured multi- principal element CrMnFeCoNi alloy, *Mater. Des.* 195 (2020) 108999, <https://doi.org/10.1016/J.MATDES.2020.108999>.
- [75] A. Amar, J. Li, S. Xiang, X. Liu, Y. Zhou, G. Le, X. Wang, F. Qu, S. Ma, W. Dong, Q. Li, Additive manufacturing of high-strength CrMnFeCoNi-based High Entropy Alloys with TiC addition, *Intermet. (Barking)* 109 (2019) 162–166, <https://doi.org/10.1016/J.JINTERMET.2019.04.005>.
- [76] M. Moorehead, K. Bertsch, M. Niezgoda, C. Parkin, M. Elbakshwan, K. Sridharan, C. Zhang, D. Thoma, A. Couet, High-throughput synthesis of Mo-Nb-Ta-W high-entropy alloys via additive manufacturing, *Mater. Des.* 187 (2020) 108358, <https://doi.org/10.1016/J.MATDES.2019.108358>.
- [77] P. Gu, T. Qi, L. Chen, T. Ge, X. Ren, Manufacturing and analysis of VNbMoTaW refractory high-entropy alloy fabricated by selective laser melting, *Int. J. Refract. Met. Hard Mater.* 105 (2022) 105834, <https://doi.org/10.1016/J.IJRMHM.2022.105834>.
- [78] K. Zhou, Z. Wang, F. He, S. Liu, J. Li, J. jung Kai, J. Wang, A precipitation-strengthened high-entropy alloy for additive manufacturing, *Addit. Manuf.* 35 (2020) 101410, <https://doi.org/10.1016/J.ADDMA.2020.101410>.
- [79] H. Peng, S. Xie, P. Niu, Z. Zhang, T. Yuan, Z. Ren, X. Wang, Y. Zhao, R. Li, Additive manufacturing of Al0.3CoCrFeNi high-entropy alloy by powder feeding laser melting deposition, *J. Alloy. Compd.* 862 (2021) 158286, <https://doi.org/10.1016/J.JALLCOM.2020.158286>.
- [80] Y. Zhu, S. Zhou, Z. Xiong, Y.J. Liang, Y. Xue, L. Wang, Enabling stronger eutectic high-entropy alloys with larger ductility by 3D printed directional lamellae, *Addit. Manuf.* 39 (2021) 101901, <https://doi.org/10.1016/J.JADDMA.2021.101901>.
- [81] Y. Bai, H. Jiang, K. Yan, M. Li, Y. Wei, K. Zhang, B. Wei, Phase transition and heterogeneous strengthening mechanism in CoCrFeNiMn high-entropy alloy fabricated by laser-engineered net shaping via annealing at intermediate-temperature, *J. Mater. Sci. Technol.* 92 (2021) 129–137, <https://doi.org/10.1016/J.JMST.2021.03.028>.
- [82] M.S.K.K.Y. Nartu, T. Alam, S. Dasari, S.A. Mantri, S. Gorsse, H. Siller, N. Dahotre, R. Banerjee, Enhanced tensile yield strength in laser additively manufactured Al0.3CoCrFeNi high entropy alloy, *Mater. (Oxf.)* 9 (2020) 100522, <https://doi.org/10.1016/J.MTLA.2019.100522>.
- [83] S. Guan, K. Solberg, D. Wan, F. Berto, T. Welo, T.M. Yue, K.C. Chan, Formation of fully equiaxed grain microstructure in additively manufactured AlCoCrFeNiTi0.5 high entropy alloy, *Mater. Des.* 184 (2019) 108202, <https://doi.org/10.1016/J.MATDES.2019.108202>.
- [84] B. Gwalani, V. Soni, O.A. Waseem, S.A. Mantri, R. Banerjee, Laser additive manufacturing of compositionally graded AlCrFeMoVx (x = 0 to 1) high-entropy alloy system, *Opt. Laser Technol.* 113 (2019) 330–337, <https://doi.org/10.1016/J.OPTLASTEC.2019.01.009>.
- [85] M.A. Melia, J.D. Carroll, S.R. Whetten, S.N. Esmaeely, J. Locke, E. White, I. Anderson, M. Chandross, J.R. Michael, N. Argibay, E.J. Schindelholz, A. B. Kustas, Mechanical and Corrosion Properties of Additively Manufactured CoCrFeMnNi High Entropy Alloy, *Addit. Manuf.* 29 (2019) 100833, <https://doi.org/10.1016/J.ADDMA.2019.100833>.
- [86] I. Kunce, M. Polanski, J. Bystrzycki, Structure and hydrogen storage properties of a high entropy ZrTiCrFeNi alloy synthesized using Laser Engineered Net Shaping (LENS), *Int. J. Hydrog. Energy* 38 (2013) 12180–12189, <https://doi.org/10.1016/J.IJHYDENE.2013.05.071>.
- [87] D. Lin, L. Xu, X. Li, H. Jing, G. Qin, H. Pang, F. Minami, A Si-containing FeCoCrNi high-entropy alloy with high strength and ductility synthesized in situ via selective laser melting, *Addit. Manuf.* 35 (2020) 101340, <https://doi.org/10.1016/J.ADDMA.2020.101340>.
- [88] S. Sarkar, P.K. Sarswat, M.L. Free, Elevated temperature corrosion resistance of additive manufactured single phase AlCoFeNiTiV0.9Sm0.1 and AlCoFeNiV0.9Sm0.1 HEAs in a simulated syngas atmosphere, *Addit. Manuf.* 30 (2019) 100902, <https://doi.org/10.1016/J.ADDMA.2019.100902>.
- [89] D. Lin, L. Xu, H. Jing, Y. Han, L. Zhao, F. Minami, Effects of annealing on the structure and mechanical properties of FeCoCrNi high-entropy alloy fabricated via selective laser melting, *Addit. Manuf.* 32 (2020) 101058, <https://doi.org/10.1016/J.ADDMA.2020.101058>.
- [90] Y.K. Kim, S. Yang, K.A. Lee, Compressive creep behavior of selective laser melted CoCrFeMnNi high-entropy alloy strengthened by in-situ formation of nano-oxides, *Addit. Manuf.* 36 (2020) 101543, <https://doi.org/10.1016/J.JADDMA.2020.101543>.
- [91] H.Y. Jung, N.J. Peter, E. Gärtner, G. Dehm, V. Uhlenwinkel, E.A. Jägle, Bulk nanostructured AlCoCrFeMnNi chemically complex alloy synthesized by laser-powder bed fusion, *Addit. Manuf.* 35 (2020) 101337, <https://doi.org/10.1016/J.JADDMA.2020.101337>.
- [92] X. Yang, Y. Zhou, S. Xi, Z. Chen, P. Wei, C. He, T. Li, Y. Gao, H. Wu, Additively manufactured fine grained Ni6Cr4WFe9Ti high entropy alloys with high strength and ductility, *Mater. Sci. Eng. A* 767 (2019) 138394, <https://doi.org/10.1016/J.MSEA.2019.138394>.
- [93] Z. Xu, H. Zhang, W. Li, A. Mao, L. Wang, G. Song, Y. He, Microstructure and nanoindentation creep behavior of CoCrFeMnNi high-entropy alloy fabricated by selective laser melting, *Addit. Manuf.* 28 (2019) 766–771, <https://doi.org/10.1016/J.JADDMA.2019.06.012>.
- [94] W.C. Lin, Y.J. Chang, T.H. Hsu, S. Gorsse, F. Sun, T. Furuhara, A.C. Yeh, Microstructure and tensile property of a precipitation strengthened high entropy

- alloy processed by selective laser melting and post heat treatment, *Addit. Manuf.* 36 (2020) 101601, <https://doi.org/10.1016/J.ADDMA.2020.101601>.
- [95] Y. Su, S. Luo, Z. Wang, Microstructure evolution and cracking behaviors of additively manufactured AlxCrCuFeNi2 high entropy alloys via selective laser melting, *J. Alloy. Compd.* 842 (2020) 155823, <https://doi.org/10.1016/J.JALLOCOM.2020.155823>.
- [96] Y.K. Kim, M.S. Baek, S. Yang, K.A. Lee, In-situ formed oxide enables extraordinary high-cycle fatigue resistance in additively manufactured CoCrFeMnNi high-entropy alloy, *Addit. Manuf.* 38 (2021) 101832, <https://doi.org/10.1016/J.ADDMA.2020.101832>.
- [97] I. Kunce, M. Polanski, J. Bystrzycki, Microstructure and hydrogen storage properties of a TiZrNbMoV high entropy alloy synthesized using Laser Engineered Net Shaping (LENS), *Int. J. Hydrom. Energy* 39 (2014) 9904–9910, <https://doi.org/10.1016/J.IJHYDENE.2014.02.067>.
- [98] H. Chen, T. Lu, Y. Wang, Y. Liu, T. Shi, K.G. Prashanth, K. Kosiba, Laser additive manufacturing of nano-TiC particles reinforced CoCrFeMnNi high-entropy alloy matrix composites with high strength and ductility, *Mater. Sci. Eng. A* 833 (2022) 142512, <https://doi.org/10.1016/J.MSEA.2021.142512>.
- [99] J. Li, S. Xiang, H. Luan, A. Amar, X. Liu, S. Lu, Y. Zeng, G. Le, X. Wang, F. Qu, C. Jiang, G. Yang, Additive manufacturing of high-strength CrMnFeCoNi high-entropy alloys-based composites with WC addition, *J. Mater. Sci. Technol.* 35 (2019) 2430–2434, <https://doi.org/10.1016/J.JMST.2019.05.062>.
- [100] J.W. Pegues, M.A. Melia, R. Puckett, S.R. Whetten, N. Argibay, A.B. Kustas, Exploring additive manufacturing as a high-throughput screening tool for multiphase high entropy alloys, *Addit. Manuf.* 37 (2021) 101598, <https://doi.org/10.1016/J.ADDMA.2020.101598>.
- [101] T. Fujieda, M. Chen, H. Shiratori, K. Kuwabara, K. Yamanaka, Y. Koizumi, A. Chiba, S. Watanabe, Mechanical and corrosion properties of CoCrFeNiTi-based high-entropy alloy additive manufactured using selective laser melting, *Addit. Manuf.* 25 (2019) 412–420, <https://doi.org/10.1016/J.ADDMA.2018.10.023>.
- [102] C.K. Ng, K. Bai, D. Wuu, K.B. Lau, J.J. Lee, A.K.H. Cheong, F. Wei, B. Cheng, P. Wang, D.C.C. Tan, Y.W. Zhang, Additive manufacturing of high-strength and ductile high entropy alloy CoCrFeNiW0.2 composites via laser powder bed fusion and post-annealing, *J. Alloy. Compd.* 906 (2022) 164288, <https://doi.org/10.1016/J.JALLOCOM.2022.164288>.
- [103] Z. Gu, X. Su, W. Peng, W. Guo, S. Xi, X. Zhang, H. Tu, Y. Gao, H. Wu, An important improvement of strength and ductility on a new type of CoCr2.5FeNi2TiW0.5 high entropy alloys under two different protective gases by selective laser melting, *J. Alloy. Compd.* 868 (2021) 159088, <https://doi.org/10.1016/J.JALLOCOM.2021.159088>.
- [104] X. Zhang, R. Li, L. Huang, A. Amar, C. Wu, G. Le, X. Liu, D. Guan, G. Yang, J. Li, Influence of in-situ and ex-situ precipitations on microstructure and mechanical properties of additive manufacturing CoCrFeMnNi high-entropy alloys, *Vacuum* 187 (2021) 110111, <https://doi.org/10.1016/J.VACUUM.2021.110111>.
- [105] K. Zhou, J. Li, L. Wang, H. Yang, Z. Wang, J. Wang, Direct laser deposited bulk CoCrFeNiNb high entropy alloys, *Intermet.* (Barking) 114 (2019) 106592, <https://doi.org/10.1016/J.INTERMET.2019.106592>.
- [106] N. Li, S. Wu, D. Ouyang, J. Zhang, L. Liu, Fe-based metallic glass reinforced FeCoCrNiMn high entropy alloy through selective laser melting, *J. Alloy. Compd.* 822 (2020) 153695, <https://doi.org/10.1016/J.JALLOCOM.2020.153695>.
- [107] C. Kenel, N.P.M. Casati, D.C. Dunand, 3D ink-extrusion additive manufacturing of CoCrFeNi high-entropy alloy micro-lattices, 2019 10:1, *Nat. Commun.* 10 (2019) 1–8, <https://doi.org/10.1038/s41467-019-08763-4>.
- [108] S. Gou, M. Gao, Y. Shi, S. Li, Y. Fang, X. Chen, H. Chen, W. Yin, J. Liu, Z. Lei, H. Wang, Additive manufacturing of ductile refractory high-entropy alloys via phase engineering, *Acta Mater.* 248 (2023) 118781, <https://doi.org/10.1016/J.ACTAMAT.2023.118781>.
- [109] G. Gong, J. Ye, Y. Chi, Z. Zhao, Z. Wang, G. Xia, X. Du, H. Tian, H. Yu, C. Chen, Research status of laser additive manufacturing for metal: a review, *J. Mater. Res. Technol.* 15 (2021) 855–884, <https://doi.org/10.1016/J.JMRT.2021.08.050>.
- [110] S. Garzon-Hernandez, D. Garcia-Gonzalez, A. Jérusalem, A. Arias, Design of FDM 3D printed polymers: an experimental-modelling methodology for the prediction of mechanical properties, *Mater. Des.* 188 (2020) 108414, <https://doi.org/10.1016/J.MATDES.2019.108414>.
- [111] M. Javaid, A. Haleem, R.P. Singh, R. Suman, S. Rab, Role of additive manufacturing applications towards environmental sustainability, *Adv. Ind. Eng. Polym. Res.* 4 (2021) 312–322, <https://doi.org/10.1016/J.AIEPR.2021.07.005>.
- [112] W. Zhang, A. Chabok, B.J. Kooi, Y. Pei, Additive manufactured high entropy alloys: A review of the microstructure and properties, *Mater. Des.* 220 (2022) 110875, <https://doi.org/10.1016/J.MATDES.2022.110875>.
- [113] J. Ge, S. Pillay, H. Ning, Post-Process Treatments for Additive-Manufactured Metallic Structures: A Comprehensive Review, 32:16, *J. Mater. Eng. Perform.* 32 (2023) 7073–7122, <https://doi.org/10.1007/S11665-023-08051-9>.
- [114] M.J. Mirzaali, V. Moosabeiki, S.M. Rajaa, J. Zhou, A.A. Zadpoor, Additive Manufacturing of Biomaterials—Design Principles and Their Implementation, *Materials* 15 (2022), <https://doi.org/10.3390/MA15155457>.
- [115] M. Vignesh, G. Ranjith Kumar, M. Sathishkumar, M. Manikandan, G. Rajyalakshmi, R. Ramanujam, N. Arivazhagan, Development of Biomedical Implants through Additive Manufacturing: A Review, *J. Mater. Eng. Perform.* 30 (2021) 4735–4744, <https://doi.org/10.1007/S11665-021-05578-7/FIGURES/1>.
- [116] T. Ron, A. Shirizly, E. Aghion, Additive manufacturing technologies of high entropy alloys (HEA): review and prospects, 2023, Vol. 16, Page 2454, *Materials* 16 (2023) 2454, <https://doi.org/10.3390/MA16062454>.
- [117] Y. Yu, L. Wang, J. Zhou, H. Li, Y. Li, W. Yan, F. Lin, Impact of fluid flow on the dendrite growth and the formation of new grains in additive manufacturing, *Addit. Manuf.* 55 (2022) 102832, <https://doi.org/10.1016/J.ADDMA.2022.102832>.
- [118] S. Jung, B. Kara, Z. Nie, T.W. Simpson, K.S. Whitefoot, Is additive manufacturing an environmentally and economically preferred alternative for mass production? *Environ. Sci. Technol.* 57 (2023) 6373–6386, <https://doi.org/10.1021/acs.est.2c04927>.
- [119] M. Dada, P. Popoola, N. Mathe, S. Pityana, S. Adeosun, Parametric optimization of laser deposited high entropy alloys using response surface methodology (RSM), *Int. J. Adv. Manuf. Technol.* 109 (2020) 2719–2732, <https://doi.org/10.1007/S00170-020-05781-1/FIGURES/19>.
- [120] K. Sun, W. Peng, L. Yang, L. Fang, Effect of SLM Processing Parameters on Microstructures and Mechanical Properties of Al0.5CoCrFeNi High Entropy Alloys, 2020, Vol. 10, Page 292, *Metals* 10 (2020) 292, <https://doi.org/10.3390/MET10020292>.
- [121] S. Xiang, J. Li, H. Luan, A. Amar, S. Lu, K. Li, L. Zhang, X. Liu, G. Le, X. Wang, F. Qu, W. Zhang, D. Wang, Q. Li, Effects of process parameters on microstructures and tensile properties of laser melting deposited CrMnFeCoNi high entropy alloys, *Mater. Sci. Eng. A* 743 (2019) 412–417, <https://doi.org/10.1016/J.MSEA.2018.11.110>.
- [122] Y. Zhang, T. fei Han, M. Xiao, Y. fu Shen, Effect of process parameters on the microstructure and properties of laser-clad FeNiCoCrTi0.5 high-entropy alloy coating, *IJMIMM* 27 (2020) 630–639, <https://doi.org/10.1007/S12613-019-1958-7/METRICS>.
- [123] A.A. Akinwande, O.A. Balogun, A.A. Adediran, O.S. Adesina, V. Romanovski, T. C. Jen, Experimental analysis, statistical modeling, and parametric optimization of quinary-(CoCrFeMnNi)100-x/TiCx high-entropy-alloy (HEA) manufactured by laser additive manufacturing, *RIE* 17 (2023) 100802, <https://doi.org/10.1016/J.RINENG.2022.100802>.
- [124] M. Dada, P. Popoola, N. Mathe, S. Pityana, S. Adeosun, Effect of laser parameters on the properties of high entropy alloys: A preliminary study, *Mater. Today Proc.* 38 (2021) 756–761, <https://doi.org/10.1016/J.MATPR.2020.04.198>.
- [125] H. Osman, L. Liu, J. Pan, R. Guo, J. Xu, P. Zhang, L. Liu, Effect of TiC addition on the microstructure and mechanical properties of FeCoCrNiMn high entropy alloy fabricated by selective laser melting, *J. Alloy. Compd.* 982 (2024) 173583, <https://doi.org/10.1016/J.JALLOCOM.2024.173583>.
- [126] M. Dada, P. Popoola, N. Mathe, S. Pityana, S. Adeosun, O. Aramide, T. Lengopen, Process optimization of high entropy alloys by laser additive manufacturing, *Eng. Rep.* 2 (2020) e12252, <https://doi.org/10.1002/ENG2.12252>.
- [127] M. Rappaz, J.M. Drezet, M. Gremaud, A new hot-tearing criterion, *Metall. Mater. Trans. A Phys. Metall. Mater. Sci.* 30 (1999) 449–455, <https://doi.org/10.1007/S11661-999-0334-Z/METRICS>.
- [128] B. Yuan, C. Li, Y. Dong, Y. Yang, P. Zhang, Z. Zhang, Selective laser melting of the Al0.3CoCrFeNiCu high-entropy alloy: Processing parameters, microstructure and mechanical properties, *Mater. Des.* 220 (2022) 110847, <https://doi.org/10.1016/J.MATDES.2022.110847>.
- [129] M. Jafary-Zadeh, Z.H. Aitken, R. Tavakoli, Y.W. Zhang, On the controllability of phase formation in rapid solidification of high entropy alloys, *J. Alloy. Compd.* 748 (2018) 679–686, <https://doi.org/10.1016/J.JALLOCOM.2018.03.165>.
- [130] Y. Zhang, T. Han, M. Xiao, Y. Shen, Effect of Nb content on microstructure and properties of laser cladding FeNiCoCrTi0.5Nb high-entropy alloy coating, *Opt. (Stuttg.)* 198 (2019), <https://doi.org/10.1016/J.OPTOLEO.2019.163316>.
- [131] C.J. Tong, Y.L. Chen, S.K. Chen, J.W. Yeh, T.T. Shun, C.H. Tsau, S.J. Lin, S. Y. Chang, Microstructure characterization of AlCoCrCuFeNi high-entropy alloy system with multiprincipal elements, *Metall. Mater. Trans. A Phys. Metall. Mater. Sci.* 36 (2005) 881–893, <https://doi.org/10.1007/S11661-005-0283-0/METRICS>.
- [132] W. Cui, S. Karnati, X. Zhang, E. Burns, F. Liou, Fabrication of AlCoCrFeNi High-Entropy Alloy Coating on an AISI 304 Substrate via a CoFe2Ni Intermediate Layer, 2019, Vol. 21, Page 2, *Entropy* 21 (2018) 2, <https://doi.org/10.3390/E21010002>.
- [133] R. Wang, K. Zhang, C. Davies, X. Wu, Evolution of microstructure, mechanical and corrosion properties of AlCoCrFeNi high-entropy alloy prepared by direct laser fabrication, *J. Alloy. Compd.* 694 (2017) 971–981, <https://doi.org/10.1016/J.JALLOCOM.2016.10.138>.
- [134] Y.F. Ye, Q. Wang, J. Lu, C.T. Liu, Y. Yang, High-entropy alloy: challenges and prospects, *Mater. Today* 19 (2016) 349–362, <https://doi.org/10.1016/J.MATTOD.2015.11.026>.
- [135] M. Löbel, T. Lindner, T. Mehner, T. Lampke, Microstructure and wear resistance of AlCoCrFeNiTi high-entropy alloy coatings produced by HVOF, 2017, Vol. 7, Page 144, *Coatings* 7 (2017) 144, <https://doi.org/10.3390/COATINGS7090144>.
- [136] R. Bardo, R. Dziurka, K. Fryzowicz, G. Cios, M. Marciszko-Wiąckowska, M. Gajewska, C. Hain, P. Bala, Influence of process parameters on the quality of powder bed fusion-fabricated Ni-Co-Fe-Mn-Ti high entropy alloy prints using elemental powders, *J. Alloy. Compd.* 972 (2024) 172862, <https://doi.org/10.1016/J.JALLOCOM.2023.172862>.
- [137] S. Mooraj, G. Kim, X. Fan, S. Samuha, Y. Xie, T. Li, J.S. Tiley, Y. Chen, D. Yu, K. An, P. Hosemann, P.K. Liaw, W. Chen, W. Chen, Additive manufacturing of defect-free TiZrNbTa refractory high-entropy alloy with enhanced elastic isotropy via in-situ alloying of elemental powders, 2024 5:1, *Commun. Mater.* 5 (2024) 1–12, <https://doi.org/10.1038/s43246-024-00452-0>.
- [138] R. Li, P. Niu, T. Yuan, P. Cao, C. Chen, K. Zhou, Selective laser melting of an equiatomic CoCrFeMnNi high-entropy alloy: processability, non-equilibrium microstructure and mechanical property, *J. Alloy. Compd.* 746 (2018) 125–134, <https://doi.org/10.1016/J.JALLOCOM.2018.02.298>.
- [139] Y.K. Kim, S. Yang, K.A. Lee, Superior temperature-dependent mechanical properties and deformation behavior of equiatomic CoCrFeMnNi high-entropy

- alloy additively manufactured by selective laser melting, 2020 10:1, Sci. Rep. 10 (2020) 1–13, <https://doi.org/10.1038/s41598-020-65073-2>.
- [140] R.B. Figueiredo, T.G. Langdon, Deformation mechanisms in ultrafine-grained metals with an emphasis on the Hall-Petch relationship and strain rate sensitivity, J. Mater. Res. Technol. 14 (2021) 137–159, <https://doi.org/10.1016/J.JMRT.2021.06.016>.
- [141] A. Huang, S.J. Fensin, M.A. Meyers, Strain-rate effects and dynamic behavior of high entropy alloys, J. Mater. Res. Technol. 22 (2023) 307–347, <https://doi.org/10.1016/J.JMRT.2022.11.057>.
- [142] X. Wang, W. Bai, Z. Zhang, Z. Wang, X. Ren, Enhanced fatigue resistance of a face-centered-cubic single-phase Al0.3CoCrFeNi high-entropy alloy through planar deformation characteristic, Mater. Sci. Eng. A 862 (2023) 144499, <https://doi.org/10.1016/J.MSEA.2022.144499>.
- [143] K.K. Alaneme, M.O. Bodunrin, S.R. Oke, Processing, alloy composition and phase transition effect on the mechanical and corrosion properties of high entropy alloys: a review, J. Mater. Res. Technol. 5 (2016) 384–393, <https://doi.org/10.1016/J.JMRT.2016.03.004>.
- [144] B. Xiao, W. Jia, J. Wang, L. Zhou, Selective electron beam melting of WMoTaNbVFeCoCrNi refractory high-entropy alloy, Mater. Charact. 193 (2022) 112278, <https://doi.org/10.1016/J.MATCHAR.2022.112278>.
- [145] T. Fujieda, H. Shiratori, K. Kuwabara, M. Hirota, T. Kato, K. Yamanaka, Y. Koizumi, A. Chiba, S. Watanabe, CoCrFeNiTi-based high-entropy alloy with superior tensile strength and corrosion resistance achieved by a combination of additive manufacturing using selective electron beam melting and solution treatment, Mater. Lett. 189 (2017) 148–151, <https://doi.org/10.1016/J.MATLET.2016.11.026>.
- [146] K. Kuwabara, H. Shiratori, T. Fujieda, K. Yamanaka, Y. Koizumi, A. Chiba, Mechanical and corrosion properties of AlCoCrFeNi high-entropy alloy fabricated with selective electron beam melting, Addit. Manuf. 23 (2018) 264–271, <https://doi.org/10.1016/J.ADDMA.2018.06.006>.
- [147] Z. Gu, J. He, Y. Qin, P. Zhang, P. Zhang, D. Zhang, H. Wu, L.L. Xiao, S. Xi, Ultra strong FCC structured Ni8Cr4Co4Fe6W2 high entropy alloys with high strength and ductility by laser powder bed fusion, J. Alloy. Compd. 992 (2024) 174580, <https://doi.org/10.1016/J.JALLOCOM.2024.174580>.
- [148] K. Li, V. Trofimov, C. Han, G. Hu, Z. Dong, Y. Zou, Z. Wang, F. Yan, Z. Fu, Y. Yang, The Printability, Microstructure, and Mechanical Properties of Fe80–xMnxCo10Cr10 High-Entropy Alloys Fabricated by Laser Powder Bed Fusion Additive Manufacturing, 2024, Vol. 15, Page 123, Micromach 15 (2024) 123, <https://doi.org/10.3390/MI15010123>.
- [149] G.M. Karthik, Y. Kim, E.S. Kim, A. Zargaran, P. Sathiyamoorthi, J.M. Park, S. G. Jeong, G.H. Gu, A. Amanov, T. Ungar, H.S. Kim, Gradient heterostructured laser-powder bed fusion processed CoCrFeMnNi high entropy alloy, Addit. Manuf. 59 (2022) 103131, <https://doi.org/10.1016/J.ADDMA.2022.103131>.
- [150] P. Agrawal, S. Thapliyal, S.S. Nene, R.S. Mishra, B.A. McWilliams, K.C. Cho, Excellent strength-ductility synergy in metastable high entropy alloy by laser powder bed additive manufacturing, Addit. Manuf. 32 (2020) 101098, <https://doi.org/10.1016/J.ADDMA.2020.101098>.
- [151] A. Mehta, T. Huynh, N. Kljestan, K. Graydon, A. Mahmud, M. Knezevic, B. McWilliams, K. Cho, Y. Sohn, Additive manufacturing of Al18Co30Cr10Fe10Ni32 high entropy alloy by gas atomization and laser powder bed fusion, Mater. Lett. 350 (2023) 134942, <https://doi.org/10.1016/J.MATLET.2023.134942>.
- [152] H. Zhang, J. Cai, J. Geng, X. Sun, Y. Zhao, X. Guo, D. Li, Study on annealing treatment of NbMoTaTiNi high-entropy alloy with ultra-high strength disordered-ordered transition structure for additive manufacturing, J. Alloy. Compd. 941 (2023) 168810, <https://doi.org/10.1016/J.JALLOCOM.2023.168810>.
- [153] A. Chabok, W. Zhang, J. Shen, J.P. Oliveira, H. Wang, S. Feng, N. Schell, B.J. Kooi, Y. Pei, On the orientation-dependent mechanical properties of interstitial solute-strengthened Fe49.5Mn30Co10Cr10C0.5 high entropy alloy produced by directed energy deposition, Addit. Manuf. 79 (2024) 103914, <https://doi.org/10.1016/J.ADDMA.2023.103914>.
- [154] X. Nie, Y. Lv, Effect of heat treatment on microstructure of Al0.78CoCrFeNi alloy fabricated by laser additive manufacturing, JOM 76 (2024) 843–852, <https://doi.org/10.1007/S11837-023-06243-1/FIGURES/8>.
- [155] M. Zhang, J. Li, Y. Li, J. Wang, Z. Li, X. Cheng, Effect of Al addition on the microstructure and hardness of the (Al<sub>x</sub>CoCrFe)50Ni high-entropy alloy prepared by directed energy deposition technique, Mater. Lett. 285 (2021) 128778, <https://doi.org/10.1016/J.MATLET.2020.128778>.
- [156] M. Zheng, C. Li, X. Zhang, Z. Ye, X. Yang, J. Gu, The influence of columnar to equiaxed transition on deformation behavior of FeCoCrNiMn high entropy alloy fabricated by laser-based directed energy deposition, Addit. Manuf. 37 (2021) 101660, <https://doi.org/10.1016/J.ADDMA.2020.101660>.
- [157] G. Shao, J. Lei, F. Zhang, S. Wang, H. Hu, K. Wang, P. Tan, J. Yi, A Study of the Microstructure and Mechanical and Electrochemical Properties of CoCrFeNi High-Entropy Alloys Additive-Manufactured Using Laser Metal Deposition, 2023, Vol. 13, Page 1583, Coatings 13 (2023) 1583, <https://doi.org/10.3390/COATINGS13091583>.
- [158] Y. Chew, G.J. Bi, Z.G. Zhu, F.L. Ng, F. Weng, S.B. Liu, S.M.L. Nai, B.Y. Lee, Microstructure and enhanced strength of laser aided additive manufactured CoCrFeNiMn high entropy alloy, Mater. Sci. Eng. A 744 (2019) 137–144, <https://doi.org/10.1016/J.MSEA.2018.12.005>.
- [159] J. Joseph, N. Stanford, P. Hodgson, D.M. Fabijanic, Understanding the mechanical behaviour and the large strength/ductility differences between FCC and BCC AlxCrCoCrFeNi high entropy alloys, J. Alloy. Compd. 726 (2017) 885–895, <https://doi.org/10.1016/J.JALLOCOM.2017.08.067>.
- [160] H. Dobbelstein, E.L. Gurevich, E.P. George, A. Ostendorf, G. Laplanche, Laser metal deposition of a refractory TiZrNbHfTa high-entropy alloy, Addit. Manuf. 24 (2018) 386–390, <https://doi.org/10.1016/J.ADDMA.2018.10.008>.
- [161] G.H. Gu, E.S. Kim, H. Kwon, S. Son, R.E. Kim, T.G. Oh, H.S. Kim, Fabrication of multi-gradient heterostructured CoCrFeMnNi high-entropy alloy using laser metal deposition, Mater. Sci. Eng. A 836 (2022) 142718, <https://doi.org/10.1016/J.MSEA.2022.142718>.
- [162] B.T. Mengiste, A. Arab, Y. Guo, Y. Lei, X. Li, P. Chen, J. Xie, Tuning the mechanical properties of CrCoFeMnNi high entropy alloy via cold spray additive manufacturing associated with heat treatment, Mater. Sci. Eng. A 894 (2024) 146214, <https://doi.org/10.1016/J.MSEA.2024.146214>.
- [163] Y. Brif, M. Thomas, I. Todd, The use of high-entropy alloys in additive manufacturing, Scr. Mater. 99 (2015) 93–96, <https://doi.org/10.1016/J.SCRIPTAMAT.2014.11.037>.
- [164] R. Zhou, Y. Liu, C. Zhou, S. Li, W. Wu, M. Song, B. Liu, X. Liang, P.K. Liaw, Microstructures and mechanical properties of C-containing FeCoCrNi high-entropy alloy fabricated by selective laser melting, Intermet. (Barking) 94 (2018) 165–171, <https://doi.org/10.1016/J.INTERMET.2018.01.002>.
- [165] C. Haase, F. Tang, M.B. Wilms, A. Weisheit, B. Hallstedt, Combining thermodynamic modeling and 3D printing of elemental powder blends for high-throughput investigation of high-entropy alloys – Towards rapid alloy screening and design, Mater. Sci. Eng. A 688 (2017) 180–189, <https://doi.org/10.1016/J.MSEA.2017.01.099>.
- [166] Q. Sui, Z. Wang, J. Wang, S. Xu, F. Zhao, L. Gong, B. Liu, J. Liu, G. Liu, The microstructure and mechanical properties of the additive manufactured AlCoCrFeNi high entropy alloy, Mater. Sci. Eng. A 833 (2022) 142507, <https://doi.org/10.1016/J.MSEA.2021.142507>.
- [167] I. Kunce, M. Polanski, K. Karczewski, T. Plocinski, K.J. Kurzydlowski, Microstructural characterisation of high-entropy alloy AlCoCrFeNi fabricated by laser engineered net shaping, J. Alloy. Compd. 648 (2015) 751–758, <https://doi.org/10.1016/J.JALLOCOM.2015.05.144>.
- [168] H. Shiratori, T. Fujieda, K. Yamanaka, Y. Koizumi, K. Kuwabara, T. Kato, A. Chiba, Relationship between the microstructure and mechanical properties of an equiautomatic AlCoCrFeNi high-entropy alloy fabricated by selective electron beam melting, Mater. Sci. Eng. A 656 (2016) 39–46, <https://doi.org/10.1016/J.MSEA.2016.01.019>.
- [169] J. Joseph, T. Jarvis, X. Wu, N. Stanford, P. Hodgson, D.M. Fabijanic, Comparative study of the microstructures and mechanical properties of direct laser fabricated and arc-melted AlxCrCoCrFeNi high entropy alloys, Mater. Sci. Eng. A 633 (2015) 184–193, <https://doi.org/10.1016/J.MSEA.2015.02.072>.
- [170] T. Fujieda, H. Shiratori, K. Kuwabara, T. Kato, K. Yamanaka, Y. Koizumi, A. Chiba, First demonstration of promising selective electron beam melting method for utilizing high-entropy alloys as engineering materials, Mater. Lett. 159 (2015) 12–15, <https://doi.org/10.1016/J.MATLET.2015.06.046>.
- [171] S. Xiang, H. Luan, J. Wu, K.F. Yao, J. Li, X. Liu, Y. Tian, W. Mao, H. Bai, G. Le, Q. Li, Microstructures and mechanical properties of CrMnFeCoNi high entropy alloys fabricated using laser metal deposition technique, J. Alloy. Compd. 773 (2019) 387–392, <https://doi.org/10.1016/J.JALLOCOM.2018.09.235>.
- [172] M. Dada, P. Popoola, N. Mathe, S. Adeosun, Wear characteristics of laser-deposited AlCoCrCuFeNi high entropy alloy with finite element analysis, Beni. Suef. Univ. J. Basic Appl. Sci. 11 (2022) 1–12, <https://doi.org/10.1186/S43088-022-00307-Y/TABLES/6>.
- [173] K. Yamanaka, H. Shiratori, M. Mori, K. Omura, T. Fujieda, K. Kuwabara, A. Chiba, Corrosion mechanism of an equimolar AlCoCrFeNi high-entropy alloy additively manufactured by electron beam melting, NPJ, 2020 4:1, Mater. Degr. 4 (2020) 1–12, <https://doi.org/10.1038/s41529-020-00127-4>.
- [174] S. Yang, Z. Liu, J. Pi, Microstructure and wear behavior of the AlCrFeCoNi high-entropy alloy fabricated by additive manufacturing, Mater. Lett. 261 (2020) 127004, <https://doi.org/10.1016/J.MATLET.2019.127004>.
- [175] Q. Wang, A. Amar, C. Jiang, H. Luan, S. Zhao, H. Zhang, G. Le, X. Liu, X. Wang, X. Yang, J. Li, CoCrFeNiMo0.2 high entropy alloy by laser melting deposition: Prospective material for low temperature and corrosion resistant applications, Intermet. (Barking) 119 (2020) 106727, <https://doi.org/10.1016/J.INTERMET.2020.106727>.
- [176] B.A. Welk, R.E.A. Williams, G.B. Viswanathan, M.A. Gibson, P.K. Liaw, H. L. Fraser, Nature of the interfaces between the constituent phases in the high entropy alloy CoCrCuFeNiAl, Ultramicros 134 (2013) 193–199, <https://doi.org/10.1016/J.ULTRAMIC.2013.06.006>.
- [177] M. Dada, P. Popoola, N. Mathe, S. Pityana, S. Adeosun, O. Aramide, The comparative study of the microstructural and corrosion behaviour of laser-deposited high entropy alloys, J. Alloy. Compd. 866 (2021) 158777, <https://doi.org/10.1016/J.JALLOCOM.2021.158777>.
- [178] Z.G. Zhu, Q.B. Nguyen, F.L. Ng, X.H. An, X.Z. Liao, P.K. Liaw, S.M.L. Nai, J. Wei, Hierarchical microstructure and strengthening mechanisms of a CoCrFeNiMn high entropy alloy additively manufactured by selective laser melting, Scr. Mater. 154 (2018) 20–24, <https://doi.org/10.1016/J.SCRIPTAMAT.2018.05.015>.
- [179] M. Zhang, X. Zhou, D. Wang, W. Zhu, J. Li, Y.F. Zhao, AlCoCuFeNi high-entropy alloy with tailored microstructure and outstanding compressive properties fabricated via selective laser melting with heat treatment, Mater. Sci. Eng. A 743 (2019) 773–784, <https://doi.org/10.1016/J.MSEA.2018.11.118>.
- [180] P. Chen, C. Yang, S. Li, M.M. Attallah, M. Yan, In-situ alloyed, oxide-dispersion-strengthened CoCrFeMnNi high entropy alloy fabricated via laser powder bed fusion, Mater. Des. 194 (2020) 108966, <https://doi.org/10.1016/J.MATERIALS.2020.108966>.
- [181] J.M. Park, J. Choe, J.G. Kim, J.W. Bae, J. Moon, S. Yang, K.T. Kim, J.H. Yu, H. S. Kim, Superior tensile properties of 1%CoCrFeMnNi high-entropy alloy

- additively manufactured by selective laser melting, *Mater. Res. Lett.* 8 (2020) 1–7, <https://doi.org/10.1080/21663831.2019.1638844>.
- [182] M. Jin, A. Piglione, B. Dovgyy, E. Hosseini, P.A. Hooper, S.R. Holdsworth, M. S. Pham, Cyclic plasticity and fatigue damage of CrMnFeCoNi high entropy alloy fabricated by laser powder-bed fusion, *Addit. Manuf.* 36 (2020) 101584, <https://doi.org/10.1016/J.ADDMA.2020.101584>.
- [183] Z.G. Zhu, X.H. An, W.J. Lu, Z.M. Li, F.L. Ng, X.Z. Liao, U. Ramamurti, S.M.L. Nai, J. Wei, Selective laser melting enabling the hierarchically heterogeneous microstructure and excellent mechanical properties in an interstitial solute strengthened high entropy alloy, *Mater. Res. Lett.* 7 (2019) 453–459, <https://doi.org/10.1080/21663831.2019.1650131>.
- [184] X. Gao, Y. Lu, Laser 3D printing of CoCrFeMnNi high-entropy alloy, *Mater. Lett.* 236 (2019) 77–80, <https://doi.org/10.1016/J.MATLET.2018.10.084>.
- [185] S. Thapliyal, S.S. Nene, P. Agrawal, T. Wang, C. Morphew, R.S. Mishra, B. A. McWilliams, K.C. Cho, Damage-tolerant, corrosion-resistant high entropy alloy with high strength and ductility by laser powder bed fusion additive manufacturing, *Addit. Manuf.* 36 (2020) 101455, <https://doi.org/10.1016/J.ADDMA.2020.101455>.
- [186] S. Guan, D. Wan, K. Solberg, F. Berto, T. Welo, T.M. Yue, K.C. Chan, Additive manufacturing of fine-grained and dislocation-populated CrMnFeCoNi high entropy alloy by laser engineered net shaping, *Mater. Sci. Eng. A* 761 (2019) 138056, <https://doi.org/10.1016/J.MSEA.2019.138056>.
- [187] P. Kumar, N.K. Jain, S. Jaiswal, S. Gupta, Development of Ti-Ta–Nb–Mo–Zr high entropy alloy by  $\mu$ -plasma arc additive manufacturing process for knee implant applications and its biocompatibility evaluation, *J. Mater. Res. Technol.* 22 (2023) 541–555, <https://doi.org/10.1016/J.JMRT.2022.11.167>.
- [188] T. Ishimoto, R. Ozasa, K. Nakano, M. Weinmann, C. Schnitter, M. Stenzel, A. Matsugaki, T. Nagase, T. Matsuzaka, M. Todai, H.S. Kim, T. Nakano, Development of TiNbTaZrMo bio-high entropy alloy (BioHEA) super-solid solution by selective laser melting, and its improved mechanical property and biocompatibility, *Scri. Mater.* 194 (2021) 113658, <https://doi.org/10.1016/J.SCRIPTAMAT.2020.113658>.
- [189] C. Shuai, J. Xie, X. Jiang, S. Peng, C. Wang, Additively manufactured high entropy alloy with high wear resistance for biomedical implant, *Vacuum* 221 (2024) 112939, <https://doi.org/10.1016/J.VACUUM.2023.112939>.
- [190] J. Feng, D. Wei, P. Zhang, Z. Yu, C. Liu, W. Lu, K. Wang, H. Yan, L. Zhang, L. Wang, Preparation of TiNbTaZrMo high-entropy alloy with tunable Young's modulus by selective laser melting, *J. Manuf. Process.* 85 (2023) 160–165, <https://doi.org/10.1016/J.JMAPRO.2022.11.046>.
- [191] S. Khaleghi, F.N. Dehnavi, M. Baghani, M. Safdari, K. Wang, M. Baniassadi, On the directional elastic modulus of the TPMS structures and a novel hybridization method to control anisotropy, *Mater. Des.* 210 (2021) 110074, <https://doi.org/10.1016/J.MATDES.2021.110074>.
- [192] M.S. Dargusch, G. Wang, D. Kent, M. Bermingham, J. Venezuela, J.E. Frith, Z. Yu, S. Yu, Z. Shi, Comparison of the Microstructure and Biocorrosion Properties of Additively Manufactured and Conventionally Fabricated near  $\beta$  Ti-25Nb-3Zr-3Mo-2Sn Alloy, *ACS Biomater. Sci. Eng.* 5 (2019) 5844–5856, [https://doi.org/10.1021/ACSBIMATERIALS.9B00596/ASSET/IMAGES/LARGE/AB9B00596\\_0008.JPG](https://doi.org/10.1021/ACSBIMATERIALS.9B00596/ASSET/IMAGES/LARGE/AB9B00596_0008.JPG).
- [193] J. Gao, Y. Jin, Y. Fan, D. Xu, L. Meng, C. Wang, Y. Yu, D. Zhang, F. Wang, Fabricating antibacterial CoCrCuFeNi high-entropy alloy via selective laser melting and in-situ alloying, *J. Mater. Sci. Technol.* 102 (2022) 159–165, <https://doi.org/10.1016/J.JMST.2021.07.002>.
- [194] Z.U. Arif, M.Y. Khalid, E. ur Rehman, Laser-aided additive manufacturing of high entropy alloys: processes, properties, and emerging applications, *J. Manuf. Process.* 78 (2022) 131–171, <https://doi.org/10.1016/J.JMAPRO.2022.04.014>.
- [195] I. Kunce, M. Polański, T. Czujko, Microstructures and hydrogen storage properties of LaNiFeVMn alloys, *Int. J. Hydrot. Energy* 42 (2017) 27154–27164, <https://doi.org/10.1016/J.IJHYDENE.2017.09.039>.
- [196] I. Hussain, C. Lamiel, M. Ahmad, Y. Chen, S. Shuang, M.S. Javed, Y. Yang, K. Zhang, High entropy alloys as electrode material for supercapacitors: A review, *J. Energy Storage* 44 (2021) 103405, <https://doi.org/10.1016/J.EST.2021.103405>.
- [197] Q. Wang, L. Velasco, B. Breitung, V. Presser, High-Entropy Energy Materials in the Age of Big Data: A Critical Guide to Next-Generation Synthesis and Applications, *Adv. Energy Mater.* 11 (2021) 2102355, <https://doi.org/10.1002/AENM.202102355>.
- [198] M. Dada, P. Popoola, O. Aramide, N. Mathe, S. Pityana, Optimization of the corrosion property of a high entropy alloy using response surface methodology, *Mater. Today Proc.* 38 (2021) 1024–1030, <https://doi.org/10.1016/J.MATPR.2020.05.618>.
- [199] M. Avila-Rubio, C. Carreño-Gallardo, J.M. Herrera-Ramirez, B.A. García-Grajeda, F.A. Pérez-González, J.H. Ramirez-Ramirez, N.F. Garza-Montes-de-Oca, F.J. Baldenbro-Lopez, Microstructure and microhardness of high entropy alloys with Zn addition: AlCoFeNiZn and AlCoFeNiMoTiZn, *Adv. Powder Technol.* 32 (2021) 4687–4696, <https://doi.org/10.1016/J.APT.2021.10.012>.
- [200] J. Li, W. Craeghs, C. Jing, S. Gong, F. Shan, Microstructure and physical performance of laser-induction nanocrystals modified high-entropy alloy composites on titanium alloy, *Mater. Des.* 117 (2017) 363–370, <https://doi.org/10.1016/J.MATDES.2016.12.007>.
- [201] N. Tepilo, X. Huang, P.C. Patnaik, Laser-based additive manufacturing technologies for aerospace applications, *Adv. Eng. Mater.* 21 (2019) 1900617, <https://doi.org/10.1002/ADEM.201900617>.
- [202] J. Karimi, P. Ma, Y.D. Jia, K.G. Prashanth, Linear patterning of high entropy alloy by additive manufacturing, *Manuf. Lett.* 24 (2020) 9–13, <https://doi.org/10.1016/J.MFGLET.2020.03.003>.
- [203] C.Y. He, X.H. Gao, M. Dong, X.L. Qiu, J.H. An, H.X. Guo, G. Liu, Further investigation of a novel high entropy alloy MoNbHfZrTi based solar absorber coating with double antireflective layers, *Sol. Energy Mater. Sol. Cells* 217 (2020) 110709, <https://doi.org/10.1016/J.SOLMAT.2020.110709>.
- [204] Y. Zhong, L.E. Rännar, S. Wikman, A. Koptyug, L. Liu, D. Cui, Z. Shen, Additive manufacturing of ITER first wall panel parts by two approaches: Selective laser melting and electron beam melting, *Fus. Eng. Des.* 116 (2017) 24–33, <https://doi.org/10.1016/J.FUSENGDES.2017.01.032>.
- [205] Y. Lu, H. Huang, X. Gao, C. Ren, J. Gao, H. Zhang, S. Zheng, Q. Jin, Y. Zhao, C. Lu, T. Wang, T. Li, A promising new class of irradiation tolerant materials: Ti<sub>22</sub>Rh<sub>16</sub>0.5Mo<sub>0.2</sub> high-entropy alloy, *J. Mater. Sci. Technol.* 35 (2019) 369–373, <https://doi.org/10.1016/J.JMST.2018.09.034>.
- [206] C. Xiang, E.H. Han, Z.M. Zhang, H.M. Fu, J.Q. Wang, H.F. Zhang, G.D. Hu, Design of single-phase high-entropy alloys composed of low thermal neutron absorption cross-section elements for nuclear power plant application, *Intermet. (Barking)* 104 (2019) 143–153, <https://doi.org/10.1016/J.INTERMET.2018.11.001>.
- [207] J. Lu, L. Li, H. Zhang, Y. Chen, L. Luo, X. Zhao, F. Guo, P. Xiao, Oxidation behavior of gas-atomized AlCoCrFeNi high-entropy alloy powder at 900 – 1100 °C, *Corros. Sci.* 181 (2021) 109257, <https://doi.org/10.1016/J.CORSCI.2021.109257>.
- [208] H. Wang, Q. Liu, Y. Guo, H. Lan, MoFe1.5CrTiWAlNb refractory high-entropy alloy coating fabricated by laser cladding, *Intermet. (Barking)* 115 (2019) 106613, <https://doi.org/10.1016/J.INTERMET.2019.106613>.
- [209] X. Qiu, Microstructure and corrosion properties of Al2CrFeCoxCuNiTi high entropy alloys prepared by additive manufacturing, *J. Alloy. Compd.* 887 (2021) 161422, <https://doi.org/10.1016/J.JALLCOM.2021.161422>.
- [210] G.M. Tomboc, T. Kwon, J. Joo, K. Lee, High entropy alloy electrocatalysts: a critical assessment of fabrication and performance, *J. Mater. Chem. A Mater.* 8 (2020) 14844–14862, <https://doi.org/10.1039/D0TA05176D>.
- [211] C. Han, Q. Fang, Y. Shi, S.Beng Tor, C.Kai Chua, K. Zhou, C. Han, S.B. Tor, K. Zhou, Q. Fang, Y. Shi, C.K. Chua, Recent Advances on High-Entropy Alloys for 3D Printing, *Adv. Mater.* 32 (2020) 1903855, <https://doi.org/10.1002/ADMA.201903855>.
- [212] Z. Geng, C. Chen, R. Li, J. Luo, K. Zhou, Composition inhomogeneity reduces cracking susceptibility in additively manufactured AlCoCrFeNi<sub>2.1</sub> eutectic high-entropy alloy produced by laser powder bed fusion, *Addit. Manuf.* 56 (2022) 102941, <https://doi.org/10.1016/J.ADDMA.2022.102941>.